

Alma Mater Studiorum – Università di Bologna

DOTTORATO DI RICERCA IN

GEOFISICA

Ciclo XXXII

Settore Concorsuale:

04/A4 - GEOFISICA

Settore Scientifico Disciplinare:

GEO/10 - GEOFISICA DELLA TERRA SOLIDA

Landslide onset and dynamics investigated numerically through Particle Finite Element Modelling

Presentata da: Liang Wang

Coordinatore Dottorato

Prof. Nadia Pinardi

Supervisore

Prof. Stefano Tinti

Esame finale anno 2020

I would like to dedicate this thesis to my loving parents ...

Acknowledgements

I would like to express my sincere gratitude to my supervisor Prof. Stefano Tinti for the constant support. He gave me the chance to study Geophysics and this starts my PhD at the University of Bologna (UNIBO). I thank Prof. Tinti also for giving me the freedom to explore all possibilities in my research. I would also like to thank Dr. Filippo Zaniboni for his support and encouragement during my PhD. I am grateful to Dr. Xue Zhang for his guidance and suggestions, which have determined the presented work.

I would like to thank Prof. Eugenio Oñate, Dr. Alessandro Franci, Dr. Ignasi de-Pouplana, and Dr. Fei Song for their continuous support during my visit at the Polytechnic University of Catalonia. I am also grateful to Prof. Peter Moczo, Prof. Jozef Kristek, Dr. Martin Galis, and Dr. David Gregor for hosting me a visiting period at the Comenius University in Bratislava.

I thank all the people of the Department of Physics and Astronomy who helped me: Prof. Alberto Armigliato, Dr. Gianluca Pagnoni, Dr. Maria Ausilia Paparo, Dr. Sara Bruni, Mrs. Maria Paola Buccella, Mr. Massimo Bacchetti, Mrs. Caterina Pultrone and other members for their understanding and help that provide me with a warm and friendly environment. I would also like to express my sincere thanks to my friends in the Department, Emanuele, Antonio, Glauco, Francesco, Enrico, Camilla, “due Giulias”, Giovanni, Kanwal for memorable friendship and numerous encouragements.

I would like to thank all the people that in some ways contributed to the accomplishment of this thesis. Finally, I am eternally grateful to my family for their endless support.

Abstract

Thanks to the development of modern advanced numerical techniques, the modelling of the whole landslide process via a single simulation has become possible today. Even though the capability of these comprehensive numerical techniques in large deformation analysis has been proven with many applications, yet few efforts have been devoted to developing landslide simulation tools addressing both the pre-failure and post-failure analyses. The present thesis focuses on the use of Particle Finite Element Modelling (PFEM) in landslide applications. PFEM was originally proposed for problems of fluid mechanics and has been gradually applied to solid mechanics. The PFEM developed here is based on the optimization solver. To assess its capability, also an additional model has been developed in this thesis work: it is the widely adopted model based on depth-averaged equations (DAEs) solved by a finite difference technique. The DAEs has been validated against analytical and laboratory data as well as against the observations of the 1783 Scilla, Italy, landslide event. The PFEM model has been validated through applications to the slope stability analysis problem and to the run-out analysis of the 2008 Tangjiashan, China, landslide. Further, the PFEM model has been used to capture the slip surface and the deposit profile of the 2013 Cà Mengoni landslide, occurred in northern Apennines, Italy. It is found that the weakening process plays a crucial role in the evolution of landslides. Finally, the onset mechanism and landslide dynamics of soil slopes subjected to seismic loading has been studied via the present approach.

Table of contents

List of figures	xiii
List of tables	xvii
1 Introduction	1
1.1 Landslides	1
1.2 Numerical techniques	3
1.3 Motivation and objectives of this work	4
2 Depth-averaged models	7
2.1 Governing equations	7
2.1.1 Balance equations	8
2.1.2 Scaling analysis	10
2.1.3 Depth-averaged equations	10
2.2 Numerical scheme	12
2.2.1 Cell average	12
2.2.2 Flux limiter	15
2.2.3 Stability condition	15
2.2.4 Extension to two-dimensional cases	16
2.3 Benchmarks	17
2.3.1 Classical 'dam-break' problem	17
2.3.2 Two-dimensional 'dam-break' problem	18
2.3.3 Dam break over a triangle hump	19
2.4 Investigation of the 1783 Scilla landslide	21
2.4.1 Mixture model with topography modifications	22
2.4.2 Buoyancy and drag force terms	24
2.4.3 Dynamic evolution of the Scilla landslide	24
2.4.4 Propagation and Deposition	26

3	Particle finite element model	31
3.1	Governing equations	32
3.1.1	Static analysis	32
3.1.2	Dynamic analysis	34
3.1.3	Contact analysis	35
3.2	Min-max program for finite-element analysis	35
3.3	Finite-element discretization	37
3.3.1	Mixed triangular element	37
3.3.2	Finite element discretization	39
3.4	Numerical implementation	41
3.4.1	Implementation of boundary conditions	42
3.4.2	Reformulation to a SOCP problem	43
3.4.3	Solution using MOSEK	45
3.5	Particle finite-element technique	46
4	Applications of landslide modelling	49
4.1	Stability analysis	49
4.1.1	FEM analysis	50
4.1.2	Post-failure analysis by PFEM	54
4.2	Landslide propagation	55
4.2.1	Laboratory test	55
4.2.2	Tangjiashan Landslide	56
5	Entire simulation of landslides	61
5.1	Critical condition	62
5.2	Case study: The 2013 Cà Mengoni landslide	65
5.2.1	Background and slope model	65
5.2.2	Numerical investigation	66
5.3	Conclusions	73
6	Large deformation analysis of soil slopes subjected to seismic loading	75
6.1	Literature reviews	76
6.2	The aim of this work	78
6.3	Clay model configuration	79
6.3.1	Onset and failure Mechanism	82
6.3.2	Influence of weakening parameter	89
6.3.3	Vertical loading	90

Table of contents xi

6.4 Frictional effects 94

7 Conclusions and Outlook 97

Appendix A Short guide of the developed codes 101

References 103

List of figures

2.1	Stencil for 1D cases.	14
2.2	Stencil for 2D cases.	16
2.3	Comparisons between numerical simulation and analytical solution of 1D 'dam-break' problems.	18
2.4	Contour plot of the break at $t = 7.2$ s. Resolution for the simulation is set to 2.5m for both x and y directions.	19
2.5	Height profile of the water break $t = 7.2$ s.	19
2.6	Sketch of the set-up of the dam break experiment over a triangular hump.	20
2.7	Time histories of the water elevation at the seven gauges.	20
2.8	A Geographical location of Scilla (red rectangle). B Area of the Scilla landslide.	22
2.9	Time evolution of the mean velocity of the landslide. The dynamics obtained from the linear drag model is quite similar to the motion depicted by the 1D quadratic-drag block model (Zaniboni et al., 2016), with slightly different accelerations. The landslide accelerates, reaching a peak value at 32 m/s and then starts slowing down. Instead, the curve from the quadratic law provides a much longer duration of the landslide motion. The landslide is strongly decelerated by the water when it crashes into the sea with high velocity and then moves slowly to the final still position. The peak velocity of the present simulations is smaller than the value exceeding 40 m/s obtained by Mazzanti and Bozzano (2011), but the deposit region is successfully reproduced by the model.	26
2.10	Snapshots of the landslide mass taken at 10 s intervals (from $t=10$ s to $t=90$ s) obtained through the linear drag model.	28
2.11	Snapshots of the landslide mass (from $t = 10$ s to $t = 300$ s) obtained through the quadratic drag model.	30
3.1	Schematic of contact condition.	35
3.2	Quadratic/linear isotropic triangular element utilized in the simulation.	38

3.3	Steps for PFEM techniques in the time interval $[t_n, t_{n+1}]$	47
4.1	Initial geometry of the slope model. Lateral displacement is set to zero along left and right boundaries and the bottom is fully fixed.	51
4.2	Searching strategy for FOS.	53
4.3	Final deposits obtained from the PFEM simulation for the reduction factor (a) $RF = 2.24$, (b) $RF = 2.3$, (c) $RF = 2.4$ and (d) $RF = 2.9$. Contours refer to the displacement of soils (unit: meter), and the slip surfaces from the analysis by SRM1, SRM2 and LEM are extracted from Cheng et al. (2007).	54
4.4	Numerical results at five moments: $t = 0.075$ s, $t = 0.125$ s, $t = 0.175$ s, $t = 0.225$ s and the final deposit profile.	56
4.5	Background of Tangjiashan landslide: Left Engineering geology map (modified from Hu et al. (2009) and Xu et al. (2009)); Right Satellite image (modified after Peng and Zhang (2012)).	57
4.6	Simulated propagation with velocity contour at four moments.	58
4.7	(a) deposit profile; (b) Mass variation; (c) Mean velocity profile	59
5.1	Final profiles of the slope with distribution of displacement.	63
5.2	Relationship between the ratio D/D_c and the reduction factors for cohesion and internal friction angle. The reduction factors are not further reduced beyond the limit shown in the graph, since the failure mass reaches the right lateral boundary of the numerical slope domain.	64
5.3	Evolution of the average velocity \bar{v} of the sliding body, computed by averaging over the nodes that have the magnitude of velocity larger than 10^{-4} m/s.	64
5.4	Evolution and numerical set-up of of the main cross-section of the Cà Menconi landslide (after Berti et al. (2017)).	66
5.5	Contour of $PEEQ$ under the critical condition for the slope models.	68
5.6	Normalized $PEEQ$ contour with final profile of landslide for four cases.	69
5.7	Snapshots of $PEEQ$ with $RFC = 1.5$, $RFF = 2$	69
5.8	Relationship between the maximum displacement and the reduction factors RFC and RFF . The simulations are conducted with RFC and RFF varying from 1 to 2 with equal step of 0.1.	70
5.9	Relationship between the MI and the reduction factors RFC and RFF that are varied from 1 to 2 with equal interval of 0.1.	71
5.10	Final deposit profile with four cases. Red and black dashed lines represent actual slope and observed slip surface.	71

5.11	Final deposit profile for the weakening process.	72
6.1	Model of clay slope	80
6.2	Input signals	81
6.3	Material-softening law	81
6.4	Input seismic signal with 7s lasting excitation.	82
6.5	Horizontal displacement of the landslide at four instants: 2 s, 4 s, 6 s, 8 s. (Unit: m)	83
6.6	Horizontal displacement of the landslide at four instants: 10 s, 12 s, 14 s, 16 s. (Unit: m)	84
6.7	Vertical displacement of the landslide at four instants: 2 s, 4 s, 6 s, 8 s. (Unit: m)	85
6.8	Vertical displacement of the landslide at four instants: 10 s, 12 s, 14 s, 16 s. (Unit: m)	85
6.9	Velocity magnitude of the landslide at four instants: 2 s, 4 s, 6 s, 8 s. (Unit: m/s)	86
6.10	Velocity magnitude of the landslide at four instants: 10 s, 12 s, 14 s, 16 s. (Unit: m/s)	87
6.11	Equivalent plastic strain at $t = 6s$	87
6.12	Equivalent plastic strain at $t = 8s$	88
6.13	Equivalent plastic strain at $t = 10s$	88
6.14	Equivalent plastic strain at $t = 12s$	88
6.15	Velocity profiles of Slope-I at five moments from $t = 2s$ to $t = 10s$ with interval of 2 s, Unit: m/s	89
6.16	Velocity profiles of Slope-II at five moments from $t = 2s$ to $t = 10s$ with interval of 2 s, Unit: m/s	90
6.17	Velocity profiles of Slope-II at $t = 4s$ excited by (a) horizontal and (b) two-direction loading, unit: m/s	91
6.18	Velocity profiles of Slope-II at $t = 5s$ excited by (a) horizontal and (b) two-direction loading, unit: m/s	91
6.19	Equivalent plastic strain evolution of Slope-II excited by two-direction load- ing from $t = 4s$ to $t = 6.5s$ with interval of $\Delta t = 0.5s$	92
6.20	Equivalent plastic strain evolution of Slope-II excited by two-direction load- ing at different instants. Slip surfaces are highlighted by adopting a fixed colorbar.	93
6.21	Comparison between velocity profile of Slope-II after the onset of landslide.	93

6.22	Velocity profiles of the landslide under different excitation amplitude at chosen instants.	94
6.23	Velocity evolution of the landslide with higher amplitude.	95

List of tables

4.1	Factor of safety determined by the limit equilibrium method (LEM), the strength reduction method with a non-associated flow rule (SRM1) and an associated flow rule (SRM2), SOCP1 and SOCP2. Diff1 is the percentage difference between the FOSs obtained from SRM1 and SOCP1 in absolute value, while Diff2 is the same but applied to SRM2 and SOCP2. The data of LEM, SRM1 and SRM2 are from Cheng et al. (2007)	53
5.1	Material parameters for homogeneous soil slope.	62

Chapter 1

Introduction

1.1 Landslides

As a widespread found geophysical phenomenon, the term landslide usually refers to various mass movements on slopes, and according to the features of movement type and material components, Varnes built a classification system (Varnes, 1978) with 29 typical landslide types that has been widely accepted and further developed (Hungri et al., 2014), based on several typical movements: fall, topple, slide, spread, and flow. Practically, the whole process of a landslide usually includes the failure, post-failure and propagation stages with distinct kinematic characteristics (Cascini et al., 2009). Different effects such as external loads and rheological relationships act together during the landslide process and pose a challenging problem for researchers.

The initiation of a landslide is governed by the basic physics including the interactions among material strength, gravitational stress, external forces, and pore-fluid pressure (Keefer and Larsen, 2007). Intensive rainfalls and seismic shaking are known to be two main factors triggering the failure of landslides according to abundant observational evidence. The large uncertainties on triggering factors and material properties lead to the huge complexity of the identification of unstable zones.

The motion and deposition of landslides are usually studied by referring to the motion of material governed by equations derived from fluid mechanics. It is difficult to develop a proper constitutive model for the motion of granular material under shear, since the grains can behave like a solid, a liquid or a gas (Jop et al., 2006). The flow behaviour has been described in many ways as Newtonian material, Non-Newtonian material, dry Mohr-Coulomb material, two-phase material, etc (Bagnold, 1954; Chen, 1988; Pitman and Le, 2005; Savage and Hutter, 1989). Additionally, the sliding landslides can be treated as rigid-like blocks, which

interact with each other following the Newton's second law (e.g., Hungr, 1995; Tinti et al., 1997).

The landslide associated with rainfall effects and seismic loading have triggered a lot of specific researches. Intensive rainfall causes the variations of pore water pressure and effective stress, leading to the deformation of pre-failure stage of landslides. It has been proposed by Caine (1980) that the occurrence of shallow landslides and debris flows are controlled by the rainfall intensive-duration threshold. Further, different rainfall thresholds have been proposed to build a relationship between the threshold and the database of rainfall-induced landslides. The analyses are carried out focusing on the explanation of pore water pressure contributing to the failure of saturated/unsaturated slopes (Collins and Znidarcic, 2004). As for the earthquake-induced landslides, they are related to the earth surface processes initialized by seismic waves. Most moderate and large earthquakes can trigger landslides, ranging from small scales in soil to massive rock avalanches and two recent events, i.e. the 1999 Chi-Chi, earthquake and the 2008 Wenchuan, earthquake, have provided numerous cases for the understanding of seismic effects on earth surface processes (Fan et al., 2019). The failure of earthquake-induced landslides is mainly attributed to the dynamic stresses and the discontinuities inside the slope body.

To quantify the relationships between the response of slopes and the triggering causes, mathematical model is needed to describe these factors. According to Van Asch et al. (2007), the mathematical model should include the following features:

- geometrical: characterizing local geometry and internal structure;
- morphostructural: identifying evidences of mass movements by remote sensing or field works;
- kinematic: specifying control factors varying in time;
- geotechnical: describing physical and hydrological properties of material;
- geomechanical: merging these features with their supportive data in mathematical form.

Various information associated with multiple strategies should be included into the mathematical model. Due to the complexity of the mathematical models, they are most often solved by means of numerical techniques.

1.2 Numerical techniques

The widely used landslide modelling techniques mainly focus on the failure mechanism and the propagation stage of landslides. For the failure mechanism, the landslide is commonly analysed by e.g., the limit equilibrium method (Fredlund and Krahn, 1977), the limit analysis method (Chen, 2013), the finite-element method (Dawson et al., 1999), the discrete-element methods (Chang, 1992). For the landslide propagation stage, the landslide is considered as a mass-flow, which can be treated as a flow-like material based on equations derived from the fluid mechanics. The mass flow consists of rocks and poorly sorted sediments and water, rapidly moving across a steep-slope region and mainly driven by gravity force. This mass-flow dynamics has attracted great interest from scientists and engineers due to its high velocity and impact forces, and consequently to its high damaging power.

To minimize the damage of landslides, it is important to study the post-failure stage of the landslide. The post-failure stage hereafter denotes the evolution processes after the failure of landslides. On the basis of the fundamental work by Savage and Hutter (1989), where the mass-flow is treated as a shallow-flow model with the Mohr-Coulomb rheology law, most of the current models are still using a set of depth-averaged equations derived from the principles of mass and momentum conservation to describe the mass flow behaviours with various emphasises, e.g., single-phase debris flows (Chen, 1988), two-fluid debris flows (Pitman and Le, 2005) and two-layer approach (Fernández-Nieto et al., 2008). These models consider the landslide propagation that starts from rest assuming that the slip surface is known, being determined by a previous slope stability analysis or field surveys. With the aim of risk assessment of landslide hazards, the depth-averaged models can be integrated into GIS-based environment suitable for quick risk assessment of rapid mass flows released from a defined area (e.g., Mergili et al., 2017).

Based on the capability of modelling large deformation problems in geomechanics, the modern numerical techniques provide the opportunity to simulate the failure and post-failure mechanism via a single simulation. The numerical approaches applied to landslide modelling can be classified into three types: discontinuous approaches, continuous approaches, and the coupled approaches.

For discontinuous approaches, the Discrete Element Method (DEM) is probably the most used method, where the Newton's law is applied to govern the discretized elements considering the internal interactions and different force-displacement relationships. Different models of force-displacement laws account for the dynamics of individual discretized elements and they have been applied to modelling of the post-failure stage of landslide with successes (e.g., Staron, 2008; Tang et al., 2009). The main limitation of the DEM is its high computational cost.

As regards continuous approaches, they can be simply categorized into mesh-based approaches and mesh-free approaches. FDM, FVM (Finite Volume Method) and FEM are the most used mesh-based approaches. Another typical technique of the mesh-based approaches is the Arbitrary Lagrangian Eulerian (ALE) method. According to the ALE description (Donea et al., 1982), the mesh nodes can move arbitrarily to optimize the shapes of elements to avoid mesh distortion. The ALE description can be reduced to the Lagrangian-based FEM method by moving mesh with material or the Eulerian-based FEM by fixing mesh in the space. An example can be found in the work by Di et al. (2007), where a standard step of the ALE algorithm consists of a Lagrangian step and a Eulerian step. The governing equations are solved in the Lagrangian step and then mesh smoothing and variable mapping are performed in the Eulerian step. One limitation of the ALE is that it cannot treat adequately cases where extreme deformations are involved.

The mesh-free approaches associated with some other mesh-based particle methods can be generalized as particle approaches including the Smoothed Particle Hydrodynamics (SPH) (Bui et al., 2008), Material point method (MPM) (Andersen and Andersen, 2010) and particle finite element method (PFEM) (Idelsohn et al., 2003). SPH is a typical mesh-free approach that was originally proposed by Lucy (1977) and Gingold and Monaghan (1977) for astrophysical problems. The idea of SPH is to follow particles that carry physical quantities. The interpolation is carried out based on the particle position vector, using a weighting function ('kernel'), being a differentiable, decreasing, compactly supported function of the particle distance and the characteristic length, h , known as the smoothing length (Violeau and Rogers, 2016). MPM is a hybrid Eulerian-Lagrangian approach, where the moving material points carry state variables and the fixed Eulerian meshes are used to determine incremental displacements and stains at material points. The idea of PFEM (Idelsohn et al., 2004) is that the mesh nodes of the FEM mesh can move freely and even separate from the original mesh they belong to. The alpha-shape method is used to recognize the computational domain and FEM-solvers are used to update the positions of those particles. For other numerical approaches applied to large deformation analysis including landslides applications, one can referred to Soga et al. (2015).

1.3 Motivation and objectives of this work

The processes of landslides are often associated with complex geological conditions and intensive rainfalls and seismic shaking are known to be the main triggering factors for the failure of a slope. Slope failure mechanism depends on many geotechnical, hydrological, geomorphological, and physical factors, which are hard to be all included in numerical

models. So far, the phases of the onset and of the evolution are treated separately in numerical models, which means that the studies are carried out from different points of view. With the development of modern numerical techniques, especially of the strategies handling large deformation problems, it has become possible to simulate the whole landslide process covering pre-failure and post-failure analyses. The aim of this work is to study landslides onset and dynamics by adopting a unified approach where slope stability, identification of unstable zone, failure propagation, detaching processes and detached mass motion can be simulated by means of a comprehensive model considering complex factors.

To develop a model for landslide processes that can be used to predict the unstable zone and the landslide deposit considering various effects, the primary work is to assess the capability of the adopted numerical techniques in the model. As regards this aspect, it has been already mentioned above that several numerical techniques can be considered for the simulation of landslides involving large deformations. One relevant additional factor qualifying the goodness of a model is that it should be easily developed and integrated into the geoscientific models that are applied for the risk assessment of landslides. In practice, the numerical method should be easy to use for all those researchers that are not familiar with advanced numerical techniques and that like to adapt it to solve their own specific problems. Taking into account these considerations, the PFEM, which can be regarded as the particle version of the classical FEM, has been chosen as the basic numerical method to treat landslides into this work. It is known that the PFEM model can be developed based on different FEM solvers. An optimization-based PFEM relying on the robustness of available optimization solvers has been developed here by constructing optimization problems submitted to the solvers, which allows researchers to develop their own version.

With these objectives, a model that solves depth-averaged equations (DAEs) is first introduced, since various DAEs have been widely applied to the landslide modelling focusing on run-out analysis. The DAEs model has also been treated as a reference in the following sections, which thereby gives the structure of this thesis. In chapter 2, the basic concepts of the widely used depth-averaged equations (DAEs) are introduced and a finite difference scheme is developed to solve the DAEs. The numerical code is tested against typical benchmarks and a real case, i.e. the 1783 Scilla landslide, Italy, with comparisons carried out against a Lagrangian block model (Tinti et al., 1997) and against observation data. In chapter 3, the numerical implementation of the mathematical optimization-based PFEM is explained, where some key aspects are unveiled. In chapter 4, an assessment of the developed PFEM model applied to landslide modelling is conducted by comparing the results with typical techniques in slope stability and landslide propagation analyses. In chapter 5, the idea of simulating the landslide process via a single simulation is carried out based on a real case,

i.e., the 2013 Cà Mengoni landslide, northern Apennines, Italy. By the back-analysis of the landslide, it is found that in general, the model can capture the shallow movement of the landslide, but a weakening of the material should be included during the post-failure process. In chapter 6, the effects of seismic loading are explored and large deformation analyses of soil slopes impacted by seismic waves are performed.

Chapter 2

Depth-averaged models

Earth-surface mass flows such as debris flows and rock avalanches can result from slope failures. Both solid and fluid phases act together, often with extremely destructive power. According to the feature of this flow-like property, the corresponding mathematical models are usually constructed based on the principles of fluid mechanics. Due to the complexity of the mixture material behaviour under motion, quantitative descriptions are built with some assumptions to simplify the mass-flow motions. The scaling technique assuming that the depth scale is much smaller than the length scale and the depth average technique assuming that the relevant variables are the average quantities along depth are the two most frequently adopted techniques, leading to the so called depth-averaged models. They have been widely applied to many flow-like phenomenon including flood propagation, landslide run-out analysis, tsunamis generation, and so on. This chapter is presented with two aims: (1) explaining the basic idea of the depth-averaged models; (2) introducing the developed finite difference code and validating it against benchmarks and real cases. It is pointed out that only a succinct description, though complete and exhaustive, is given here since most contents have been included in a paper (Wang et al., 2019a) that is one of the products of this thesis work.¹ We stress also that this model will be further compared with the developed PFEM model in the following chapters.

2.1 Governing equations

The governing equations of the depth-averaged models, also called depth-averaged equations (DAEs), are derived from the Navier-Stokes equations using depth-integration technique.

¹Most contents in this section have been summarized in a paper published in: Wang L, Zaniboni F, Tinti S, et al. Reconstruction of the 1783 Scilla landslide, Italy: numerical investigations on the flow-like behaviour of landslides[J]. *Landslides*, 2019, 16(6): 1065-1076.

The shallow-water approximation (long-wave approximation) assumes that the vertical velocity scale is negligibly small compared to the horizontal velocity scale, which leads to the appearance of the shallow water equations (SWEs). Incorporating the Mohr-Coulomb rheology law into the SWEs, the model developed by Savage and Hutter (1989) has been widely used and further extended by many researchers. The modifications on the classical SWEs have been conducted to describe different mechanisms during the motion of mass flows (e.g. Gray and Thornton, 2005; Iverson, 2005; Mangeney et al., 2005; Pudasaini, 2012). The governing equations in this chapter are restricted to the basic equations that express the conservation law of mass and of linear momentum for a two-phase mixture.

2.1.1 Balance equations

On the basis of the Eulerian description, let's consider the flow motion through a volume V in space bounded by the surface S . Assuming that the out direction of V is positive, then the mass change within V can be attributed to two components:

- the continuum flows out $\int_S \rho \mathbf{u}_n dS$, where \mathbf{u}_n is the velocity normal to S and ρ is the density
- the variation of density within V $\int_V \frac{\partial \rho}{\partial t} dV$

Since mass is conserved: $\Delta m = \int_V \frac{\partial \rho}{\partial t} dV + \int_S \rho \mathbf{u}_n dS = 0$, using the divergence theorem, we can get the following equations inside the volume V :

$$\int_V \left(\frac{\partial \rho}{\partial t} + \nabla \cdot (\rho \mathbf{u}) \right) dV = 0 \quad (2.1)$$

Let's assume a mixture consisting of fluid and solid phases with components denoted by the volume fractions α_s and α_f . Hereafter, the subscript s and f are used to denote the fluid and the solid phases. The mass conservation is valid for both phases, with two simplified conditions:

- no phase change $\frac{dm_i}{dt} = 0 (i = s, f)$
- two phases are individually incompressible $\frac{\partial \rho_i}{\partial t} = 0 (i = s, f)$

The simplified mass conservation equations be written as:

$$\frac{\partial (\rho_s \alpha_s)}{\partial t} + \nabla \cdot (\rho_s \alpha_s \mathbf{u}_s) = 0 \quad (2.2a)$$

$$\frac{\partial (\rho_f \alpha_f)}{\partial t} + \nabla \cdot (\rho_f \alpha_f \mathbf{u}_f) = 0 \quad (2.2b)$$

Similarly, we can obtain a momentum conservation equation based on the Newton's second law, stating that the momentum change is produced by forces. Considering that:

- the rate of momentum

$$\int_V \frac{\partial(\rho \mathbf{u})}{\partial t} dV$$

- the flow out of momentum (" \otimes " represents the tensor product)

$$\int_S (\rho \mathbf{u} \otimes \mathbf{u}) dS$$

- and the forces

One can obtain the momentum conservation equations:

$$\frac{\partial(\rho_s \alpha_s \mathbf{u}_s)}{\partial t} + \nabla(\alpha_s \rho_s \mathbf{u}_s \otimes \mathbf{u}_s) = \alpha_s \rho_s \mathbf{g} - \nabla \mathbf{T}_s + \mathbf{f}_s - \alpha_s \nabla p \quad (2.3a)$$

$$\frac{\partial(\rho_f \alpha_f \mathbf{u}_f)}{\partial t} + \nabla(\alpha_f \rho_f \mathbf{u}_f \otimes \mathbf{u}_f) = \alpha_f \rho_f \mathbf{g} + \nabla \mathbf{T}_f + \mathbf{f}_f + \alpha_s \nabla p \quad (2.3b)$$

Here the complex interactive forces (e.g. Pudasaini, 2012) are simplified as the drag force term \mathbf{f}_d between the solid and fluid phases, leading to the expressions: $\mathbf{f}_s = \mathbf{f}_d, \mathbf{f}_f = -\mathbf{f}_d$ (Meng and Wang, 2016). \mathbf{T}_s and \mathbf{T}_f are the partial stress tensors of granular and fluid phases. p is the fluid pressure and \mathbf{g} is the gravitational acceleration.

Stress tensors

The buoyancy force exerted on solid phase is $-\alpha_s \nabla p$ and $\mathbf{T}_f = -p \mathbf{I} + \tau_f$. Thus we can obtain that $\nabla \mathbf{T}_f + \alpha_s \nabla p = -\alpha_f \nabla p + \nabla \tau_f$. Considering the Mohr-Coulomb model for solid phase and the Newtonian fluid model for the fluid phase, one can write $\mathbf{T}_s = \alpha_s \tilde{\mathbf{T}}_s$ with $\tilde{\mathbf{T}}_s$ being the Coulomb stress tensor for dry granular material. The partial shear stress is given by $\tau_f = \alpha_f \mu (\nabla \mathbf{u}_f + \nabla^T \mathbf{u}_f)$, where μ is the dynamic viscosity.

Mixture expression

The governing equations for two phases can be reduced to the classical Navier-Stokes equation for incompressible fluid if we add Eq. (2.3a) with Eq. (2.3b). Replacing $-\nabla \mathbf{T}_s$ by $\nabla \tau_f$ (compressive stress is positive for solid while negative for fluid), we have:

$$\frac{\partial(\rho \mathbf{u})}{\partial t} + \nabla(\rho \mathbf{u} \otimes \mathbf{u}) = \rho \mathbf{g} + \nabla \tau - \nabla p \quad (2.4)$$

2.1.2 Scaling analysis

According to the previous works (e.g. Gray et al., 1999; Pudasaini, 2012; Savage and Hutter, 1989), the above governing equations can be simplified with the introduction of dimensionless variables:

$$(x, y, z, b, s, t) = L(\hat{x}, \hat{y}, \varepsilon \hat{z}, \varepsilon \hat{b}, \varepsilon \hat{s}, 1/\sqrt{gL}\hat{t}) \quad (2.5a)$$

$$(u, v, w) = \sqrt{gL}(\hat{u}, \hat{v}, \varepsilon \hat{w}) \quad (2.5b)$$

$$(p) = \rho_f g H \hat{p}, (C_d) = \rho_f \sqrt{g/L} \hat{C}_d \quad (2.5c)$$

$$(T_{s(ii)}) = \rho_s g H \hat{T}_{s(ii)}, (T_{s(ij)}) = \rho_s g H \hat{T}_{s(ij)} \quad (2.5d)$$

Here H and L are the introduced characteristic depth and horizontal length respectively and the superscript $\hat{}$ represents the non-dimensionalized variables. u, v, w are the down-slope (x), cross-slope (y) and normal (z) components of the velocity. $\varepsilon = H/L$ is the aspect ratio and $\mathbf{T}_{s(ij)}$ are the components of the solid stress tensor.

2.1.3 Depth-averaged equations

By means of the scaling analysis technique, the governing equations can be simplified as dimensionless equations. The continuity equations Eqs. (2.2) are naturally converted as (Hereafter, the superscript $\hat{}$ is omitted for convenience):

$$\frac{\rho_s \sqrt{gL}}{L} \left(\frac{\partial(\alpha_s)}{\partial t} + \nabla(\alpha_s \mathbf{u}_s) \right) = 0 \quad (2.6a)$$

$$\frac{\rho_f \sqrt{gL}}{L} \left(\frac{\partial(\alpha_f)}{\partial t} + \nabla(\alpha_f \mathbf{u}_f) \right) = 0 \quad (2.6b)$$

As for the momentum equations, the following equations are separately expressed for the solid and the fluid phases.

Fluid: The components of terms along x, y and z directions are listed inside the equations:

$$\frac{\partial(\rho_f \alpha_f \mathbf{u}_f)}{\partial t} \left\{ \begin{array}{l} \frac{\rho_f g L}{L} \frac{\partial \alpha_f u_f}{\partial t} \\ \frac{\rho_f g L}{L} \frac{\partial \alpha_f v_f}{\partial t} \\ \varepsilon \frac{\rho_f g L}{L} \frac{\partial \alpha_f w_f}{\partial t} \end{array} \right. \quad (2.7)$$

$$\nabla(\rho_f \alpha_f \mathbf{u}_f \otimes \mathbf{u}_f) \left\{ \begin{array}{l} \frac{\rho_f g L}{L} \left(\frac{\partial(\alpha_f u_f^2)}{\partial x} + \frac{\partial(\alpha_f u_f v_f)}{\partial y} + \frac{\partial(\alpha_f u_f w_f)}{\partial z} \right) \\ \frac{\rho_f g L}{L} \left(\frac{\partial(\alpha_f u_f v_f)}{\partial x} + \frac{\partial(\alpha_f v_f^2)}{\partial y} + \frac{\partial(\alpha_f v_f w_f)}{\partial z} \right) \\ \varepsilon \frac{\rho_f g L}{L} \left(\frac{\partial(\alpha_f u_f w_f)}{\partial x} + \frac{\partial(\alpha_f v_f w_f)}{\partial y} + \frac{\partial(\alpha_f w_f^2)}{\partial z} \right) \end{array} \right. \quad (2.8)$$

$$-\alpha_f \nabla p \left\{ \begin{array}{l} -\frac{\rho_f g H}{L} \alpha_f \frac{\partial p}{\partial x} \\ -\frac{\rho_f g H}{L} \alpha_f \frac{\partial p}{\partial y} \\ -\frac{\rho_f g H}{H} \alpha_f \frac{\partial p}{\partial z} \end{array} \right. \quad (2.9)$$

Assuming a linear drag relationship for the drag force term $\mathbf{f}_d = C_d \alpha_s \alpha_f (\mathbf{u}_f - \mathbf{u}_s)$, one can write

$$-\mathbf{f}_d \left\{ \begin{array}{l} \rho_f g C_d \alpha_f \alpha_s (u_f - u_s) \\ \rho_f g C_d \alpha_f \alpha_s (v_f - v_s) \\ \varepsilon \rho_f g C_d \alpha_f \alpha_s (w_f - w_s) \end{array} \right. \quad (2.10)$$

Newtonian rheology is adopted for the fluid, i.e. $\boldsymbol{\tau}_f = \eta_f (\nabla \mathbf{u}_f + \nabla^T \mathbf{u}_f)$:

$$\nabla \boldsymbol{\tau}_f \left\{ \begin{array}{l} \frac{\varepsilon}{N_R} \left[2 \frac{\partial^2 u_f}{\partial x^2} + \frac{\partial}{\partial y} \left(\frac{\partial v_f}{\partial x} + \frac{\partial u_f}{\partial y} \right) + \frac{1}{\varepsilon^2} \frac{\partial^2 u_f}{\partial z^2} + \frac{\partial^2 w_f}{\partial x \partial z} \right] \\ \frac{\varepsilon}{N_R} \left[2 \frac{\partial^2 v_f}{\partial y^2} + \frac{\partial}{\partial x} \left(\frac{\partial v_f}{\partial x} + \frac{\partial u_f}{\partial y} \right) + \frac{1}{\varepsilon^2} \frac{\partial^2 v_f}{\partial z^2} + \frac{\partial^2 w_f}{\partial y \partial z} \right] \\ \mathcal{O} \end{array} \right. \quad (2.11)$$

in which $N_R = (\rho_f H \sqrt{g L}) / (\alpha_f \eta_f)$ that is similar to the Reynold number. The z component of the stress is omitted.

Solid: The same procedures can be applied to the stresses exerted on solid phases.

Depth-integration technique

$$\frac{1}{h} \int_{b(x,y)}^{s(x,y,t)} (\cdot) dz = \overline{(\cdot)} \quad (2.12)$$

Leibniz integral rule

$$\begin{aligned} \frac{d}{dx} \left(\int_{a(x)}^{b(x)} f(x,t) dt \right) &= f(x,b(x)) \frac{d}{dx} b(x) - f(x,a(x)) \frac{d}{dx} a(x) \\ &+ \int_{a(x)}^{b(x)} \frac{\partial}{\partial x} f(x,t) dt \end{aligned} \quad (2.13)$$

With further simplifications, e.g. shallow water assumptions (hydrostatic), the depth-averaged equations (DAEs) can be obtained for the two-phase modelling. Different modifications

(boundary conditions, interaction forces, etc.) can result in different equations (e.g. Meng and Wang, 2016; Pitman and Le, 2005; Pudasaini, 2012) describing different mechanisms. These equations can be reduced to the simple mixture models (e.g. Iverson and Denlinger, 2001; Savage and Hutter, 1989), but, for simplicity, the details and final forms of these DAEs are not presented here. Instead, the DAEs adopted to simulate landslide propagation in the thesis will be introduced in the next sections.

2.2 Numerical scheme

The resulting partial differential equations can be solved by means of various numerical techniques. With the advantages of easily understood and implemented, FDM has been served for solving these equations for a quite long time. The numerical scheme presented here follows the one proposed by Tai et al. (2002). The numerical scheme combines a first-order Lax-Friedrichs scheme (Lax, 1954) with a piecewise linear reconstruction. The central Nessyahu-Tadmor (NT) scheme (Nessyahu and Tadmor, 1990), computing the staggered cell averages at the interfacing break-points, is adopted since it possesses the advantage of the simplicity of a Riemann-solver-free approach. The cell average and the linear reconstruction techniques of the NT scheme that is written in a conservative form to automatically satisfy the conservation properties of the original equations are explained in this section. The conservation equations are integrated in both time and space in discrete form to be solved by the code. The staggered grid algorithm is implemented to control spurious oscillations, which are further reduced using a suitable flux limiter method. The numerical scheme based on the fixed Cartesian grid (Eulerian approach) and identifying the shocks by the regions with large gradients, is a so-called shock capturing scheme.

2.2.1 Cell average

In order to explain our numerical scheme better we use a 1D case first, where the governing equations take the form:

$$u_t(x,t) + f_x(u(x,t)) = s(u(x,t)) \quad (2.14)$$

Here u is the conservative variable, f is the momentum flux along x direction and s is the source term. Hereafter, the subscripts t, x represent derivatives with respect to the time and x

directions. To solve this problem, the idea of cell average is applied on a staggered grid.

$$\begin{aligned} U_i^n &= \frac{1}{\Delta x} \int_{x_{i-\frac{1}{2}}}^{x_{i+\frac{1}{2}}} u(x, t^n) dx, \\ U_{i+\frac{1}{2}}^n &= \frac{1}{\Delta x} \int_{x_i}^{x_{i+1}} u(x, t^n) dx \end{aligned} \quad (2.15)$$

Here, U denotes cell-average values. The subscript i and the superscript n represent at the i th node and at the current state respectively. The center of the interval $(x_{i-1/2}, x_{i+1/2})$ is x_i , and the interval is named as cell I_i . Thus, the interval of (x_i, x_{i+1}) is naturally denoted as cell $I_{i+1/2}$. Taking the cell I_i as an example and integrating the hyperbolic equations in time over the interval (t^n, t^{n+1}) and in space over the interval $(x_{i-\frac{1}{2}}, x_{i+\frac{1}{2}})$, one obtains:

$$\begin{aligned} & \int_{x_{i-\frac{1}{2}}}^{x_{i+\frac{1}{2}}} \int_{t^n}^{t^{n+1}} u_t(x, t) dx dt = \\ & - \int_{x_{i-\frac{1}{2}}}^{x_{i+\frac{1}{2}}} \int_{t^n}^{t^{n+1}} f_x(u(x, t)) dx dt + \int_{x_{i-\frac{1}{2}}}^{x_{i+\frac{1}{2}}} \int_{t^n}^{t^{n+1}} s(u(x, t)) dx dt \end{aligned} \quad (2.16)$$

that can be easily written as:

$$\begin{aligned} & \int_{x_{i-\frac{1}{2}}}^{x_{i+\frac{1}{2}}} u(x, t^{n+1}) dx = \int_{x_{i-\frac{1}{2}}}^{x_{i+\frac{1}{2}}} u(x, t^n) dx \\ & - \int_{t^n}^{t^{n+1}} \left(f(u(x_{i+\frac{1}{2}}, t)) - f(u(x_{i-\frac{1}{2}}, t)) \right) dt + \int_{x_{i-\frac{1}{2}}}^{x_{i+\frac{1}{2}}} \int_{t^n}^{t^{n+1}} s(u(x, t)) dx dt \end{aligned} \quad (2.17)$$

The LHS and the first term of the RHS of the above equation can be further manipulated by the cell average technique:

$$\begin{aligned} & \int_{x_{i-\frac{1}{2}}}^{x_{i+\frac{1}{2}}} u(x, t^{n+1}) dx = \Delta x U_i^{n+1} \\ & \int_{x_{i-\frac{1}{2}}}^{x_{i+\frac{1}{2}}} u(x, t^n) dx = \frac{\Delta x}{2} u_{i-\frac{1}{4}}^n + \frac{\Delta x}{2} u_{i+\frac{1}{4}}^n \end{aligned} \quad (2.18)$$

As for the other terms in the RHS, they similarly can be transformed to:

$$\int_{t^n}^{t^{n+1}} \left(f(u(x_{i+\frac{1}{2}}, t)) - f(u(x_{i-\frac{1}{2}}, t)) \right) dt = \Delta t \left(f(u_{i+\frac{1}{2}}^{n+\frac{1}{2}}) - f(u_{i-\frac{1}{2}}^{n+\frac{1}{2}}) \right) \quad (2.19)$$

$$\int_{x_{i-\frac{1}{2}}}^{x_{i+\frac{1}{2}}} \int_{t^n}^{t^{n+1}} s(u(x,t)) dx dt = \frac{\Delta t \Delta x}{2} \left(s(u_{i+\frac{1}{4}}^{n+\frac{1}{2}}) + s(u_{i-\frac{1}{4}}^{n+\frac{1}{2}}) \right) \quad (2.20)$$

where u_i^n is used to denote $u(x_i, t^n)$.

By a piecewise linear approximation, we can assume that:

$$u_{i\pm\frac{1}{4}}^n = u_{i\pm\frac{1}{2}}^n \mp \frac{\Delta x}{4} (u_x)_{i\pm\frac{1}{2}}^n \quad (2.21)$$

Further, the values at half-time step can be similarly predicted by Taylor's expansion and the original equation Eq. (2.14):

$$\begin{aligned} u_{i\pm\frac{1}{2}}^{n+\frac{1}{2}} &= u_{i\pm\frac{1}{2}}^n + \frac{\Delta t}{2} (u_t)_{i\pm\frac{1}{2}}^n \\ &= u_{i\pm\frac{1}{2}}^n - \frac{\Delta t}{2} (f_x)_{i\pm\frac{1}{2}}^n + \frac{\Delta t}{2} (s)_{i\pm\frac{1}{2}}^n \end{aligned} \quad (2.22)$$

$$u_{i\pm\frac{1}{4}}^{n+\frac{1}{2}} = u_{i\pm\frac{1}{2}}^{n+\frac{1}{2}} \mp \frac{\Delta x}{4} (u_x)_{i\pm\frac{1}{2}}^{n+\frac{1}{2}} \quad (2.23)$$

Therefore the cell average values U_i^{n+1} can be obtained from the original values at the previous time step at the nodes $x_{i-\frac{1}{2}}, x_{i+\frac{1}{2}}$ denoted as $u_{i\mp\frac{1}{2}}^n$. Based on the present scheme, on integrating values in the intervals $I_{i+1/2}$ and I_i , the values of the original nodes can be updated after two time steps. Figure 2.1 explains the procedure of the time advance process.

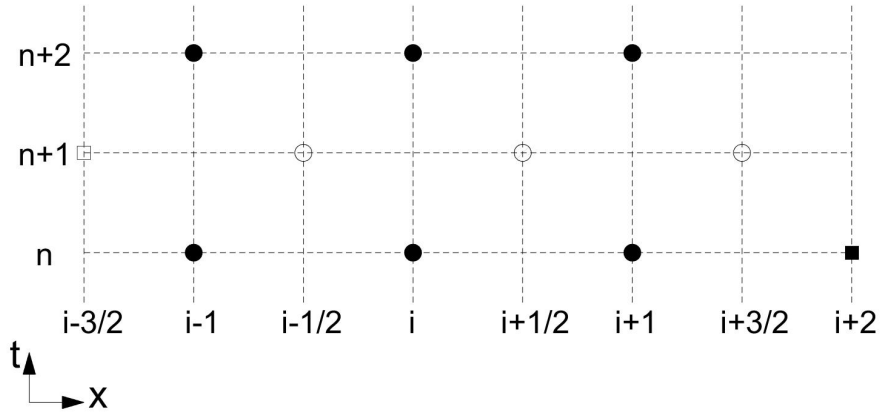


Fig. 2.1 Stencil for 1D cases.

Assume that the initial computational domain includes three values u_{i-1}^n , u_i^n and u_{i+1}^n , denoted as black-filled circles. With the information at a ghost node u_{i+2}^n shown as a black-filled rectangle, the values of middle points $u_{i-1/2}^{n+1}$, $u_{i+1/2}^{n+1}$ and $u_{i+3/2}^{n+1}$, marked as unfilled circles can be obtained by the mentioned strategy. Moreover, with the values at another ghost node $u_{i-3/2}^{n+1}$ marked as an unfilled rectangle, the values at original domain are obtained at the next time step, which are denoted as u_{i-1}^{n+2} , u_i^{n+2} and u_{i+1}^{n+2} . Therefore, the time advance process of the conservative variable is achieved.

2.2.2 Flux limiter

To attenuate possible spurious oscillations in the numerical solution, a flux limiter method is applied to conduct the second-order piecewise linear reconstructions. The cell average derivative is determined by a generalized minmod-like limiter involving a parameter θ (Kurganov and Tadmor, 2000).

$$(u_x)_i^n = MM\left(\theta \frac{u_i^n - u_{i-1}^n}{\Delta x}, \frac{u_{i+1}^n - u_{i-1}^n}{2\Delta x}, \theta \frac{u_{i+1}^n - u_i^n}{\Delta x}\right) \quad (2.24)$$

where θ is a predefined parameter and $1 \leq \theta \leq 2$. MM denotes the function of the minmod limiter expression. For the present flux limiter involving three values, i.e. $MM(z_1, z_2, z_3)$:

$$\minmod(z_1, z_2, z_3) = \begin{cases} \min\{z_1, z_2, z_3\}, & \text{if } z_{1,2,3} > 0 \\ \max\{z_1, z_2, z_3\}, & \text{if } z_{1,2,3} < 0 \\ 0, & \text{otherwise.} \end{cases}$$

2.2.3 Stability condition

The CFL (Courant-Friedrichs-Lewy) stability condition is used to ensure that the maximum phase velocity c_{max} is always smaller than the speed associated with the grid, i.e. $\Delta x/\Delta t$, and gives the expression of the adaptive time step for solving the governing equations:

$$\Delta t \leq k \frac{\Delta x}{c_{max}} \quad (2.25)$$

$$c_{max} = \max_{\forall i} (|\lambda_i^{(min)}|, |\lambda_i^{(max)}|) \quad (2.26)$$

where $\lambda_i^{(min)}$ and $\lambda_i^{(max)}$ are the minimum and maximum eigenvalues of the Jacobian matrix $(\partial \mathbf{F} / \partial \mathbf{U})_i^n$. The parameter k is usually taken less than 1/0.5 for the NT scheme applied to

1D/2D cases, and $k = 0.475$ for 2D simulations is suggested by the numerical experiments conducted by Jiang and Tadmor (1998).

2.2.4 Extension to two-dimensional cases

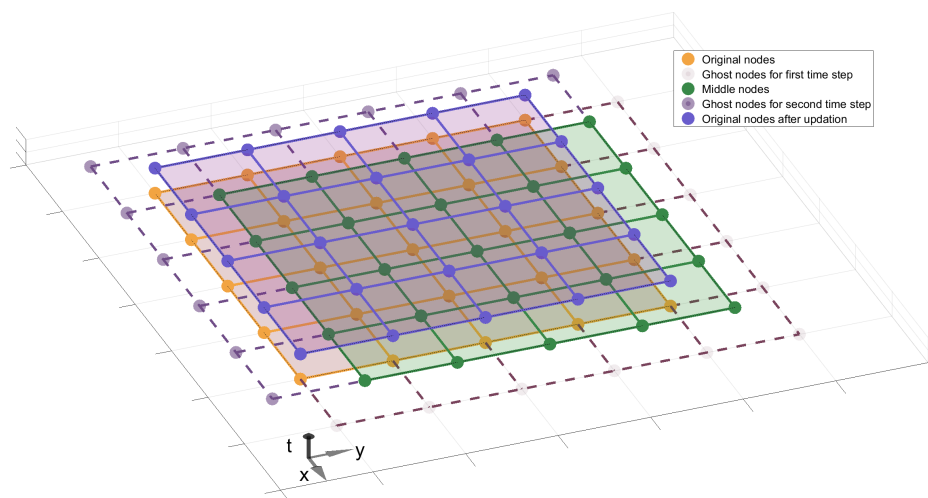


Fig. 2.2 Stencil for 2D cases.

With a 2D cell, the formulas given in the previous section have to be adapted to cover both space directions. Each loop of calculation is divided into two time steps. In the first time step, the values of cell average, denoted as $U_{i+1/2,j+1/2}^{n+1}$ are updated from the original nodal values, denoted as $u_{i,j}^n$. In the second time step, the values of cell average $U_{i,j}^{n+2}$ are updated from the values $u_{i+1/2,j+1/2}^{n+1}$ obtained from the first time step. Thus, the values at the original nodes are updated every two time-steps calculations. Figure 2.2 illustrates this procedure. The values at the original nodes $u_{i,j}^n$ are shown as orange points, and the region defined by orange solid lines is the computational domain. By means of the mentioned numerical scheme, cell average values at $U_{i+1/2,j+1/2}^{n+1}$ (green nodes) can be obtained with the help of ghost nodes for the first time step. Let values at the nodes be equal to the obtained cell average values, that is $u_{i+1/2,j+1/2}^{n+1} = U_{i+1/2,j+1/2}^{n+1}$. By one more time step, all the values at original nodes $u_{i,j}^{n+2}$ can be successfully updated (shown as blue nodes). Naturally the information at the displayed ghost nodes are used.

2.3 Benchmarks

2.3.1 Classical 'dam-break' problem

The dam-break problem is a classical benchmark for shock-capturing numerical schemes, and has been widely used also for validating mass flow models. The analytical solution of this kind of Saint-Venant equations is reviewed in Faccanoni and Mangeney (2013). The governing equations can be given the following form:

$$\vec{U} = \begin{bmatrix} h \\ hu \end{bmatrix}; \quad \vec{F} = \begin{bmatrix} hu \\ hu^2 + \frac{1}{2}gh^2 \end{bmatrix}; \quad \vec{G} = 0; \quad \vec{S} = 0 \quad (2.27)$$

where h is the height of water, $g = 9.81 \text{ m/s}^2$ is the gravity acceleration, u is the x direction velocity. The initial condition is that the water is still and its level has an abrupt jump from the higher constant value h_1 to the lower constant value h_2 . Very many experiments have been run that all gave very satisfactory results. What we show here refers to the same configuration treated by Louaked and Hanich (1998), i.e. the initial upstream depth is set to $h_1 = 1.0 \text{ m}$ and the downstream depth is set as $h_2 = 10^{-6} \text{ m}$. The adopted fixed space step is $\Delta x = 0.01 \text{ m}$. The numerical and analytical solutions for a specific time $t = 0.1 \text{ s}$ are compared in Fig. 2.3 (a-b) to show that the shock wave is well captured by the present method.

Another typical benchmark for mass flows is a debris mixture flowing over a rough slope inclined at an angle α , described by the following equations:

$$\vec{U} = \begin{bmatrix} h \\ hu \end{bmatrix}; \quad \vec{F} = \begin{bmatrix} hu \\ hu^2 + \frac{1}{2}\beta_x h^2 \end{bmatrix}; \quad (2.28)$$

$$\vec{G} = 0; \quad \vec{S} = \begin{bmatrix} 0 \\ hg \cos \alpha (\tan \alpha - \tan \delta) \end{bmatrix}$$

where $\beta_x = g \cos \alpha$ and δ is the basal friction angle. If lateral earth pressure is taken into consideration, we have $\beta_x = K_x g \cos \alpha$, where K_x is the lateral earth pressure coefficient (Savage and Hutter, 1989) along the x direction. The model adopted hereafter assumes that lateral earth pressure coefficient is equal to 1. The initial configuration of the 'dry bed' test case (the downstream water level $h_2 = 0.0 \text{ m}$) provided by Faccanoni and Mangeney (2013) is used, where $\alpha = 22^\circ$, $\delta = 21^\circ$ and the upstream water level is $h_1 = 0.1446 \text{ m}$. The mesh density of $\delta x = 0.01 \text{ m}$ is used. The results obtained from this numerical scheme at $t = 0.5 \text{ s}$ can be seen in Figure 2.3(c-d).

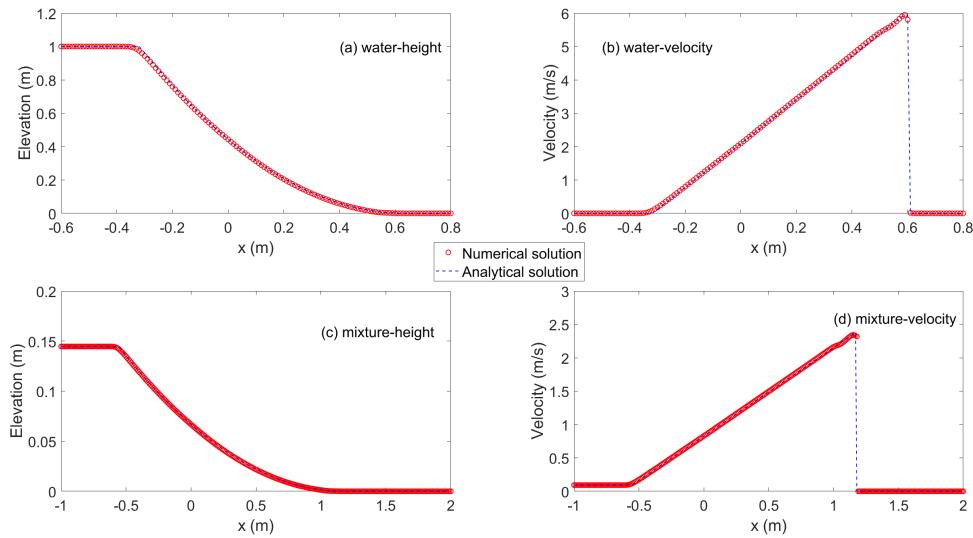


Fig. 2.3 Comparisons between numerical simulation and analytical solution of 1D 'dam-break' problems.

2.3.2 Two-dimensional 'dam-break' problem

The geometry of this problem is firstly used by Fennema and Chaudhry (1990), and has been widely adopted for testing numerical codes or new approaches, such as by Fagherazzi et al. (2004), Ouyang et al. (2013) and La Rocca et al. (2015). The computational domain is a 200-m-long and 200-m-wide channel with a thin dam that is located at the position of $(x, y) = (100\text{ m}, 0 - 200\text{ m})$ along the y direction. Water depth of the upstream and downstream region in the reservoir are 10 m and 5 m respectively. Assuming that a part of the dam, that is $(x, y) = (100\text{ m}, 95 - 170\text{ m})$, breaks instantaneously, the water upstream crashes into the reservoir with lower water depth. The wall condition is enforced at the boundary of the channel and at the non-breaking sector of the dam, where the velocities normal to the wall are set to zero. Contour and height profiles of water are given at $t = 7.2\text{ s}$ in Figures 2.4 and 2.5. Using coarse grids with a resolution of 2.5 m, and the results obtained with the present scheme agree well with the published results that can be found in Fagherazzi et al. (2004) and in the other aforementioned papers.

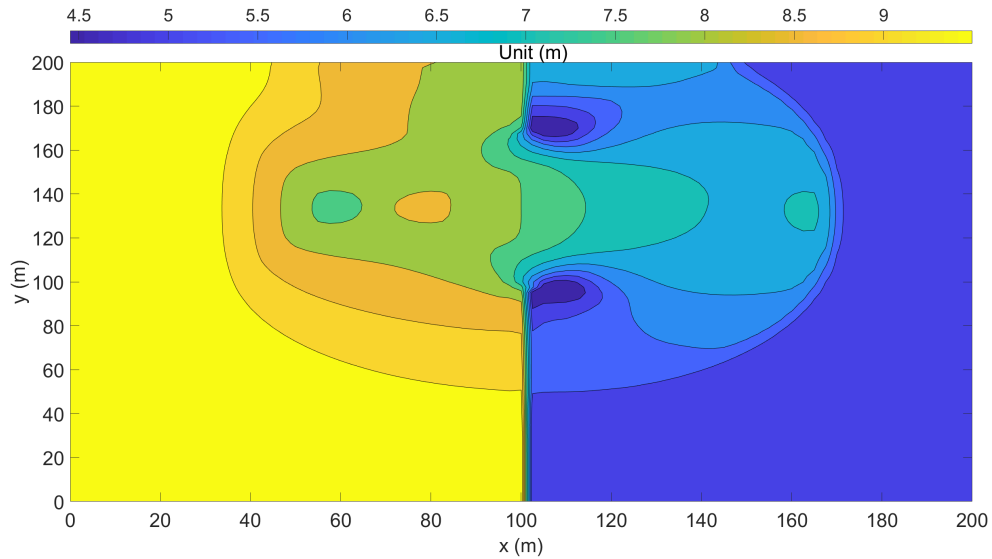


Fig. 2.4 Contour plot of the break at $t = 7.2$ s. Resolution for the simulation is set to 2.5m for both x and y directions.

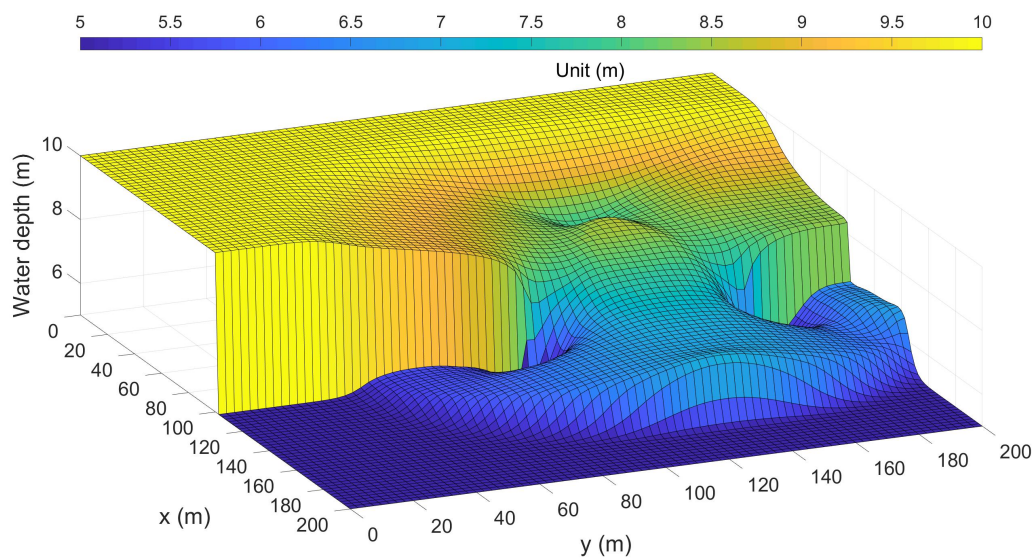


Fig. 2.5 Height profile of the water break $t = 7.2$ s.

2.3.3 Dam break over a triangle hump

The European project EU CADAM (European Union Concerted Action on Dam Break Modelling) provides a laboratory experiment for testing the capability of numerical schemes applied to a practical case. The set-up is a 38 m long horizontal domain with a dam located

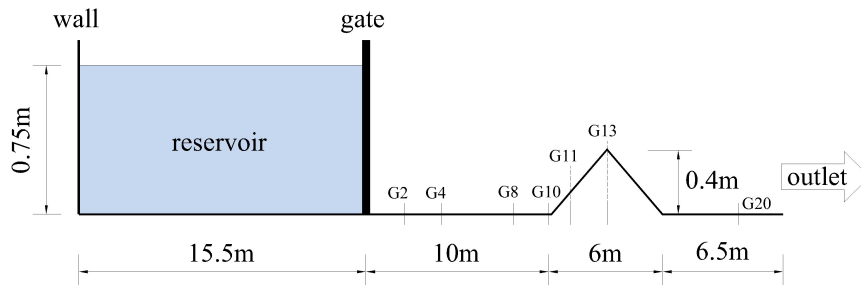


Fig. 2.6 Sketch of the set-up of the dam break experiment over a triangular hump.

at $x = 15.5\text{m}$. Seven gauges named G2, G4, G8, G10, G11, G13 and G20, located at $x = 17.5, 19.5, 23.5, 25.5, 26.5, 28.5,$ and 35.5m , were set to measure the time history of the water depth. Figure 2.6 illustrates the configuration of this experiment. To reproduce this experiment by the numerical code, the node separation is set to $\Delta x = 0.05\text{m}$ and the Manning coefficient $n = 0.0125\text{s/m}^{1/3}$ is adopted throughout the entire domain. On the left end a rigid wall condition is imposed, while on the right end the condition is a free flow. The computational time is set as 90s to be compared with the experimental data. After the sudden opening of the gate, the water in the reservoir rushes out and inundates the downstream domain. The generated water wave propagates along the domain over the basal topography, and several surges are observed at gauges. The water motion is affected by the gravity and friction. In Figure 2.7, great agreements have been achieved by the numerical results compared with the observation data. The arriving time and water depth of the various water pulses have been successfully predicted.

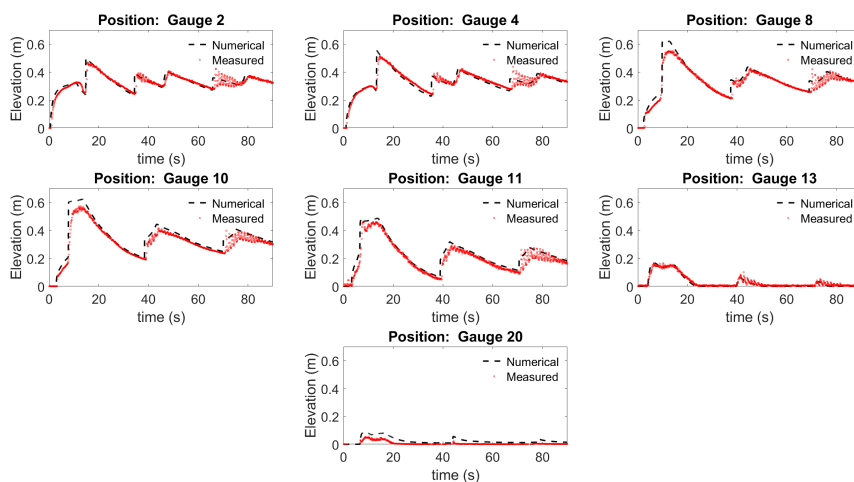


Fig. 2.7 Time histories of the water elevation at the seven gauges.

2.4 Investigation of the 1783 Scilla landslide

The narrow Messina Strait, located between the eastern tip of Sicily and the southern end of Calabria, connecting the Tyrrhenian Sea to the north with the Ionian Sea to the south, as shown in Figure 2.8A, is one of the most seismically active areas of southern Italy. Tectonically, it is dominated by the development of the Siculo-Calabrian Rift Zone and is the northernmost sector of the high level seismic belt including the largest earthquakes that have occurred in southern Italy in the last four centuries, such as the 1693 SE Sicily earthquakes, the 1783 Calabrian seismic sequence, the 1905 Monteleone earthquake and the Messina earthquake of 1908 (Catalano et al., 2008). The 1783 seismic crisis started with a sequence of strong earthquakes from February to March, exceeding magnitude M_w 7 (Rovida et al., 2011) and lasted for at least three years (1783-1785). It caused more than 30,000 casualties, destroyed 200 localities (Porfido et al., 2011), and triggered a further series of secondary disasters including numerous mass failures, river dams with temporary lake formation and tsunamis. The most catastrophic episode of this crisis in terms of death toll was the Scilla tsunami event, that was generated by an earthquake-induced landslide and that killed more than 1500 people on February 6, 1783. The landslide occurred at the south of the coastal village of Scilla. The earthquake regarded as the trigger of the landslide happened offshore in the Messina Strait and was a $M_w = 5.9$ aftershock of a strong shock occurred the day before. The mass failure took place about 30 minutes later, and a huge tsunami generated by the landslide crashing into the sea was observed soon after the mass collapse (Minasi, 1785). Available historical reports and studies provide the tsunami run-up heights and inundation distances, as summarized in Graziani et al. (2006). On the basis of recent field surveys of subaerial and submarine scars, the total volume involved in the failure was postulated to be 8 Mm^3 and the deposit was estimated as $5\text{-}6 \text{ Mm}^3$ (Bozzano et al., 2006, 2011).

Previous numerical studies of the Scilla event were carried out by Avolio et al. (2009); Mazzanti and Bozzano (2011) and Zaniboni et al. (2016) via different numerical techniques. The Scilla landslide in the first two papers was simulated by the cellular automata technique and by the DAN3D code (developed by Hungr and McDougall, 2009) respectively. The cellular automata technique is used to simulate the complex dynamic system, where the landslide consists of sub-blocks with interactions. The deposit of the Scilla landslide was reconstructed by Avolio et al. (2009), who however did not give any details on the landslide dynamics. The code DAN3D adopts a Lagrangian-based method to solve the DAEs, where a variety of basal rheological relationships, material entrainment and other features can be included. The conducted DAN3D simulations of the Scilla landslide described the motion of the submarine landslide through a turbulence coefficient considering the effects of underwater drag and frictions. The simulations revealed that the Scilla landslide accelerated to 45 m/s

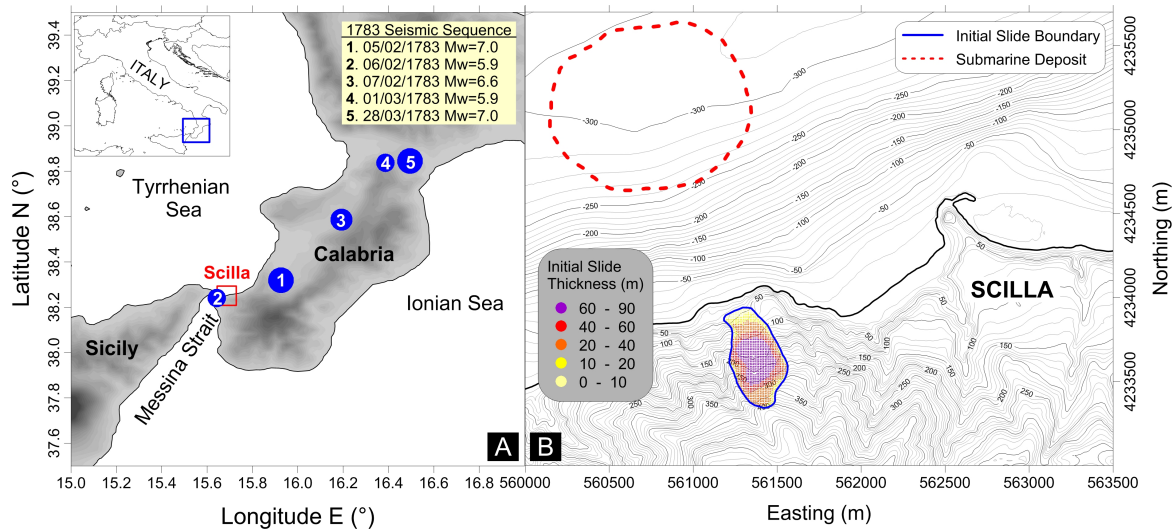


Fig. 2.8 **A** Geographical location of Scilla (red rectangle). **B** Area of the Scilla landslide.

after 20 s and decelerated to rest after 80 s. The computer deposit region was acceptably reproduced by Mazzanti and Bozzano (2011), but the dynamic evolution of the sliding mass was not presented in the paper. As for the last work mentioned above, it makes use of a 1D Lagrangian block model (Tinti et al., 1997), where the landslide mass is discretized into blocks that interact with each other. Forces including gravity, friction, drag and block-block interaction act on blocks, that are allowed to change shape, but not volume. According to the numerical investigations by Zaniboni et al. (2016), the model provided reasonable results in both landslide dynamics and tsunami generation. However, it has to be mentioned that the motion path should be predefined inside the code, which implies that the complex topography effects have to be studied before using the model.

In this section, a model that include topography effects based on a global Cartesian coordinate system and solved by the FDM scheme illustrated above is used to reconstruct the historical 1783 Scilla landslide event. Additionally, the submarine landslide dynamics is studied by means of two drag laws, i.e., linear and quadratic. According to the simulations, the flow model is capable of handling topography effects and provides results that agree well with the motion mechanism described by the 1D block model (Zaniboni et al., 2016). Therefore, the flow model can be regarded as a reference to be further compared with the PFEM model that will be the subject of Chapter 3.

2.4.1 Mixture model with topography modifications

This flow model assumes that the landslide consists of a grain-water mixture. It can be simply regarded as the extension of the single-phase flow with topography effects. Usually,

the complex topography effects driving the mass flows can be treated in a curvilinear coordinate system (Gray et al., 1999), or implemented into more complicated Boussinesq-like models (e.g., Castro-Orgaz et al., 2015; Denlinger and Iverson, 2004) to ensure the accuracy and robustness of the numerical schemes. Here, we adopt the model considering vertical acceleration and curvature effects resulting from topography effects based on the global Cartesian coordinate system (Xia and Liang, 2018), and the model has been proven in both theoretical studies and applications. The vector form of this model is given as follows:

$$\begin{aligned} \vec{U} &= \begin{bmatrix} h \\ hu \\ hv \end{bmatrix}; \quad \vec{F} = \begin{bmatrix} hu \\ hu^2 + \frac{1}{2}g\phi^{-2}h^2 \\ huv \end{bmatrix}; \\ \vec{G} &= \begin{bmatrix} hv \\ huv \\ hv^2 + \frac{1}{2}g\phi^{-2}h^2 \end{bmatrix}; \quad \vec{S} = \vec{S}_b + \vec{S}_f \end{aligned} \quad (2.29)$$

$$\begin{aligned} \vec{S}_b &= \begin{bmatrix} 0 \\ -ahb_x + \frac{1}{2}gh^2 \frac{\partial(\phi^{-2})}{\partial x} \\ -ahb_y + \frac{1}{2}gh^2 \frac{\partial(\phi^{-2})}{\partial y} \end{bmatrix}; \\ \vec{S}_f &= \begin{bmatrix} 0 \\ -\frac{\mu ah u \phi}{\sqrt{u^2+v^2+(ub_x+vb_y)^2}} \\ -\frac{\mu ah v \phi}{\sqrt{u^2+v^2+(ub_x+vb_y)^2}} \end{bmatrix} \end{aligned} \quad (2.30)$$

$$\begin{aligned} a &= \phi^{-2}(g + \vec{v}^T \vec{H} \vec{v}), \quad \vec{v} = (u, v)^T; \\ \vec{H} &= \begin{bmatrix} b_{xx} & b_{xy} \\ b_{xy} & b_{yy} \end{bmatrix}; \quad \phi = (b_x^2 + b_y^2 + 1)^{1/2} \end{aligned} \quad (2.31)$$

where \vec{S}_b is the basal topography term and \vec{S}_f is the friction term. The factor ϕ^{-2} merely related to basal topography is theoretically important for the governing equations considering complex topography in a Cartesian coordinate system. The term $\vec{v}^T \vec{H} \vec{v}$ accounts for the effect of the centrifugal force. \vec{v} is the velocity vector including velocity components along x and y directions. The parameter μ is the basal friction coefficient, and $b(x, y)$ is the basal surface of the landslide. $b_{x(y)}$ and b_{xx}, b_{xy}, b_{yy} represent the first-order and the second-order derivatives. In this case we have assumed that the lateral earth pressure coefficients K_x and K_y are equal to 1.

2.4.2 Buoyancy and drag force terms

In the study conducted by Mazzanti and Bozzano (2011), using the DAN3D model, the motion of the submarine landslide is computed by applying a turbulence coefficient, which is rarely used in mass flow models. In our simulation, the whole event is restricted to the motion of the slide, and the complicated interactions between mass and water are simplified as buoyancy and drag forces acting on the mass itself. The effective gravity acceleration for the submarine motion of the slide is reduced to $(1 - \gamma)g$, where γ is the ratio between the fluid and debris densities, i.e. $\gamma = \rho_f / \rho_s$, with $\rho_f = 1000 \text{kg/m}^3$ and $\rho_s = 1700 \text{kg/m}^3$ adopted for the simulations. The drag force is the effect of a rather complicated process difficult to describe. In mass flow modelling it can be expressed as a linear or quadratic function of the relative mass-water velocity Meng and Wang (2016); Pudasaini (2012). However, the quantification of the drag force coefficient is not easy and it is usually determined by empirical formulas based on experimental data. Additionally, some proposed models (i.e. Pudasaini, 2012) involving several parameters that are hard to evaluate, are scarcely adequate for practical applications. Here, we focus on the performance of two different drag force relationships. In our model the drag force is given as an additional source term:

$$\vec{S} = \vec{S}_b + \vec{S}_f + \vec{S}_{drag};$$

$$\vec{S}_{ldrag} = \begin{bmatrix} 0 \\ -C_d h u \\ -C_d h v \end{bmatrix}; \quad \vec{S}_{qdrag} = \begin{bmatrix} 0 \\ -C_d h u \sqrt{u^2 + v^2} \\ -C_d h v \sqrt{u^2 + v^2} \end{bmatrix} \quad (2.32)$$

where C_d is the drag force coefficient that has dimensions of inverse time for linear model and dimensions of inverse length for quadratic model. The drag force term is denoted as \vec{S}_{drag} , which is implemented as linear drag forces \vec{S}_{ldrag} or quadratic drag forces \vec{S}_{qdrag} into the model. A constant drag coefficient is used in the simulations, choosing $C_d = 0.05 \text{s}^{-1}$ for linear drag and the $C_d = 0.015 \text{m}^{-1}$ for quadratic drag forces.

2.4.3 Dynamic evolution of the Scilla landslide

After the triggering, the falling mass moves over the basal topography acted by driving and resisting forces, and finally deposits at a certain distance. The triggering mechanism of the landslide is not contained in the model, and the mass is released without initial velocity. To account for the dynamic evolution of the landslide, the average velocity, calculated by the total momentum and total height, is used to capture the overall dynamic state of the landslide. At each time step, the code detects the boundary of the region that contains the mass material,

so determining the computational domain. The choice of friction coefficients depends on the back analysis, according to the observed data (Zaniboni et al., 2016) and differentiates between subaerial and submarine sliding. The notations of μ_{SA} and μ_{SM} are used to represent the basal friction coefficient for subaerial sliding and submarine sliding respectively. For the simulation adopting the linear drag model, $\mu_{SA} = 0.25$ and $\mu_{SM} = 0.05$, while $\mu_{SA} = 0.25$ and $\mu_{SM} = 0.03$ are chosen for the quadratic drag model.

The average velocity time histories shown in Figure 2.9 clearly provide two distinct dynamics obtained from two adopted different drag functions. As for the linear-law case, one may observe that the curve we obtain here is similar to the one computed by Zaniboni et al. (2016) with their 1D block model, where they used however a quadratic law for the drag. Indeed, in both cases the landslide experiences a rapid acceleration stage followed by a slightly less rapid deceleration stage. The only difference is that the velocity peak appears at slightly different times. The curve we obtain for the quadratic law model however is quite different. The acceleration phase is shorter, the peak velocity is much less (24 m/s vs. circa 32 m/s) and the deceleration phase lasts several minutes, much longer than for the linear drag case.

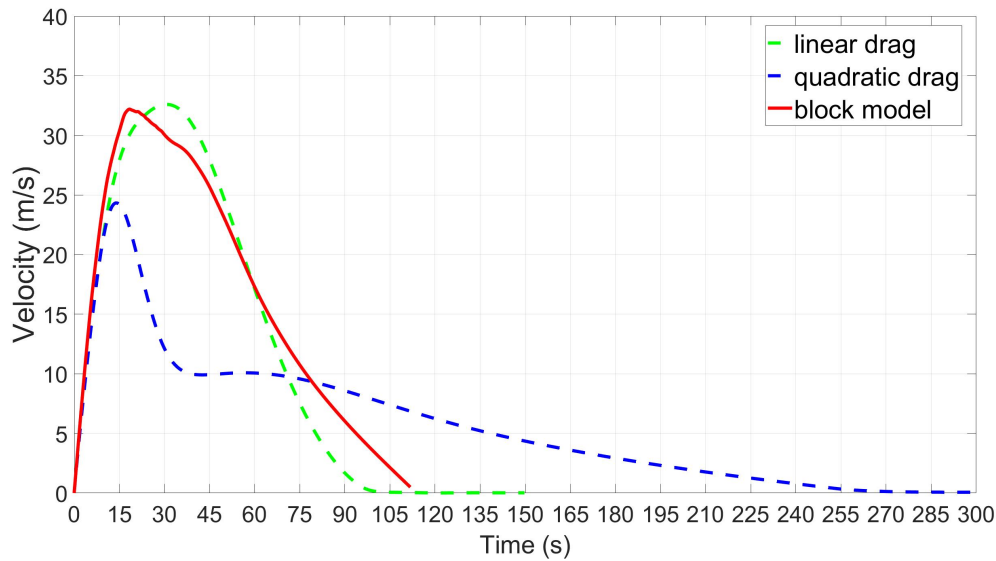


Fig. 2.9 Time evolution of the mean velocity of the landslide. The dynamics obtained from the linear drag model is quite similar to the motion depicted by the 1D quadratic-drag block model (Zaniboni et al., 2016), with slightly different accelerations. The landslide accelerates, reaching a peak value at 32 m/s and then starts slowing down. Instead, the curve from the quadratic law provides a much longer duration of the landslide motion. The landslide is strongly decelerated by the water when it crashes into the sea with high velocity and then moves slowly to the final still position. The peak velocity of the present simulations is smaller than the value exceeding 40 m/s obtained by Mazzanti and Bozzano (2011), but the deposit region is successfully reproduced by the model.

2.4.4 Propagation and Deposition

The field surveys of subaerial and submarine scars reveal the initial and final position of the landslide, while the heights of the offshore deposits are not known from the literature. We present the snapshots of the landslide height at different times in Figure 11 and Figure 12. The snapshots are shown at 10 s time intervals for the linear drag model simulation, whereas different time intervals are used for the quadratic drag model. As shown by the snapshots, the mass moves along a reasonable direction, which validates the goodness of the mixture-flow model with topographical modifications (Xia and Liang, 2018).

Figure 2.10 is the set of snapshots regarding the linear drag model. After the landslide front crashes into water, the rest of the mass enters the sea and is affected by a relatively low resistance that does not heavily impede the motion of the landslide. This dynamic is depicted by the behaviour of the front body. In the first 30 s, the main body concentrates on the middle and the rear of the landslide. Later, mainly as the effect of the drag force, the main mass moves to the front and the middle, as can be seen in the snapshot at $t = 40$ s.

During the deceleration stage, most mass deposits within the observed region (delimited by the dashed red line, see the $t = 70$ s snapshot), and the motion is practically over after 90 s. The observed landslide subaerial scar area is bounded by a solid blue line, and the observed landslide deposit area is bounded by a dashed red line. The coastline is denoted by the black line. The movement can be separated into two stages: the acceleration stage ($t = 0 - 30$ s) and the following deceleration stage. Easting and Northing are implemented as x and y directions in the simulation.

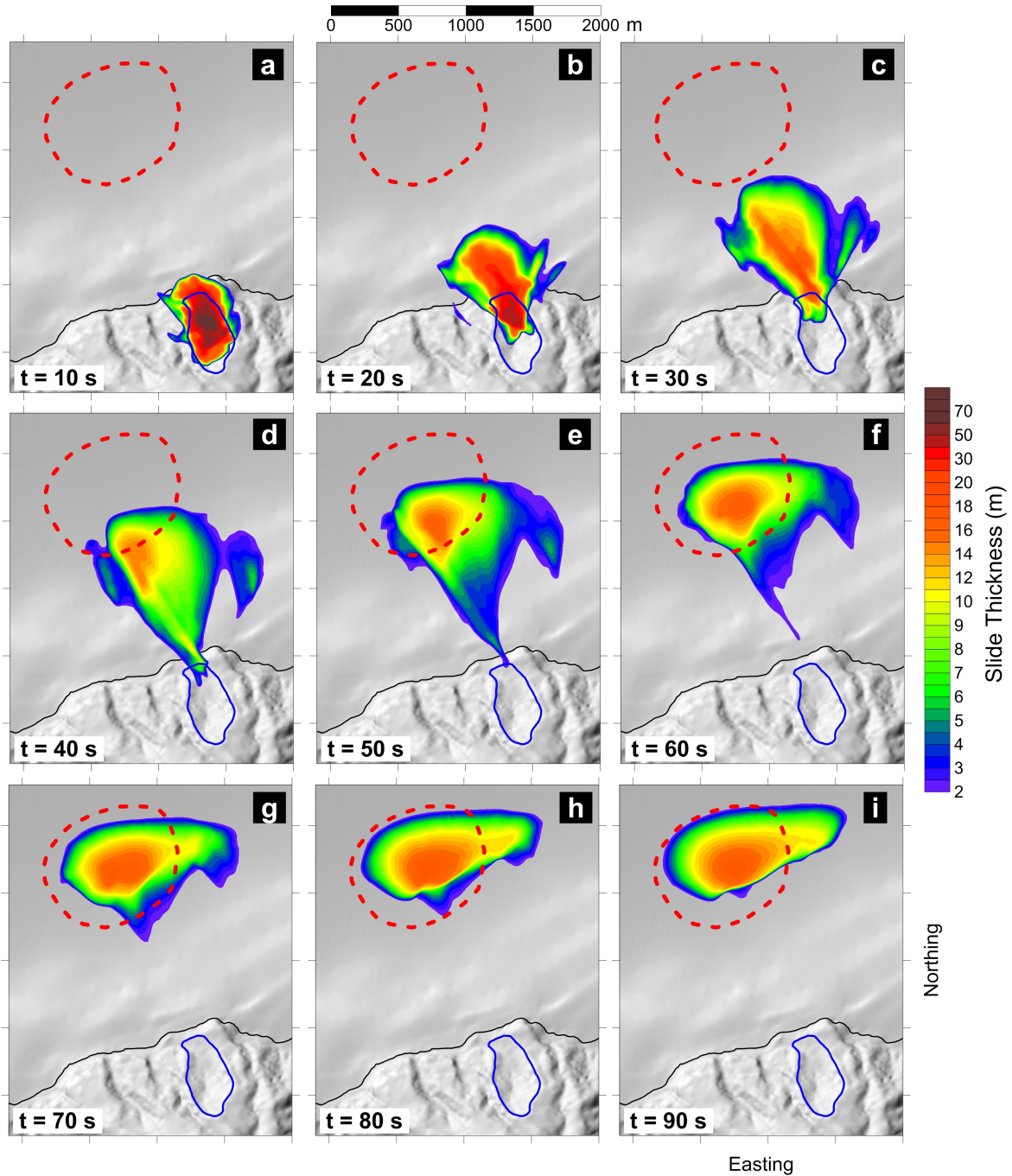


Fig. 2.10 Snapshots of the landslide mass taken at 10 s intervals (from $t = 10$ s to $t = 90$ s) obtained through the linear drag model.

Figure 2.11 displays the simulations concerning the quadratic drag case. Impacted by a very large drag when the mass front crashes into water, the landslide moves slowly and tightly during the underwater propagation. In contrast to what is shown in Figure 2.10, the main mass concentrates on the front and the middle of the body during the acceleration stage. The lateral spreading behaviour shown in Figure 2.10 is restricted in Figure 2.11. After 160 s, the main body arrives at the observed deposit region and then slowly decelerates until it stops. Note that the deposit shapes resulting from the two laws are similar, though reached at quite different times (see the $t = 90$ s image of Figure 2.10). The blue line depicts the boundary of the initial region of the landslide. The observed landslide deposit is bounded by a dashed red line with the black line denoting the coastline. The movement can be separated into three stages: an acceleration stage and two deceleration phases. The mass is mainly driven by gravity forces in the first 15 s and then experiences a strong deceleration until 30 s and then a gradual slow down until the rest. Easting and Northing are implemented as x and y directions in the simulation.

We observe that the deposits from our simulations are located inside the region defined by the observed data and therefore we can state that both kinds of simulations successfully reconstruct the landslide event from the run-out perspective. The main difference between the two simulations is that the landslide moves more slowly and remains more concentrated at least during most of the motion when the quadratic drag model is implemented, while a linear drag accounts for a larger spreading.

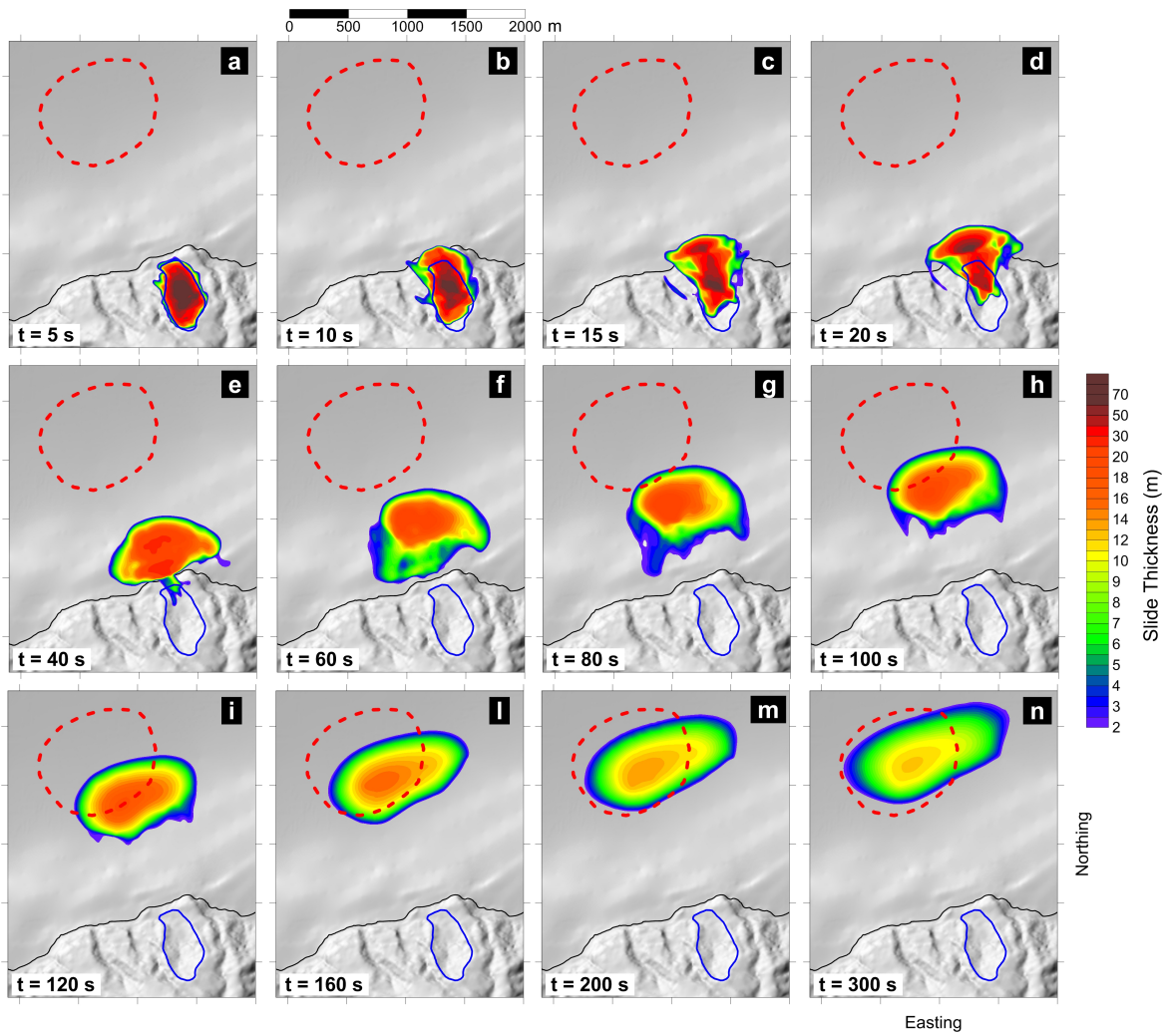


Fig. 2.11 Snapshots of the landslide mass (from $t = 10$ s to $t = 300$ s) obtained through the quadratic drag model.

Chapter 3

Particle finite element model

The finite element method (FEM) with its flexibility of considering complex geometries, various constitutive models of geomaterials, different loading conditions and providing the time evolution information of the slope body, has been seen as a dominant approach for slope stability analysis. Despite the advantages of the traditional Lagrangian FEM in slope stability analysis, it cannot capture adequately both the motion and deposition stages since severe mesh distortion is unavoidable when the sliding body suffers large deformation. To tackle this problem, the particle finite-element method (PFEM) was proposed by Idelsohn et al. (2004) that combines the standard finite-element analysis and a particle-based approach. The method was first developed for considering fluid-solid interaction (FSI) problems with free surfaces and has been further applied to the modelling of landslides (Cremonesi et al., 2011; Oñate et al., 2011; Zhang et al., 2015).

The existing PFEM for landslide modelling can be classified into two categories based on the FEM solvers: (1) Newton-Raphson method (Cremonesi et al., 2011; Oñate et al., 2011); (2) Mathematical-programming. The Newton-Raphson iteration method is the most used scheme for the implementation of FEM in many codes and the iterations are carried out between the level of global structures (where the unbalanced force is minimized) and the level of material points such as stress integration points (where the stress-strain relationship should be fulfilled). Loading steps are conducted through a series of load increments in a relatively small magnitude for the sake of convergence (Bathe, 2006). As for the mathematical programming method, the boundary value problems (BVP) are converted into equivalent optimization problem, which can be solved using the interior point method (IPM). Based on the analysis of the existence, uniqueness, sensitivity and stability of the solution can be carried out mathematically, and efforts have been devoted to analyse the convergence properties of this method (Alizadeh et al., 1998; Tits et al., 2003). The non-linear partial differential

equations are cast as second-order cone programming (SOCP) problem, abbreviated as SOCP-FEM and its PFEM version is denoted as SOCP-PFEM.

Even though the theory of the SOCP-PFEM has been well documented in Zhang et al. (2013), its numerical implementation, which is widely different from the PFEM version based on Newton's iteration schemes, was not introduced in detail, which therefore handicaps its further applications. We remark that the solution scheme for the finite element formulation in the optimization-based PFEM differs considerably from that in the version developed by Oñate et al. (2004) and by Cremonesi et al. (2010). This section is to explain the developed mathematical optimization-based PFEM model based on the work by Zhang et al. (2013) and some parts of this section have been published in Wang et al. (2019b).¹

3.1 Governing equations

The governing equations are partial differential equations of rate-independent elastoplastic plane-strain problems for a continuum medium. First the system of equations for a static analysis is established, and then dynamic and contact analysis problems are covered. These equations include the equilibrium equations, the geometric equations, the constitutive equations and the boundary conditions. Further, the θ time-integration method (Bathe and Wilson, 1972) and the rigid contact scheme are introduced to account for the dynamic and the contact analysis.

3.1.1 Static analysis

For a 2D domain V delimited by a boundary S , the set of equations relevant for a static analysis is as follows.

(a) The equilibrium equation

$$\nabla^T \boldsymbol{\sigma} + \mathbf{b} = \mathbf{0} \quad (3.1)$$

where the operator is $\nabla^T = (\frac{\partial}{\partial x}, 0, \frac{\partial}{\partial y}, 0, \frac{\partial}{\partial y}, \frac{\partial}{\partial x})$, the body force is $\mathbf{b} = (b_x, b_y)^T$ and the stress is $\boldsymbol{\sigma} = (\sigma_{xx}, \sigma_{yy}, \sigma_{zz}, \sigma_{xy})^T$.

(b) The strain-displacement relationship

$$\boldsymbol{\varepsilon} = \nabla \mathbf{u} \quad (3.2)$$

¹Most contents in this section have been summarized in a paper published in: Wang, L., Zhang, X., Zaniboni, F., Oñate, E., & Tinti, S. (2019). Mathematical optimization problems for particle finite element analysis applied to 2D landslide modeling[J]. *Mathematical Geosciences*, 1-23.

where the strain is $\boldsymbol{\varepsilon} = (\boldsymbol{\varepsilon}_{xx}, \boldsymbol{\varepsilon}_{yy}, 2\boldsymbol{\varepsilon}_{xy})^T$ and the displacement is $\mathbf{u} = (u_x, u_y)^T$.

(c) The boundary conditions on S

$$\mathbf{N}\boldsymbol{\sigma} = \mathbf{t} \quad (3.3a)$$

$$\mathbf{u} = \mathbf{u}^p \quad (3.3b)$$

where $\mathbf{N} = (n_x, 0, n_y; 0, n_y, n_x)$, \mathbf{t} is the traction force and \mathbf{u}^p is the prescribed displacement.

(d) The constitutive relationship

$$F(\boldsymbol{\sigma}) \leq 0 \quad (3.4a)$$

$$\boldsymbol{\varepsilon} = \boldsymbol{\varepsilon}^e + \boldsymbol{\varepsilon}^p \quad \boldsymbol{\varepsilon}^e = \mathbb{C}\boldsymbol{\sigma} \quad \boldsymbol{\varepsilon}^p = \lambda \nabla_{\boldsymbol{\sigma}} G(\boldsymbol{\sigma}) \quad (3.4b)$$

in which F is the yield function, $\boldsymbol{\varepsilon}^e$ and $\boldsymbol{\varepsilon}^p$ are the elastic and the plastic strains, \mathbb{C} is the elastic compliance matrix, λ is the plastic multiplier and G is the plastic potential. As shown in (3.4b), the additive decomposition of the strain is used, whose incremental form is:

$$\Delta\boldsymbol{\varepsilon} = \mathbb{C}\Delta\boldsymbol{\sigma} + \Delta\lambda \nabla_{\boldsymbol{\sigma}} G(\boldsymbol{\sigma}) \quad (3.5)$$

For an associated flow rule, we have $G = F$. When the material undergoes purely elastic deformation, the plastic multiplier increment $\Delta\lambda = 0$ and $F(\boldsymbol{\sigma}) < 0$, whereas, when the material yields, we have $\Delta\lambda > 0$ and $F(\boldsymbol{\sigma}) = 0$. This constrain is the so-called complementary condition that

$$\Delta\lambda F(\boldsymbol{\sigma}) = 0, \quad \Delta\lambda \geq 0 \quad (3.6)$$

Therefore, the above constitutive relationships are summarized in the following expression:

$$\left\{ \begin{array}{l} F(\boldsymbol{\sigma}) \leq 0 \\ \Delta\boldsymbol{\varepsilon} = \mathbb{C}\Delta\boldsymbol{\sigma} + \Delta\lambda \nabla_{\boldsymbol{\sigma}} G(\boldsymbol{\sigma}) \\ \Delta\lambda F(\boldsymbol{\sigma}) = 0, \quad \Delta\lambda \geq 0 \end{array} \right. \quad (3.7)$$

3.1.2 Dynamic analysis

For dynamic analyses, the inertial force should be included in the equilibrium equation (3.1) that is:

$$\nabla^T \boldsymbol{\sigma} + \mathbf{b} = \rho \dot{\mathbf{v}} \quad (3.8a)$$

$$\mathbf{v} = \dot{\mathbf{u}} \quad (3.8b)$$

By means of the θ -method (Bathe and Wilson, 1972), the expressions of stresses and velocities become $\boldsymbol{\sigma} = \theta_1 \boldsymbol{\sigma}_{n+1} + (1 - \theta_1) \boldsymbol{\sigma}_n$ and $\mathbf{v} = \theta_2 \mathbf{v}_{n+1} + (1 - \theta_2) \mathbf{v}_n$, rendering Eq. (3.8) as:

$$\nabla^T [\theta_1 \boldsymbol{\sigma}_{n+1} + (1 - \theta_1) \boldsymbol{\sigma}_n] + \mathbf{b} = \rho \frac{\mathbf{v}_{n+1} - \mathbf{v}_n}{\Delta t} \quad (3.9a)$$

$$\theta_2 \mathbf{v}_{n+1} + (1 - \theta_2) \mathbf{v}_n = \frac{\mathbf{u}_{n+1} - \mathbf{u}_n}{\Delta t} \quad (3.9b)$$

Hereafter, the subscripts n and $n + 1$ denote the known and unknown states at times t_n and $t_n + \Delta t$ respectively, and Δt is the time step. By introducing a new intermediate variable, i.e. the inertial force γ , whose definition is shown in (3.12), and substituting Eq. (3.9b) into Eq. (3.9a), the latter can be rearranged as:

$$\nabla^T \boldsymbol{\sigma}_{n+1} + \frac{1 - \theta_1}{\theta_1} \nabla^T \boldsymbol{\sigma}_n + \tilde{\mathbf{b}} = \gamma_{n+1} \quad (3.10)$$

and the according traction boundary condition Eq. (3.3a) becomes

$$\mathbf{N} \boldsymbol{\sigma}_{n+1} = \tilde{\mathbf{t}} \quad (3.11)$$

in which

$$\tilde{\rho} = \frac{\rho}{\theta_1 \theta_2}, \quad \tilde{\mathbf{b}} = \frac{1}{\theta_1} \mathbf{b} + \tilde{\rho}, \quad \gamma_{n+1} = \tilde{\rho} \frac{\Delta \mathbf{u}}{\Delta t^2}, \quad \tilde{\mathbf{t}} = \frac{1}{\theta_1} \mathbf{t} \quad (3.12)$$

Eq. (3.9b) can also be rearranged as

$$\mathbf{v}_{n+1} = \frac{1}{\theta_2} \left[\frac{\Delta \mathbf{u}}{\Delta t} - (1 - \theta_2) \mathbf{v}_n \right] \quad (3.13)$$

which is used to update velocity \mathbf{v}_{n+1} after the displacement increment $\Delta \mathbf{u}$ is obtained. It should be mentioned that the time integration scheme is unconditional stable when $\theta_1 \geq \frac{1}{2}$ and $\theta_2 \geq \frac{1}{2}$.

3.1.3 Contact analysis

The implementation of a rigid non-penetration contact scheme ensures that the incremental nodal displacements do not exceed the gap between the node and the boundary. Therefore, the contact condition is derived as follows:

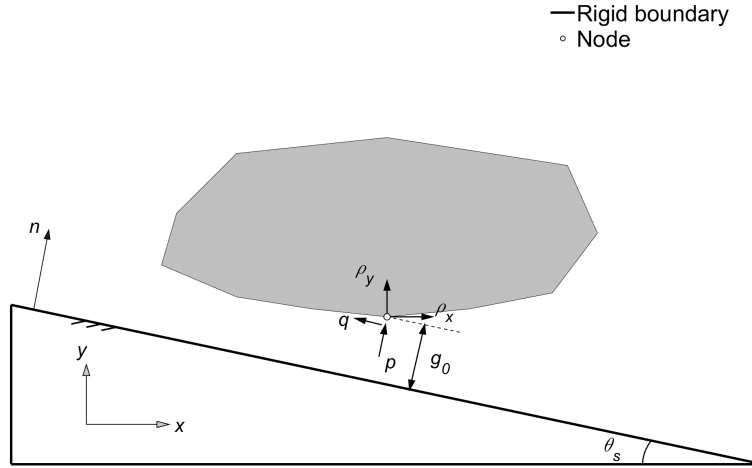


Fig. 3.1 Schematic of contact condition.

$$\mathbf{n}^T \Delta \mathbf{u} - g_0 \leq 0 \quad (3.14a)$$

$$p(\mathbf{n}^T \Delta \mathbf{u} - g_0) = 0 \quad (3.14b)$$

$$|q| - \mu p \leq 0 \quad (3.14c)$$

where \mathbf{n} is the outward unit vector of the rigid surface, g_0 is the gap between the boundary point of deformable materials and the rigid surface at $t = t_n$, p is the normal force, q is the tangential force and μ is the friction coefficient.

3.2 Min-max program for finite-element analysis

The aforementioned governing equations can be reformulated as min-max formulations according to previous works (e.g., Krabbenhoft et al., 2007; Simo et al., 1989; Simo and Taylor, 1985; Zhang et al., 2013), where detailed derivations have been documented. In the section, a brief summary is provided for those equivalent min-max optimization problems.

The standard finite-element analysis follows from the principle of minimum potential energy or from the principle of virtual work, considering displacements or stresses as the only master field while all other field variables can be obtained by the master field. The multi-field Hellinger-Reissner variational principle (Reissner, 1950), treating displacements and stresses as the master fields is adopted for static analysis after defining the functional:

$$\Pi(\boldsymbol{\sigma}, \mathbf{u}) = \int_V \left(-\frac{1}{2} \Delta \boldsymbol{\sigma}^T \mathbb{C} \Delta \boldsymbol{\sigma} + \boldsymbol{\sigma}^T \nabla^T \mathbf{u} \right) dV - \int_V \mathbf{b}^T \mathbf{u} dV - \int_S \mathbf{t}^T \mathbf{u} dS \quad (3.15)$$

The equivalence between this variational principle and the governing equations can be proved by introducing an additional equation with a new variable s :

$$F(\boldsymbol{\sigma}_{n+1}) + s = 0, \quad s > 0 \quad (3.16)$$

Next, the following functional is defined:

$$J = \Pi(\boldsymbol{\sigma}, \mathbf{u}) + \beta \ln s - \Delta \lambda (F(\boldsymbol{\sigma}_{n+1}) + s) \quad (3.17)$$

where β is an arbitrarily small constant and the logarithmic barrier function implies the fact that $s > 0$. Taking functional derivatives, the governing equations of static analysis in section 3.1 can be obtained as follows:

$$\frac{\delta J}{\delta \Delta \mathbf{u}} = \begin{cases} \nabla^T \boldsymbol{\sigma} + \mathbf{b} = \mathbf{0}, & \text{in } V \\ \mathbf{N} \boldsymbol{\sigma} = \mathbf{t}, & \text{on } S \end{cases} \quad (3.18a)$$

$$\frac{\delta J}{\delta \boldsymbol{\sigma}} = \nabla(\Delta \mathbf{u}) - \mathbb{C} \Delta \boldsymbol{\sigma} - \Delta \lambda \Delta F(\boldsymbol{\sigma}) = 0 \quad (3.18b)$$

$$\frac{\delta J}{\delta \Delta \lambda} = F(\boldsymbol{\sigma}) + s = 0 \quad (3.18c)$$

$$\frac{\delta J}{\delta s} \rightarrow s \Delta \lambda = \beta \quad (3.18d)$$

These equations are equivalent to the governing equations for static analysis when β approaches to 0. It should be mentioned that the flow rule for material behaviour $F = G$ is included in Eq. (3.18b). Therefore, the solutions can be obtained at the saddle point of the functional Eq. (3.15), expressed as $\delta \Pi(\boldsymbol{\sigma}, \mathbf{u}) = 0$. According to this formulation, the problem is transformed easily to a problem of min-max optimization, more specifically to:

$$\min_{\mathbf{u}} \max_{\boldsymbol{\sigma}} \int_V \left(-\frac{1}{2} \Delta \boldsymbol{\sigma}^T \mathbb{C} \Delta \boldsymbol{\sigma} + \boldsymbol{\sigma}^T \nabla^T \mathbf{u} \right) dV - \int_V \mathbf{b}^T \mathbf{u} dV - \int_S \mathbf{t}^T \mathbf{u} dS \quad (3.19)$$

where, the internal work is maximized with respect to stresses and the total potential energy is minimized with respect to displacements. The incremental form of the min-max problem is implemented for conducting the analysis.

$$\begin{aligned} \min_{\Delta \mathbf{u}} \max_{\sigma_{n+1}} & -\frac{1}{2} \int_V \Delta \boldsymbol{\sigma}^T \mathbb{C} \Delta \boldsymbol{\sigma} dV + \int_V \boldsymbol{\sigma}^T \nabla^T \Delta \mathbf{u} dV - \int_V \mathbf{b}^T \Delta \mathbf{u} dV - \int_S \tilde{\mathbf{t}}^T \Delta \mathbf{u} dS \quad (3.20) \\ \text{subject} & F(\boldsymbol{\sigma}) \leq 0 \end{aligned}$$

Here, the stress increment $\Delta \boldsymbol{\sigma}$ is estimated by $\Delta \boldsymbol{\sigma} = \boldsymbol{\sigma}_{n+1} - \boldsymbol{\sigma}_n$ and $\Delta \mathbf{u}$ denotes the displacement at the current analysis step. Efforts have also been devoted to reformulate the governing equations for dynamic elastoplastic problems. It was demonstrated (Zhang et al., 2013) that the min-max optimization problem equivalent to the governing equations discretized by θ -method for dynamic analysis is:

$$\begin{aligned} \min_{\Delta \mathbf{u}} \max_{(\boldsymbol{\sigma}, \boldsymbol{\gamma})_{n+1}} & -\frac{1}{2} \int_V \Delta \boldsymbol{\sigma}^T \mathbb{C} \Delta \boldsymbol{\sigma} dV + \int_V \boldsymbol{\sigma}_{n+1}^T \nabla^T \Delta \mathbf{u} dV - \int_V \tilde{\mathbf{b}}^T \Delta \mathbf{u} dV \quad (3.21) \\ & - \int_S \tilde{\mathbf{t}}^T \Delta \mathbf{u} dS + \frac{(1-\theta_1)}{\theta_1} \int_V \boldsymbol{\sigma}_n^T \nabla^T \Delta \mathbf{u} dV + \int_V \boldsymbol{\gamma}_{n+1}^T \Delta \mathbf{u} dV - \frac{\Delta t^2}{2} \int_V \boldsymbol{\gamma}_{n+1}^T \tilde{\rho}^{-1} \boldsymbol{\gamma}_{n+1} dV \\ \text{subject} & F(\boldsymbol{\sigma}_{n+1}) \leq 0 \end{aligned}$$

where the inertial force $\boldsymbol{\gamma}$ is included as an independent master field in the maximum part of the optimization problem. The contact constraints will be taken into account later.

3.3 Finite-element discretization

3.3.1 Mixed triangular element

The finite-element approximations are achieved by the use of shape functions. Following the standard finite-element notation, the relationship between element and nodes can be written as:

$$\boldsymbol{\sigma} \approx \mathbf{N}_\sigma \hat{\boldsymbol{\sigma}} \quad (3.22a)$$

$$\mathbf{u} \approx \mathbf{N}_u \hat{\mathbf{u}} \quad (3.22b)$$

$$\boldsymbol{\gamma} \approx \mathbf{N}_\gamma \hat{\boldsymbol{\gamma}} \quad (3.22c)$$

where $\hat{\boldsymbol{\sigma}}$, $\hat{\mathbf{u}}$ and $\hat{\boldsymbol{\gamma}}$ are stresses, displacements and dynamic forces at nodes, while \mathbf{N}_σ , \mathbf{N}_u and \mathbf{N}_γ are the corresponding matrix forms of the shape functions. The mixed isoparametric triangle element (Bathe, 2006) is chosen for our simulations, using quadratic shape functions

for displacements interpolation and linear shape functions for stresses interpolation. Within an element, six nodes at the edges are used to discretize displacements and dynamic forces, while three integration nodes are used to discretize stresses, as illustrated in Fig. 3.2.

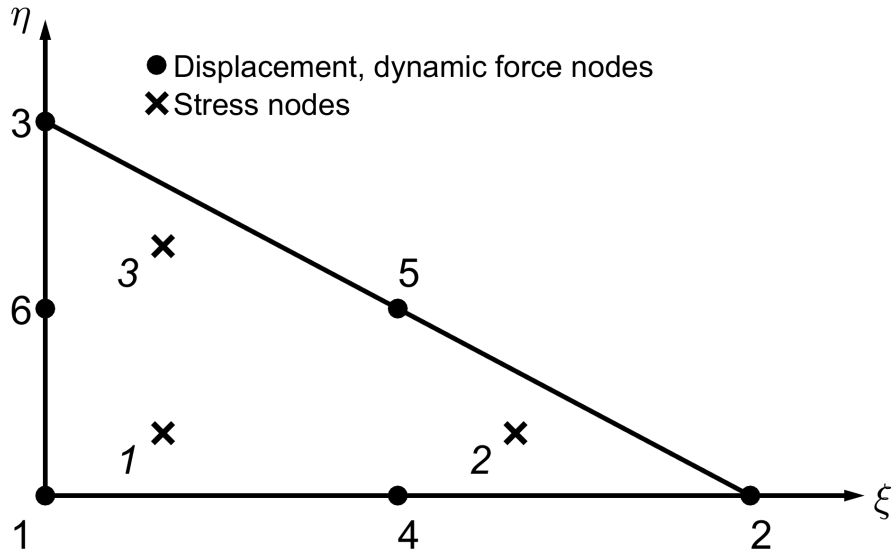


Fig. 3.2 Quadratic/linear isotropic triangular element utilized in the simulation.

By substituting the Eq. (3.29b) into the geometric Eq. (3.2), the relationship between strains and nodal displacements is

$$\boldsymbol{\varepsilon} = \nabla^T \mathbf{u} = \mathbf{B}_u \hat{\mathbf{u}} \quad (3.23)$$

where, \mathbf{B}_u are the partial derivatives of the displacement shape functions with respect to the global coordinates x and y . The shape functions N_u and N_σ are:

$$N_u^1 = (2\zeta - 1)\zeta, N_u^2 = (2\xi - 1)\xi, N_u^3 = (2\eta - 1)\eta, N_u^4 = 4\xi\zeta, N_u^5 = 4\xi\eta, N_u^6 = 4\eta\zeta; \quad (3.24a)$$

$$N_\sigma^1 = 2\zeta - \frac{1}{3}, N_\sigma^2 = 2\xi - \frac{1}{3}, N_\sigma^3 = 2\eta - \frac{1}{3}. \quad (3.24b)$$

in which, ξ, η, ζ are the local coordinates and $\zeta = 1 - \xi - \eta$. Consequently, the local derivatives of N_u are:

$$\frac{\partial N_u^1}{\partial \xi} = 4(\xi + \eta) - 3, \frac{\partial N_u^2}{\partial \xi} = 4\xi - 1, \frac{\partial N_u^3}{\partial \xi} = 0, \frac{\partial N_u^4}{\partial \xi} = 4 - 8\xi - 4\eta, \frac{\partial N_u^5}{\partial \xi} = 4\eta, \frac{\partial N_u^6}{\partial \xi} = -4\eta. \quad (3.25a)$$

$$\frac{\partial N_u^1}{\partial \eta} = 4(\xi + \eta) - 3, \frac{\partial N_u^2}{\partial \eta} = 0, \frac{\partial N_u^3}{\partial \eta} = 4\eta - 1, \frac{\partial N_u^4}{\partial \eta} = -4\xi, \frac{\partial N_u^5}{\partial \eta} = 4\xi, \frac{\partial N_u^6}{\partial \eta} = 4 - 8\eta - 4\xi. \quad (3.25b)$$

As for the numerical integration, the Gauss integration scheme is adopted to calculate the numerical integrations over the triangular elements:

$$\int_V x d\eta d\xi = \frac{1}{2} \sum w_i x(\eta_i, \xi_i) \quad (3.26)$$

where, x is the integral variable, V denotes the integration domain and w_i are the weight factors. A seven-point integration scheme is recommended for the integration of the variable involving the calculation of a matrix square root, such as the calculation of $\mathbf{C}^{1/2}$ in the next section, since in such a case a three-point integration is not able to ensure the required accuracy. For different finite elements, the local coordinates and weight factors of the integration points are documented in Bathe (2006).

3.3.2 Finite element discretization

Using the explained finite element discretization, the discrete form of the min-max problem (3.21) for dynamic analysis can be expressed as:

$$\min_{\Delta \hat{\mathbf{u}}} \max_{(\hat{\boldsymbol{\sigma}}, \hat{\boldsymbol{\gamma}})_{n+1}} \hat{\boldsymbol{\sigma}}_{n+1}^T \mathbf{B} \Delta \hat{\mathbf{u}} - \tilde{\mathbf{f}}^T \Delta \hat{\mathbf{u}} - \frac{1}{2} \Delta \hat{\boldsymbol{\sigma}}_{n+1}^T \mathbf{C} \Delta \hat{\boldsymbol{\sigma}}_{n+1} - \frac{1}{2} \Delta t^2 \hat{\boldsymbol{\gamma}}_{n+1}^T \mathbf{D} \hat{\boldsymbol{\gamma}}_{n+1} + \hat{\boldsymbol{\gamma}}_{n+1}^T \mathbf{A} \Delta \hat{\mathbf{u}} \quad (3.27a)$$

$$\text{subject to } F(\hat{\boldsymbol{\sigma}}_{n+1}^j) \leq 0, \quad j = 1, \dots, n_\sigma \quad (3.27b)$$

Where

$$\tilde{\mathbf{f}} = \int_V \mathbf{N}_u^T \tilde{\mathbf{b}} dV + \int_S \mathbf{N}_u^T \tilde{\mathbf{t}} dS - \frac{1 - \theta_1}{\theta_1} \mathbf{B}^T \hat{\boldsymbol{\sigma}}_n \quad (3.28a)$$

$$\mathbf{B} = \int_V \mathbf{N}_\sigma^T \mathbf{B}_u dV \quad (3.28b)$$

$$\mathbf{C} = \int_V \mathbf{N}_\sigma^T \mathbf{C} \mathbf{N}_\sigma dV \quad (3.28c)$$

$$\mathbf{D} = \int_V \mathbf{N}_\gamma^T \tilde{\rho}^{-1} \mathbf{N}_\gamma dV \quad (3.28d)$$

$$\mathbf{A} = \int_V \mathbf{N}_u^T \mathbf{N}_\gamma dV \quad (3.28e)$$

$$(3.28f)$$

In the optimization problem (3.27), the yield function (3.27b) is imposed at the stress interpolation points, with n_σ and $\hat{\boldsymbol{\sigma}}_{n+1}^j$ being respectively the total number of the stress interpolation points and the stress states at the j th stress integration point at t_{n+1} . The minimization part of the min-max problem (3.27a) can be resolved analytically meaning that the min-max problem (3.27) is equivalent to the following maximization problem:

$$\max_{(\hat{\boldsymbol{\sigma}}, \hat{\boldsymbol{\gamma}})_{n+1}} -\frac{1}{2} \Delta \hat{\boldsymbol{\sigma}}_{n+1}^T \mathbf{C} \Delta \hat{\boldsymbol{\sigma}}_{n+1} - \frac{1}{2} \Delta t^2 \hat{\boldsymbol{\gamma}}_{n+1}^T \mathbf{D} \hat{\boldsymbol{\gamma}}_{n+1} \quad (3.29a)$$

$$\text{subject to } F(\hat{\boldsymbol{\sigma}}_{n+1}^j) \leq 0, \quad j = 1, \dots, n_\sigma \quad (3.29b)$$

$$\mathbf{B}^T \hat{\boldsymbol{\sigma}}_{n+1} - \tilde{\mathbf{f}} + \mathbf{A}^T \hat{\boldsymbol{\gamma}}_{n+1} = \mathbf{0} \quad (3.29c)$$

which is the one for dynamic analysis.

The optimization problem (3.29) can be reduced to the one for quasi-static elastoplastic analysis by removing the terms relevant to dynamics and setting $\theta_1 = \theta_2 = 1$. Specifically, for quasi-static elastoplastic analysis is:

$$\min_{\Delta \hat{\mathbf{u}}} \max_{\hat{\boldsymbol{\sigma}}_{n+1}} -\frac{1}{2} \Delta \hat{\boldsymbol{\sigma}}_{n+1}^T \mathbf{C} \Delta \hat{\boldsymbol{\sigma}}_{n+1} \quad (3.30a)$$

$$\text{subject to } F(\hat{\boldsymbol{\sigma}}_{n+1}^j) \leq 0, \quad j = 1, \dots, n_\sigma \quad (3.30b)$$

$$\mathbf{B}^T \hat{\boldsymbol{\sigma}}_{n+1} - \mathbf{f} = \mathbf{0} \quad (3.30c)$$

in which $\mathbf{f} = \int_V \mathbf{N}_u^T \mathbf{b} dV + \int_S \mathbf{N}_u^T \mathbf{t} dS$.

In contact analysis problems, at every time step, the identification of potential contact nodes should be carried out and the normal and tangential forces are implemented at these nodes. The displacements of the potential contact nodes cannot be higher than the distance

from the boundary, considering the non-penetration contact condition. The potential nodes are identified as contact nodes, if the normal displacements of the contact nodes equal the gap, $\Delta \mathbf{u}_N - g_0 = 0$. If not, $\Delta \mathbf{u}_N \leq g_0$. And the variational formulation of this contact scheme is the same (with the same contact inequality), used in granular dynamics by Krabbenhoft et al. (2012b).

$$\max \quad -g_0 p \quad (3.31a)$$

$$\text{subject to} \quad |q| - \mu p \leq 0, p \geq 0 \quad (3.31b)$$

The contact analysis is included only when the dynamic analysis is conducted. So the min-max problem is rewritten as

$$\max_{(\hat{\sigma}, \hat{\gamma}, p_j)_{n+1}} \quad -\frac{1}{2} \Delta \hat{\sigma}_{n+1}^T \mathbf{C} \Delta \hat{\sigma}_{n+1} - \frac{1}{2} \Delta t^2 \hat{\gamma}_{n+1}^T \mathbf{D} \hat{\gamma}_{n+1} - \sum_{j=1}^{n_c} g_{0j} p_j \quad (3.32a)$$

$$\text{subject to} \quad F(\hat{\sigma}_{n+1}^j) \leq 0, \quad j = 1, \dots, n_\sigma \quad (3.32b)$$

$$\mathbf{B}^T \hat{\sigma}_{n+1} + \mathbf{A}^T \hat{\gamma}_{n+1} + \mathbf{E}_c^T \boldsymbol{\rho} = \tilde{\mathbf{f}} \quad (3.32c)$$

$$p_j = -\mathbf{n}_j^T \boldsymbol{\rho}_j, \quad j = 1, \dots, n_c \quad (3.32d)$$

$$q_j = -\hat{\mathbf{n}}_j^T \boldsymbol{\rho}_j, \quad j = 1, \dots, n_c \quad (3.32e)$$

$$|q_j| - \mu p_j \leq 0, \quad j = 1, \dots, n_c \quad (3.32f)$$

in which, $\boldsymbol{\rho} = (\rho_x, \rho_y)^T$ is the nodal forces vector, $\mathbf{n} = (n_x, n_y)^T$ is the normal of the rigid boundary and $\hat{\mathbf{n}} = (-n_y, n_x)^T$. Assuming that the inclined angle of the slope is θ_s (see Figure 3.1), the corresponding components are $n_x = \sin \theta_s, n_y = \cos \theta_s$. The logical index set of contact nodes is denoted as \mathbf{E}_c and n_c is the number of potential contact nodes. The potential contact nodes are set as the nodes on the surface S of the computational domain V . The present maximization problem is a type of a convex optimization problem that can be recast as a standard second-order cone programming (SOCP) problem and then resolved using the interior point method. For simplicity, the present scheme for the finite element solution is abbreviated as SOCP-FEM.

3.4 Numerical implementation

Although the theories of the SOCP-FEM analysis for quasi-static and dynamic elastoplastic problems have been well demonstrated, there are only few efforts devoted to its numerical implementation. This section focuses primarily on the numerical implementation of the SOCP-FEM with emphasis on some key aspects. Particularly, we focus on (1) the implemen-

tation of the boundary conditions in the SOCP-FEM; (2) the transformation of the resulting maximization problem for quasi-static/dynamic elastoplastic analyses into a standard SOCP problem; and (3) the solution of the resulting SOCP problem using the IPM available in MOSEK. MOSEK is a large-scale optimization software, and it is freely available for academic license. For the present simulations, the MOSEK optimization toolbox for MATLAB is used and more details can be found in MOSEK (2019).

3.4.1 Implementation of boundary conditions

The traction and displacement boundary conditions have to be imposed so that the boundary-value problem can be resolved. The traction boundary condition, for instance Eq. (3.3a), is handled by integrating tractions along the boundary surface, resulting in equivalent nodal forces. In other words, the implementation of the traction boundary condition in the SOCP-FEM is exactly the same as that in the traditional displacement-based FEM (Bathe, 2006). Nevertheless, the imposition of displacement boundary condition (3.3b) in the SOCP-FEM differs from that in the displacement-based FEM. In the traditional displacement-based FEM, the displacement boundary condition is implemented either by the penalty method or by modifying the global stiffness matrix. In contrast, the SOCP-FEM requires the introduction of a new field variable, i.e. the nodal reaction force $\hat{\mathbf{r}}_{n+1}$, for this purpose. Specifically, for quasi-static problems, the discretized optimization problem with displacement boundary conditions being fulfilled is in the form of

$$\max_{(\hat{\boldsymbol{\sigma}}, \hat{\mathbf{r}})_{n+1}} -\frac{1}{2} \Delta \hat{\boldsymbol{\sigma}}_{n+1}^T \mathbf{C} \Delta \hat{\boldsymbol{\sigma}}_{n+1} + (\mathbf{E}_u \mathbf{u}^p)^T \hat{\mathbf{r}}_{n+1} \quad (3.33a)$$

$$\text{subject to } F(\hat{\boldsymbol{\sigma}}_{n+1}^j) \leq 0, \quad j = 1, \dots, n_\sigma \quad (3.33b)$$

$$\mathbf{B}^T \hat{\boldsymbol{\sigma}}_{n+1} - \mathbf{f} = \mathbf{E}_u \hat{\mathbf{r}}_{n+1} \quad (3.33c)$$

In contrast to the min-max program for static analysis shown in (3.30a-c), the new equations consider the work done by the nodal reaction force $\hat{\mathbf{r}}_{n+1}$ and the change on equilibrium equation (3.33c). This equilibrium condition can also be implemented into the dynamic and the contact analyses. It is worth noting that $\boldsymbol{\sigma}_{n+1}$ and $\Delta \mathbf{u}$ are dual variables, that can be obtained simultaneously by the optimization solver. Consequently, the imposition of the stress boundary condition and of the displacement boundary condition cannot be imposed on the same element, namely over-constraints are not allowed. To check the validity, the

Lagrangian associated with (3.3) is constructed:

$$\mathcal{L} = \frac{1}{2} \Delta \hat{\boldsymbol{\sigma}}^T \mathbf{C} \Delta \hat{\boldsymbol{\sigma}} - (\mathbf{E}_u \hat{\mathbf{u}}^p)^T \hat{\mathbf{r}}_{n+1} - \Delta \hat{\mathbf{u}} (\mathbf{B}^T \hat{\boldsymbol{\sigma}}_{n+1} - \mathbf{f} - \mathbf{E}_u \hat{\mathbf{r}}_{n+1}) - \sum_{j=1}^{n_\sigma} \Delta \hat{\lambda}^j F(\hat{\boldsymbol{\sigma}}_{n+1}^j) \quad (3.34)$$

Differentiating \mathcal{L} with respect to the reaction force $\hat{\mathbf{r}}_{n+1}$ leads to

$$\frac{\partial \mathcal{L}}{\partial \hat{\mathbf{r}}_{n+1}} = -\mathbf{E}_u \hat{\mathbf{u}}^p + \mathbf{E}_u \Delta \hat{\mathbf{u}} = \mathbf{0} \quad (3.35)$$

which is the displacement boundary condition (3.3b). For dynamic problems, the imposition of displacement boundary conditions is operated in the same manner.

3.4.2 Reformulation to a SOCP problem

The aforementioned optimization problem can be reformulated as a standard second-order cone programming (SOCP) problem in a form of:

$$\min_{\mathbf{x}} \quad \mathbf{c}^T \mathbf{x} \quad (3.36a)$$

$$\text{subject to} \quad \mathbf{a} \mathbf{x} = \mathbf{b} \quad (3.36b)$$

$$\mathbf{x} \in \mathcal{H} \quad (3.36c)$$

where \mathbf{x} is the vector of optimization variables, \mathbf{a} , \mathbf{b} and \mathbf{c} are the matrix and vectors of factors, and \mathcal{H} is a tensor product of second-order cones such that $\mathcal{H} = \mathcal{H}_1 \times \dots \times \mathcal{H}_l$. The second-order cones can be in the type of:

- Quadratic cone:

$$\mathcal{H}_q^n = \mathbf{x} \in \mathbb{R}^n : x_1 \geq \sqrt{x_2^2 + \dots + x_n^2} \quad (3.37)$$

- Rotated quadratic cone:

$$\mathcal{H}_r^n = \mathbf{x} \in \mathbb{R}^n : 2x_1 x_2 \geq \sum_{j=3}^n x_j^2, x_1, x_2 \geq 0 \quad (3.38)$$

Specifically, the SOCP problem equivalent to the maximization problem (3.32) is

$$\min_{\mathbf{x}_{n+1}} m + s + \sum_{j=1}^{n_c} g_{0j} p_j \quad (3.39a)$$

$$\text{subject to } \mathbf{B}^T \hat{\boldsymbol{\sigma}}_{n+1} + \mathbf{A}^T \hat{\boldsymbol{\sigma}}_{n+1} + \mathbf{E}_c^T \boldsymbol{\rho} = \tilde{\mathbf{f}} \quad (3.39b)$$

$$\left(\frac{1}{2} \Delta \hat{\boldsymbol{\sigma}}^T \mathbf{C} \Delta \hat{\boldsymbol{\sigma}} \leq m \right) \begin{cases} \mathbf{y} = \mathbf{C}^{\frac{1}{2}} \Delta \hat{\boldsymbol{\sigma}} \\ n = 1 \\ 2mn \geq \mathbf{y}^T \mathbf{y} \end{cases} \quad (3.39c)$$

$$\left(\frac{1}{2} \Delta t^2 \hat{\boldsymbol{\gamma}}_{n+1}^T \mathbf{D} \hat{\boldsymbol{\gamma}}_{n+1} \leq s \right) \begin{cases} \mathbf{k} = \Delta t \mathbf{D}^{\frac{1}{2}} \hat{\boldsymbol{\gamma}}_{n+1} \\ l = 1 \\ 2sl \geq \mathbf{k}^T \mathbf{k} \end{cases} \quad (3.39d)$$

$$\text{Contact constraints} \begin{cases} p_j = -\mathbf{n}_j^T \boldsymbol{\rho}_j \\ q_j = -\hat{\mathbf{n}}_j^T \boldsymbol{\rho}_j \\ \mu p_j \geq \sqrt{(q_j)^2 + \mathbf{0}_j} \end{cases}, j = 1, \dots, n_c \quad (3.39e)$$

$$(F(\hat{\boldsymbol{\sigma}}_{n+1}^j) \leq 0) \begin{cases} \chi^j = \mathbf{H} \hat{\boldsymbol{\sigma}}_{n+1}^j + \mathbf{d} \\ \chi_1^j \geq \sqrt{(\chi_2^j)^2 + (\chi_3^j)^2} \end{cases}, j = 1, \dots, n_\sigma \quad (3.39f)$$

where \mathbf{x}_{n+1} is the vector consisting of all the optimization variables. The SOCP problem (3.39) is obtained by first converting the quadratic terms $\frac{1}{2} \Delta \hat{\boldsymbol{\sigma}}^T \mathbf{C} \Delta \hat{\boldsymbol{\sigma}}$ into the objective function of (3.32) into the minimization of a scalar variable (i.e. variable m in (3.39a)) subject to linear equalities and rotated quadratic constraints (i.e. (3.39c)). The same operation is applied to $\frac{1}{2} \Delta t^2 \hat{\boldsymbol{\gamma}}_{n+1}^T \mathbf{D} \hat{\boldsymbol{\gamma}}_{n+1}$ in the objective function resulting in the variable s in (3.39a) and the constraints in (3.39d). Contact constraints in (3.32d-f) are reformulated as those in (3.39e), where quadratic constraints are enforced. The yield criterion $F(\hat{\boldsymbol{\sigma}}_{n+1}^j) \leq 0$ is equivalent to the constraints in (3.39f). In our simulations, the Mohr-Coulomb criterion is adopted which in a plane-strain case is

$$F(\boldsymbol{\sigma}_{xx}, \boldsymbol{\sigma}_{yy}, \boldsymbol{\sigma}_{xy}) = \sqrt{(\boldsymbol{\sigma}_{xx} - \boldsymbol{\sigma}_{yy})^2 + 4\boldsymbol{\sigma}_{xy}^2} + (\boldsymbol{\sigma}_{xx} + \boldsymbol{\sigma}_{yy}) \sin \phi - 2c \cos \phi \leq 0 \quad (3.40)$$

and thus the according $\chi, \mathbf{H}, \mathbf{d}$ in (3.39f) are:

$$\chi = (\chi_1, \chi_2, \chi_3), \quad \sigma = (\sigma_{xx}, \sigma_{yy}, \sigma_{zz}, \sigma_{xy}) \quad (3.41a)$$

$$\mathbf{H} = \begin{bmatrix} -\sin\phi & -\sin\phi & 0 \\ 1 & -1 & 0 \\ 0 & 0 & 2 \end{bmatrix} \quad \text{and} \quad \mathbf{d} = [2c \times \cos\phi \quad 0 \quad 0]^T \quad (3.41b)$$

3.4.3 Solution using MOSEK

The resulting SOCP problem (3.39) can be resolved using the IPM which is a robust solution scheme available in MOSEKMOSEK (2019). In this section, the program submitted to MOSEK for the solution is presented in detail. All information of the program is restored in an object called '*prob*' in MOSEL. Specifically, the optimization variables of SOCP problem (3.39) are as follows:

$$\mathbf{x} = \{\hat{\sigma}_{n+1}, \chi, \mathbf{y}, m, n, l, s, \hat{\gamma}_{n+1}, \mathbf{k}, \rho, p, q, \mu p, \mathbf{0}\} \quad (3.42)$$

and the corresponding vectors \mathbf{c} and \mathbf{b} and the matrix \mathbf{a} (see also problem (3.36)) are

$$prob.c = [\mathbf{0}; \mathbf{0}; \mathbf{0}; 1; 0; 0; 1; \mathbf{0}; \mathbf{0}; \mathbf{0}; g_0; \mathbf{0}; \mathbf{0}; \mathbf{0}], \quad (3.43a)$$

$$prob.a = \begin{bmatrix} \mathbf{B}^T & \dots & \mathbf{A}^T & \dots & \mathbf{E}_c^T & \dots \\ -\mathbf{H} & diag(1) & \dots & \dots & \dots & \dots \\ -\mathbf{C}^{1/2} & \mathbf{0} & diag(1) & \dots & \dots & \dots \\ \dots & \dots & 1 & \dots & \dots & \dots \\ \dots & \dots & 1 & \dots & \dots & \dots \\ \dots & \dots & -\Delta t \mathbf{D}^{1/2} & diag(1) & \dots & \dots \\ \dots & \dots & \mathbf{n}^T \mathbf{E}_c^T & diag(1) & \dots & \dots \\ \dots & \dots & \hat{\mathbf{n}}^T \mathbf{E}_c^T & \dots & diag(1) & \dots \\ \dots & \dots & diag(-\mu) & \dots & diag(1) & \dots \\ \dots & \dots & \dots & \dots & \dots & diag(1) \end{bmatrix}, \quad (3.43b)$$

$$prob.blc = prob.buc = [\tilde{\mathbf{f}}; \mathbf{d}; -\mathbf{C}^{\frac{1}{2}} * \hat{\sigma}_n; 1; 1; \mathbf{0}; \mathbf{0}; \mathbf{0}; \mathbf{0}; \mathbf{0}]. \quad (3.43c)$$

The linear equality constraint (3.36b) is implemented as the lower and upper bounds, namely, $prob.blc \leq prob.ax \leq prob.buc$. The inequality constraints are in the form of quadratic or rotated quadratic cones. There are a total of $n_c + n_\sigma + 2$ conic cones according to the expression in (3.39c)-(3.39f). Specifying the type of each cone and the index of its members in \mathbf{x} , the conic constraints can be defined straightforwardly in '*prob*'. A detailed solution scheme

for the SOCP-FEM analysis is provided in Algorithm 1 for reference. The optimization solver returns the structure type of the solutions named ‘*res*’ at the end of each analysis step, and the solutions of \mathbf{x} are contained in *res.sol.itr.xx*. The incremental displacement $\Delta\hat{\mathbf{u}}$ is the dual variable of $\hat{\gamma}_{n+1}$, and is stored in *res.sol.itr.y*. The optimization solver returns the

For *i*th incremental analysis:

1. Update the status of variables such as the velocity, the acceleration and the stress;
2. Form global matrices $\mathbf{A}, \mathbf{B}, \mathbf{C}, \mathbf{D}, \mathbf{H}, \mathbf{d}$ according to (3.28b-e) and (3.40);
3. Calculate $\tilde{\mathbf{f}}$ according to Eq. (3.28a);
4. Contact detection:
 - (1) Calculate g_0 of potential contact nodes;
 - (2) Update normal vectors in Eqs. (3.32d)-(3.32e) with inclined slope angle θ_s ;
5. Construct the SOCP program based on Eq. (3.43) and submit to MOSEK;
6. Extract/calculate the status variables:
 - (a) Find stresses $\hat{\sigma}_{n+1}$ in *res.sol.itr.xx*;
 - (b) Calculated velocity $\hat{\mathbf{v}}_{n+1}$ with $\Delta\hat{\mathbf{u}}$ obtained from *res.sol.itr.y*;
 - (c) Calculate the increment of strain tensors using Eq. (2.2) and Eq. (2.5);

Return to step 1 with $i = i + 1$

Algorithm 1: Solution scheme

structure type of the solutions named *res* at the end of each analysis step, and the solutions of \mathbf{x} are contained in *res.sol.itr.xx*. The incremental displacement is the dual variable of the stresses and is stored in *res.sol.itr.y*.

3.5 Particle finite-element technique

Originated in the fluid mechanics, the PFEM has demonstrated its capabilities of tackling issues such as free-surface evolution and mesh distortion. Some challenging fluid mechanics problems that have been solved successfully include, but are not limited to, the modelling of free-surface flows and their interaction with solid structures, wave breaking, multi-phase flows, etc. (Idelsohn et al., 2003, 2004; Oñate et al., 2011, 2004). The key idea behind the PFEM rests with the treatment of mesh nodes as free particles which can move and even

separate from the computational domain to which they originally belong. In a given time interval $[t_n, t_{n+1}]$, the basic steps of the PFEM are as follows (see also Fig. 3.3):

- 1. Erase the mesh topology and update the position of mesh nodes based on the solved incremental displacement to obtain a cloud of particles, C_{n+1} (Figs. 3.3(a) and (b)).
- 2. Use the α -shape method (Cremonesi et al., 2010) to identify the new computational domain Ω_{n+1} based on C_{n+1} (Fig. 3.3(c)).
- 3. Remesh the domain Ω_{n+1} to obtain a new mesh M_{n+1} (Fig. 3.3(d)).
- 4. Map the history variables from the old mesh M_n to the new mesh M_{n+1} using the Unique Element Method (UEM) introduced in Hu and Randolph (1998).
- 5. Solve the equations using Algorithm 1 based on the new mesh M_{n+1} .

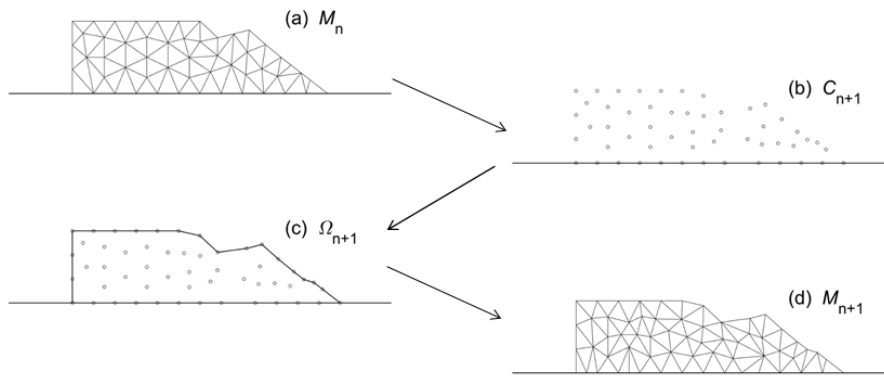


Fig. 3.3 Steps for PFEM techniques in the time interval $[t_n, t_{n+1}]$.

It is worth noting that the governing equations used in this PFEM version are under the assumption of infinitesimal strain. At the end of each incremental analysis, the configuration is updated according to the solved displacement. This assumption may lead to several errors for large deformation analysis. However, practically the error induced due to the infinitesimal strain assumption is relatively minor because the used incremental step is very small. The present version of the PFEM with small strain theory has been validated against several benchmarks such as the modelling of a water dam break, granular column collapse, underwater granular flows and the related induced waves, and non-Newtonian flows in an annular viscometer in (Zhang et al., 2019) where satisfactory agreements between the PFEM simulation results and the available experimental data and/or analytical results have been obtained. For the PFEM derived from the concepts of large-strain plasticity and its application

to granular material flows which are closely related to landslide propagations, readers are referred to Dávalos et al. (2015). More specifically, an investigation of ‘Remeshing and Interpolation Technique with Small Strain’ (RITSS) for large deformation analysis in soil has shown that the RITSS procedure with small time steps leads to relatively small errors when applied to geotechnical problems (Tian et al., 2014). As for the accuracy of UEM, more details can be found in Hu and Randolph (1998), where numerical results of the bearing capacity problem using UEM and coarse meshes is compared with analytical solutions: the fluctuation of the load-displacement curve is within 6%, which can be further reduced by adopting finer meshes.

Chapter 4

Applications of landslide modelling

The details of the optimization-based PFEM applied to landslide modelling has been explained in Chapter 3, and its applications have been explored through modelling a flow-like landslide (Zhang et al., 2015), the progressive failure of landslides in sensitive clays (Zhang et al., 2017) as well as submarine landslides and their consequences such as the induced tsunamis and the impact to ocean pipelines (Zhang et al., 2019). However, there are few efforts devoted to studies comparing the optimization-based PFEM vs. the common approaches for landslide modelling in geosciences (e.g. vs. depth-averaged approaches). The objective of this section is to quantitatively assess the performance of the present model in landslide modelling with two main applications: (1) stability analysis; (2) landslide propagation analysis. As mentioned, these two stages are usually simulated separately by numerical techniques addressing pre-failure and post-failure analyses. Therefore, the performance of the model developed in this thesis is discussed through comparisons against the most commonly used techniques. Specifically, the stability analysis is carried out based on a typical homogeneous slope benchmark (see Cheng et al., 2007) and the propagation analysis is conducted with the presented depth-averaged model in Chapter 2. Some parts of this section have been published in Wang et al. (2019b).¹

4.1 Stability analysis

Slope stability analysis is a classical problem in the field of geological, geophysical and engineering. The quantitative analysis of slope stability starts from the fundamental work by Bishop (1955), in which the slice-based limit equilibrium method (LEM) was used for

¹Most contents in this section have been summarized in a paper published in: Wang, L., Zhang, X., Zaniboni, F., Oñate, E., & Tinti, S. (2019). Mathematical optimization problems for particle finite element analysis applied to 2D landslide modeling[J]. *Mathematical Geosciences*, 1-23.

predicting slope stability. Due to its simplicity, the use of LEM has been widely adopted in engineering applications even though it is known that some assumptions are over simplified and there is not a unique solution for it. The LEM uses the global equilibrium condition and the slices are treated as being in purely static situation without constitutive relationships. Later, the use of the limit analysis method that models the soil as a perfectly plastic material obeying an associated flow rule became popular. In this approach two plastic bounding theorems (lower and upper bounds) can be used to determine the computational value (Chen, 2013). In order to automatically obtain the slip surface through the computation, proper stress-strain relationships should be implemented to account for the evolution of the slip surface, which can be identified by the shear strain. With the successes of the development of the finite element method (FEM) in engineering, the advantages of FEM in the elastoplastic analysis of slopes have been recognised. They can be summarized as follows (Griffiths and Marquez, 2007):

- failure surface is not needed to be predefined
- balance relationship between slices is avoided
- information inside the slope body can be described
- capability to simulate slope failures that can be observed in reality

Thereby, numerical techniques especially the finite-element analysis has become the dominant approach in the slope stability analysis nowadays. Usually the factor of safety (*FOS*) is chosen as the index to determine the situation of slopes. Combined with the present model for 2D elastoplastic plane-strain problems, a simply binary search algorithm is implemented to compute the critical situation of slopes in this section.

4.1.1 FEM analysis

Practically, the stability analysis of a slope is carried out using the strength reduction method (SRM) to identify the critical state of the slope by gradually reducing the strength of the soil. The critical state is indicated by the factor of safety (*FOS*) that is defined as the ratio of the actual soil shear strength to the minimum shear strength required to prevent failure (Bishop, 1955). For example, when the Mohr-Coulomb model is used with cohesion c and internal frictional angle ϕ , then according to the SRM (Dawson et al., 1999), these parameters are reduced by a reduction factor (*RF*) that is:

$$c' = \frac{c}{RF}, \quad \tan\phi' = \frac{\tan\phi}{RF} \quad (4.1)$$

The RF is the FOS of the slope when the used c' and $\tan\phi'$ are at the minimum values required to prevent failure. In other words, a slope with a FOS greater than one is identified as stable otherwise it is unstable. To verify the accuracy of the SOCP-FEM approach for slope stability analysis, a homogeneous soil slope that was analyzed using the limit equilibrium method (LEM) and the finite element method by Cheng et al. (2007), is re-examined in this section. The initial geometry of the example is illustrated in Fig. 4.1. The density, elastic modulus and Poisson's ratio of the soil are $2000\text{kg}/\text{m}^3$, 14MPa and 0.3 , respectively. Simulations with both the associated ($\psi = \phi$) and non-associated ($\psi = 0^\circ$) flow rules are conducted using SOCP-FEM under quasi-static assumptions with material parameters in line with those in Cheng et al. (2007). For the case of non-associated flow rule, the strategy presented in Krabbenhoft et al. (2012a) is utilized. A total of 6095 triangular elements are used to discretize the slope in our simulations.

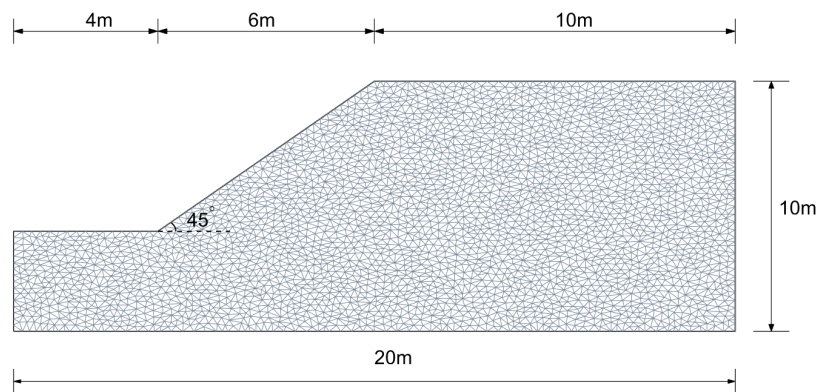


Fig. 4.1 Initial geometry of the slope model. Lateral displacement is set to zero along left and right boundaries and the bottom is fully fixed.

The binary search algorithm illustrated in Fig. 4.2 is employed to calculate the FOS . The critical failure state of a slope is determined when the optimization solver is not feasible or the maximum incremental displacement is higher than a given threshold. For the static analysis, the incremental displacement of the failed zone should be infinite. So, the threshold used here is to approach the critical situation. Several thresholds varying from 0.1 m to 100 m have been used and no significant effects on FOS are found. For an engineering point of the permanent displacement of slopes, more investigations should be devoted to the dynamic analysis of the slope since the time-dependent information is available. It will be shown later that the weakening process may play a significant role in the slope failures

according to our simulations. Here, an initial range [$RF1 = 0.2, RF2 = 10$] is set to trigger the searching process and when the tolerance $|RF1 - RF2|/RF1 < 10^{-3}$ is achieved, the calculated reduction factor RF1 is the FOS of the slope. For the non-associated flow rule, the plastic potential function is not equivalent to the yield function, i.e.:

$$F = \sqrt{(\sigma_{xx} - \sigma_{yy})^2 + 4\sigma_{xy}^2} + (\sigma_{xx} + \sigma_{yy})\sin\phi - 2ccos\phi \quad (4.2a)$$

$$G = \sqrt{(\sigma_{xx} - \sigma_{yy})^2 + 4\sigma_{xy}^2} + (\sigma_{xx} + \sigma_{yy})\sin\psi \quad (4.2b)$$

By means of the approximation form of the yield function, the non-associated flow rule can be expressed as an associated flow rule (Krabbenhoft et al., 2012a), which can be tackled by the present min-max program.

$$F \approx F^* = \sqrt{(\sigma_{xx} - \sigma_{yy})^2 + 4\sigma_{xy}^2} + (\sigma_{xx} + \sigma_{yy})\sin\psi - 2\tilde{c}cos\psi \quad (4.3a)$$

$$\tilde{c} = c \frac{\cos\phi}{\cos\psi} + \frac{1}{2} \left(\tan\psi - \frac{\sin\phi}{\cos\psi} \right) (\sigma_{xx} + \sigma_{yy})_n \quad (4.3b)$$

where \tilde{c} is updated every time step to guarantee the accuracy of the approximation. The subscript n refers to the current state at time t_n . Additionally, an error control scheme proposed by Wang et al. (2018) replaces the dilation angle by an automatically determined ϕ_k . The angle ϕ_k approaches to the dilation angle ψ as the internal loop increases and the loop ends when the increment displacement field suffers a control error from the reduction of ϕ_k . The error control scheme improves the accuracy of the stability analysis of slopes with non-associated Mohr-Coulomb material. Also, a comparison between the searching process for FOS using traditional FEM and using the mathematical-optimization based finite element analysis can be found in Wang et al. (2018). With the examples shown in Table 4.1, numerical results by SOCP-FEM are compared with the results in Cheng et al. (2007). SOCP1 and SOCP2 denote the SOCP-FEM with non-associated flow rule and with associated flow rule.

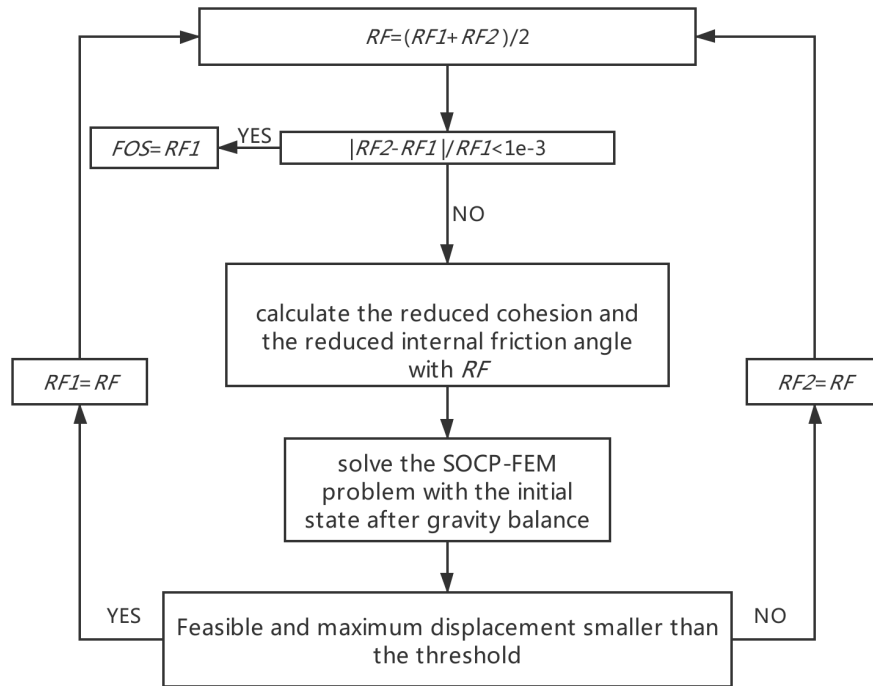


Fig. 4.2 Searching strategy for FOS.

Table 4.1 Factor of safety determined by the limit equilibrium method (LEM), the strength reduction method with a non-associated flow rule (SRM1) and an associated flow rule (SRM2), SOCP1 and SOCP2. Diff1 is the percentage difference between the FOSs obtained from SRM1 and SOCP1 in absolute value, while Diff2 is the same but applied to SRM2 and SOCP2. The data of LEM, SRM1 and SRM2 are from Cheng et al. (2007)

Case	c (kPa)	ϕ ($^{\circ}$)	LEM	SRM1	SOCP1	Diff1 (%)	SRM2	SOCP2	Diff2 (%)
1	5	5	0.41	0.43	0.42	2.3	0.43	0.43	0.0
2	5	15	0.70	0.73	0.71	2.7	0.73	0.72	1.4
3	5	25	0.98	1.03	1.02	1.0	1.03	1.00	2.9
4	5	35	1.28	1.34	1.32	1.5	1.35	1.31	3.0
5	10	5	0.65	0.69	0.67	2.9	0.69	0.68	1.4
6	10	15	0.98	1.04	0.99	4.8	1.04	1.01	2.9
7	10	25	1.30	1.36	1.32	2.9	1.37	1.33	2.9
8	10	35	1.63	1.69	1.63	3.6	1.71	1.68	1.8
9	20	5	1.06	1.20	1.16	3.3	1.20	1.18	1.7
10	20	15	1.48	1.59	1.51	5.0	1.59	1.55	2.5
11	20	25	1.85	1.95	1.83	6.2	1.96	1.91	2.6
12	20	35	2.24	2.28	2.24	1.8	2.35	2.30	2.1

4.1.2 Post-failure analysis by PFEM

In the framework of the PFEM, not only the FOS of a slope can be determined but also the post-failure processes and final run-out distances for different reduction factors. This can be achieved through the dynamics analysis. To illustrate this capability, case 12 in Table 4.1 is re-analyzed with the non-associated flow rule. Four different reduction factors are used and the corresponding final deposits from the simulations are illustrated in Fig. 4.3.

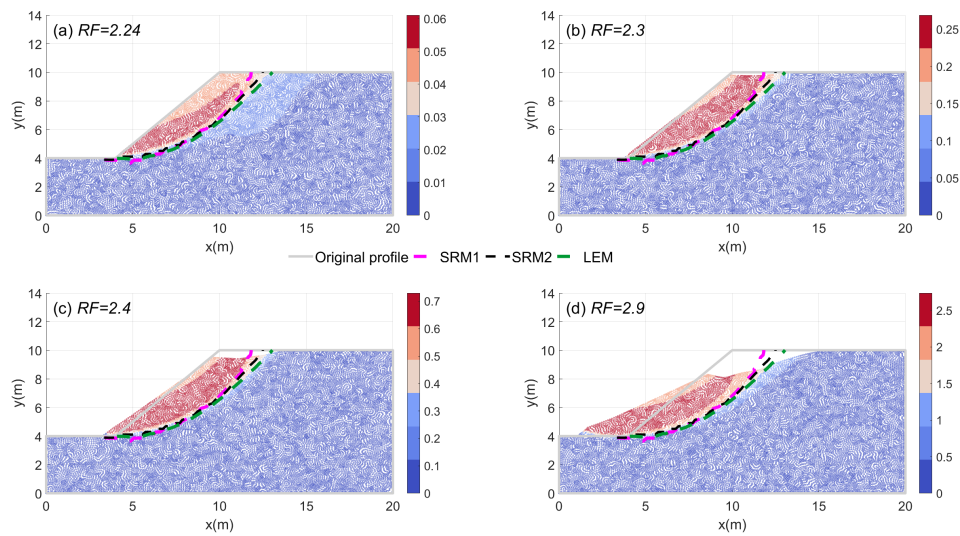


Fig. 4.3 Final deposits obtained from the PFEM simulation for the reduction factor (a) $RF = 2.24$, (b) $RF = 2.3$, (c) $RF = 2.4$ and (d) $RF = 2.9$. Contours refer to the displacement of soils (unit: meter), and the slip surfaces from the analysis by SRM1, SRM2 and LEM are extracted from Cheng et al. (2007).

As displayed, for $RF = 2.24$ and 2.3 clear sliding surfaces are identified from the PFEM simulation which coincide with the slip surfaces determined by other approaches (Figs. 4.3 (a) and (b)). However, soil elements in these two cases experience very small displacements. This is because the used reduction factors are very close to the factor of safety of the slope implying that the slope will tend to be stable again after limited deformation. For $RF = 2.4$ (Fig. 4.3(c)), deformation is well identified and the maximum displacement around 0.7 m is experienced by soil nodes along the slip surface. Increasing further the reduction factor leads to greater deformations. For example, when $RF = 2.9$, the sliding mass has a moving distance exceeding 2 meters, which has been well predicted by our approach. The present simulations indicate that the run-out distance of landslides might be slightly small if without further material-weakening, which is due to the redistribution of stress and material. This also

indicates that the material-weakening behaviour may play a significant role in the evolution of some large landslides.

4.2 Landslide propagation

The landslide propagation involves the accurate description of the rheological behaviour of landslides. Due to the limitation of traditional FEM in dealing with large deformation problems, the run-out analysis of landslides mainly focuses on the fluid-like behaviour based on the Eulerian approaches. Based on the present PFEM model, traditional FEM analysis can be extended to the description of landslide propagation. By means of the non-associated Mohr-Coulomb, the Drucker-Prager and the Tresca yield criterion, the present SOCP-PFEM has been applied to the examples of granular collapse and dam-break problems (Zhang et al., 2013, 2019). In this section, the present PFEM model is compared against the results of the widely used depth-averaged model applied to the landslide propagation problem and also with Laboratory test and a real landslide data.

4.2.1 Laboratory test

In Chapter 2, the developed DAEs code has been validated against the water-dam break problems, where the flow-like behaviour of the material is simulated. The comparison with analytical results proves the accuracy of the code and the comparison with the observation data from EU CADAM laboratory experiment validate the capability of the shallow-water model with hydraulic friction effects in water-flow simulations. Here, a laboratory test of the collapse of aluminum bars is used as an example for the numerical investigations. Small aluminum bars of diameters 1 and 1.55 mm, and length 50 mm are used to represent soil. The initial model is a rectangular area of 200×100 mm and is generated by placing two flat solid walls on a flat surface. The aluminum bars mainly move along the longitudinal direction leading to a 2D configuration. Square grids were plotted to visualize the profiles and the experiment was started by quickly removing the right-end wall to right. More details can be found in Bui et al. (2008).). In the same paper, the smoothed particle hydrodynamic (SPH) associated with the Drucker-Prager constitutive model is used to capture the large deformation and failure of this experiment, where good agreements are obtained. Later, different numerical results have been compared based on the experimental data (e.g., Lian et al., 2012; Peng et al., 2016; Zhang et al., 2019).

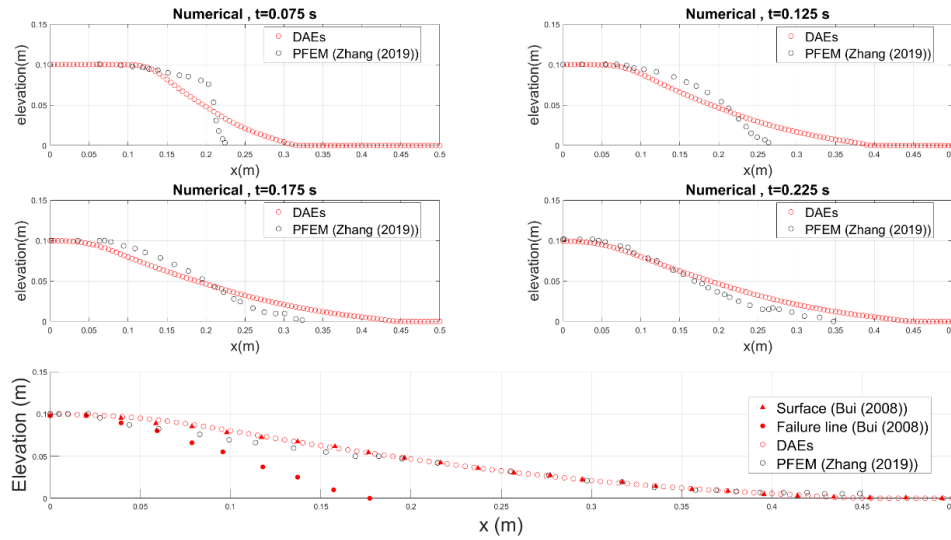


Fig. 4.4 Numerical results at five moments: $t = 0.075$ s, $t = 0.125$ s, $t = 0.175$ s, $t = 0.225$ s and the final deposit profile.

In this part, we focus on the simple comparison between the PFEM model and the depth-averaged model in this experiment. It should be mentioned that the adopted depth-averaged model is the simple shallow water model with the basal Mohr-Coulomb law Savage and Hutter (1989), better results can be obtained by the advanced models that are able to describe the internal rheology. The Mohr-Coulomb model is implemented into the PFEM model and parameters are: Young's Modulus $E = 0.84$ MPa, Poisson's ratio $\mu = 0.3$, friction angle $\phi = 19.8^\circ$, dilation angle $\psi = 0^\circ$ and cohesion $c = 0$. The time step is set to $\Delta t = 1 \times 10^{-3}$ s (Zhang et al., 2019). As for the Depth-averaged model, only the basal friction angle is needed and it is set to $\phi = 19.8^\circ$.

4.2.2 Tangjiashan Landslide

Computing the propagation of landslides requires the accurate description of the rheological behavior of the involved geomaterials. In the present PFEM framework, more sophisticated material constitutive models can be implemented for landslide propagation. It is of interest to compare the simulation results of a real landslide case obtained from the present PFEM method and those from the depth-averaged models.

To this end, a historical event, i.e. the Tangjiashan mass failure in Sichuan province, China, is addressed in this section (Fig. 4.5). The failure was triggered by the 2008 Wenchuan earthquake and the sliding mass crashed rapidly into the Jianjiang river, causing a landslide dam and a death toll up to 84 (Luo et al., 2012; Xu et al., 2009). The slide moved along

a complex topography with a maximum slope angle of 40° the motion lasted around 30 s according to (Xu et al., 2009). The data about the landslide body and the deposit are extracted from the field survey conducted by (Hu et al., 2009). In our PFEM simulation, the domain is discretized by using 3335 elements and a time step Δt of 0.1 s is used. According to Huang et al. (2012), the sliding mass can be represented by a Mohr-Coulomb model with the following material parameters: density $\rho = 2000\text{kg/m}^3$, friction angle $\phi = 30^\circ$, dilation angle $\psi = 0^\circ$, and cohesion $c = 30\text{kPa}$. The basal friction coefficient is chosen as $\mu = 0.27$. As for the time integration, the backward Euler scheme, i.e. $\theta_1 = \theta_2 = 1$, is implemented into the PFEM simulation.

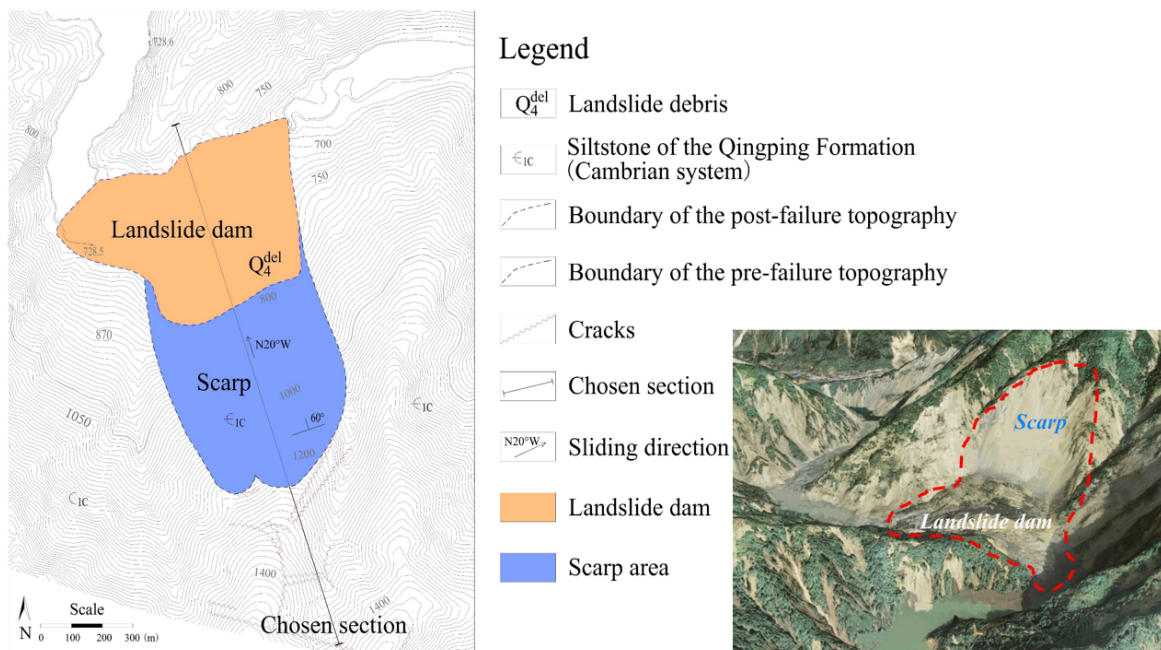


Fig. 4.5 Background of Tangjiashan landslide: **Left** Engineering geology map (modified from Hu et al. (2009) and Xu et al. (2009)); **Right** Satellite image (modified after Peng and Zhang (2012)).

In addition to the PFEM, the simulation of the landslide motion was also carried out by using the depth-averaged model shown in section 2.4.1. In contrast to the present PFEM model, the adopted depth-averaged model only considers the basal Mohr-Coulomb friction law, mainly used for simulating the flow-like behavior of mass-flow movements. Therefore the needed material parameters is the basal frictional coefficient $\mu = 0.27$. In the simulation, the lateral earth pressure coefficient (Savage and Hutter, 1989) is assumed to unity.

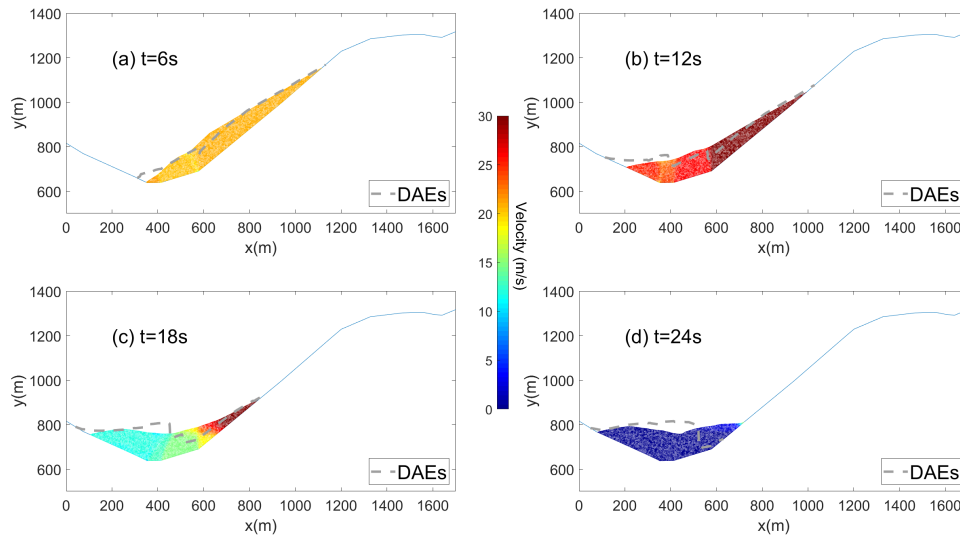


Fig. 4.6 Simulated propagation with velocity contour at four moments.

The landslide position simulated by the PFEM analysis with velocity magnitude contour at four different moments are shown in Fig. 4.6 and the dash line represents the simulation conducted by the depth-averaged model. At $t = 6\text{s}$, the landslide moves as a whole with the velocity around 20 m/s and the DAEs model depicts a slightly faster motion. Further, velocity distinctions within the landslide body in PFEM simulation can be observed when the mass climbs the opposite side of the mountain. Impeded by the anti-slope, the front of the landslide decelerates rapidly, while the rear of the landslide still moves with a velocity higher than 25 m/s . On the contrary, it is clear that the landslide depicted by the DAEs simulation suffers a larger deformation and the mass accumulates in the front of the landslide (see in Fig. 4.6(c-d)). The movement of the rear sector changes the deposit profile of the landslide shown in Fig. 4.6(d). The main body described by the PFEM model is still, while the mass depicted by DAEs is impeded by the front mountain and starts moving back. The present PFEM model describes the Tangjiashan landslide moving more like a rigid body and differs in this aspect from the DAEs simulation.

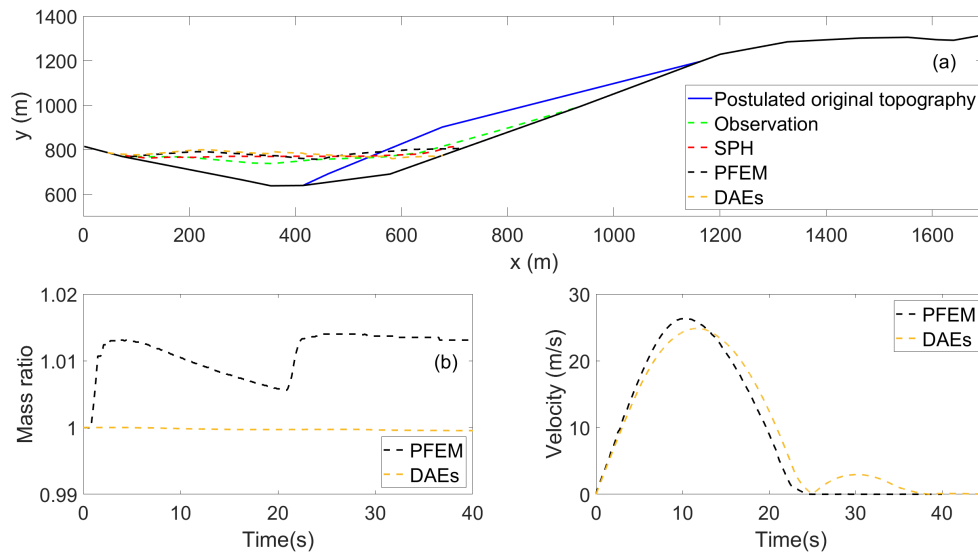


Fig. 4.7 (a) deposit profile; (b) Mass variation; (c) Mean velocity profile

The simulations agree well with the observation data and also with the SPH simulation. Calculating the area of the initial and final cross-sections of the computational domain, the mass variations of the simulations are shown in Fig. 4.7(b), where the maximum of 1.5% mass change is produced by the remeshing procedure in PFEM simulation. The mass balance of the DAEs simulation is well kept. Considering the landslide as a whole, the mean velocity profile of the landslide is shown in Fig. 4.7(c). In the PFEM simulation, the landslide was accelerated to around 26 m/s in the first 10 s and then decelerated to still. As for the DAEs simulation, the main mean velocity profile is quite similar, while an additional velocity profile is produced due to the back motion of the landslide body. In general, the present two simulations are nearly consistent in capturing the main motion of the Tangjiashan landslide with differences in the internal motion inside the landslide body, depicted by the landslide profile.

Chapter 5

Entire simulation of landslides

With some assumptions, physically-based models can provide the dynamic information of landslides such as travel distance, impact forces, hazardous areas for the assessment of landslide hazards. Usually these models can be integrated into Geographic Information System (GIS) with some techniques, such as Monte Carlo techniques and multiple flow direction algorithms, to predict mass movements at different scales (Mergili et al., 2017). Mostly, depth-averaged equations (DAEs) are used to account for the flow dynamics since they can be easily developed and solved for different scales. For some landslides, the onset of slope failure is at small scale and the landslide propagation is at a larger scale. Therefore, modelling the dynamics of landslides including different scales is a challenging task. Currently, several numerical methods can be used for the analysis of landslides from initiation and deposition stages, as reviewed in (Soga et al., 2015). And a study on a virtual slope model based on MPM has been conducted by (Yerro et al., 2016) to investigate the response of slope to the reduction of the material strength. It has been proven in Chapter 4 that our particle finite element method (PFEM) has the capability of simulating the entire evolution of the landslide from the generation to the deposition phase. Therefore it is important to figure out the difference between a unified PFEM simulation and the usually adopted approaches that separate failure mechanism (static analysis) and run-out analysis (dynamic analysis) based on real cases. In this Chapter, we first apply the PFEM code to a simple homogeneous slope model and numerical results reveal that under the so-called critical condition the landslide comes to a stop with a slight modification of the original profile, while the profile is drastically changed if strength reduction is further applied. To further explore the PFEM capability, we choose the 2013 Cà Mengoni landslide, northern Apennines, Italy, as a case study, since it behaved as if it were formed by a homogeneous material. In virtue of the back-analysis of the run-out distance that is performed by using different material strength parameters, we show that the PFEM model is able to capture

the variation of the observed landslide profile, and contributes to the understanding of the dynamics of the whole sliding process.

5.1 Critical condition

In Chapter 4, a slight deformation under critical condition (see Figure 4.3) has been depicted by the PFEM model with dynamic analysis. This phenomenon has also been reported by other methods (e.g. Cuomo et al., 2013; Peng et al., 2015; Yerro et al., 2016). A simple comparison is presented here to show the deposit profile of a homogeneous slope, simulated by PFEM and SPH methods. The latter method was applied by (Peng et al., 2015) methods who made use of the Drucker-Prager elastoplastic model with non-associated flow rule. In the SPH code, the simulations were conducted with material parameters modified by prescribed reduction factors that were set close to the critical safety factor, which is the so-called critical failure condition for the slope. The critical condition of a slope may be defined as the moment that the slope transits from a state of stability to instability. The material parameters for soil including elastic modulus E , internal friction angle ϕ , cohesion c , dilation angle ψ , Poisson's ratio ν and density ρ can be found in Table 5.1. By means of the shear strength reduction method (SSR), the strength parameters, i.e. cohesion and internal friction angle, are modified by the reduction factor (RF), the critical value for RF being approximately equal to the stability factor of the slope (FOS). The safety factor computed by static analysis in our model is 1.953 and is comparable with the published values of 1.94 (Griffiths and Lane, 1999; Peng et al., 2015). In this section, we adopt the critical reduction factor $RF = 1.953$ for the dynamic simulations to investigate how the slope evolves under the critical condition.

Table 5.1 Material parameters for homogeneous soil slope.

	E (MPa)	ϕ (°)	c (kPa)	ψ (°)	ν	ρ (kg/m ³)
Case	30	30	5	0	0.2	1850

The critical condition of a slope may be defined as the moment that the slope transits from a state of stability to instability. By means of the shear strength reduction method (SSR), the strength parameters, i.e. cohesion and internal friction angle, are modified by the reduction factor (RF), the critical value for RF being approximately equal to the stability factor of the slope (FOS). The safety factors computed by static analysis in our model is 1.953 respectively and is comparable with the published values of 1.94 (Griffiths and Lane, 1999; Peng et al., 2015). In this section, we adopt the critical reduction factor $RF = 1.953$ for the dynamic simulations to investigate how the slope evolves under the critical condition.

In the simulations, we chose the mesh element size with typical area of 0.16 m^2 for the slope, resulting in the corresponding total number of 1566 triangles. The adopted boundary conditions are that lateral nodes cannot have horizontal displacements and bottom nodes cannot move at all. The final deposit profile we obtain for the slope with our PFEM model is displayed in Fig. 5.1. It can be seen that the PFEM model, which has solid foundations in continuum mechanics, describes that the homogeneous slope stops with slight modification of the original profile. This result also suggests that the weakening process during the post-failure stage influences the mobility of shallow landslide and debris flows, which will be proven in the next section.

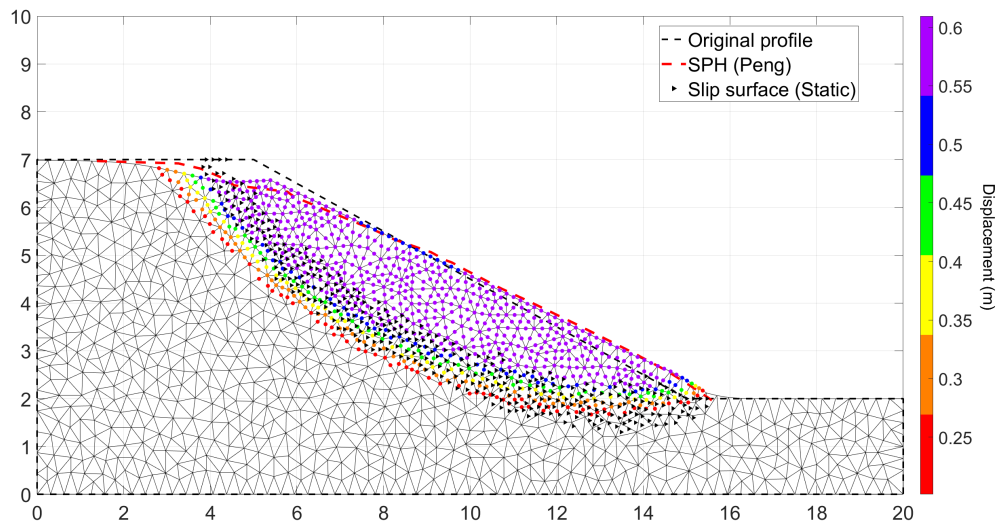


Fig. 5.1 Final profiles of the slope with distribution of displacement.

Naturally, it is of interest to investigate the dynamic evolution of the slope when the material strengths are further reduced. By the same SSR technique, individual reduction factors RFC and RFF are implemented to reduce cohesion and internal friction angle respectively. To quantify the run-out distance of the sliding body, the average displacement D is calculated by averaging the displacement of nodes that run distances more than 0.1 m. The value of D computed by the critical condition is denoted as D_c . The influence of RFC and RFF on the ratio between D and D_c is plotted in Fig. 5.2.

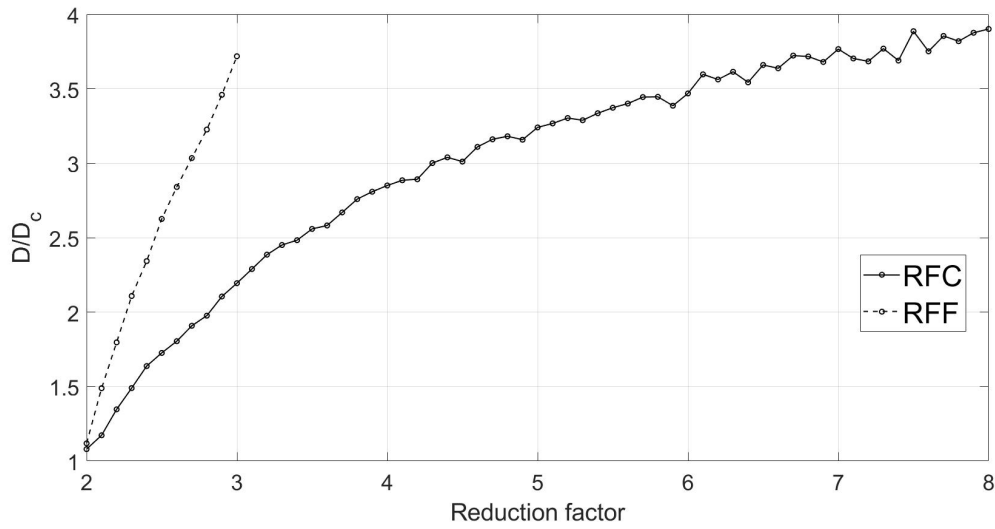


Fig. 5.2 Relationship between the ratio D/D_c and the reduction factors for cohesion and internal friction angle. The reduction factors are not further reduced beyond the limit shown in the graph, since the failure mass reaches the right lateral boundary of the numerical slope domain.

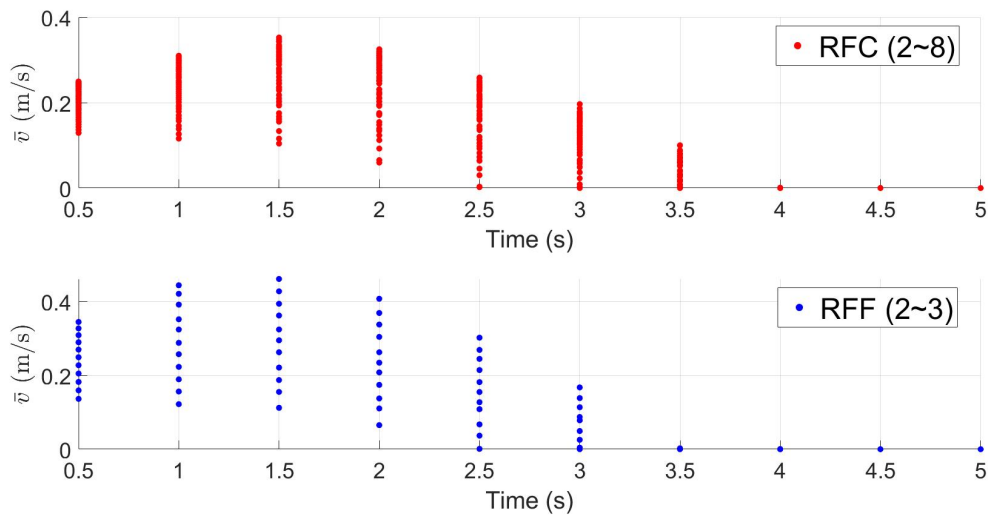


Fig. 5.3 Evolution of the average velocity \bar{v} of the sliding body, computed by averaging over the nodes that have the magnitude of velocity larger than 10^{-4} m/s.

The clearly sharp slope of the curve of RFF indicates that the reduction of friction angle has larger influence on the mobility of landslides. The dynamics of the landslide is also shown through the evolution of the average velocity in Fig. 5.3. After failure ($t = 0$ s), the main body achieves its peak velocity at $t = 1.5$ s and then decelerates to still within 4 s in total.

5.2 Case study: The 2013 Cà Mengoni landslide

As was mentioned already, the modern numerical techniques can be applied to the entire evolution of landslides from initiation to deposition. Nonetheless, few studies have been conducted to investigate the performance of these techniques based on a real case landslide. To explore its capability in capturing some landslide features, the Cà Mengoni landslide, that occurred on 6 April 2013 in the northern Apennines, close to Castel dell'Alpi, a village in the province of Bologna, Italy, is chosen as a case study. A detailed static slope stability analysis has been conducted by Berti et al. (2017), where the material strength parameters were back-analysed in details. The landslide is a flysch rock slide, and is of a type quite common in northern Apennines. Previous studies (Berti et al., 2017; Ronchetti et al., 2009) indicated that, despite its complexity, the flysch behaves as a homogeneous medium at the slope scale. Additionally, we note that the final profile of the 2013 Cà Mengoni landslide is similar to what is observed in the shallow movements of landslides. Therefore, we take this as a hint that our model based on continuum mechanics can be implemented to investigate this historical event. The strategy is to use the PFEM model to investigate the failure mechanism and profile variation from the perspective of analysing the final deposit with different parameters.

5.2.1 Background and slope model

The 2013 6th April Cà Mengoni landslide, located in the Apennines south of Bologna was triggered after a long period of rainfall with about 310 mm in 30 days, and finally deposited on 8th, April. The main motion of the landslide occurred in the early afternoon of 6th, April and then slowed down reaching a velocity less than 1 m/h in the late afternoon. The landslide, that has an estimated volume of 3 million m^3 , was witnessed moving with an approximately peak velocity of 10 m/h. The landslide mainly consists of a cretaceous flysch that is made of a close alternation of sandstones, siltstones, and marls. The detailed field survey reveals that the original slope was initialized within the flysch substratum. The geological, geotechnical, and geophysical investigations provide an interpretation of the failure mechanism of the landslide. It was postulated that the landslide experienced a three-stage mechanism, which

has been depicted in Fig. 5.4. After the first translational sliding of the landslide, the failure mass moved along a curvilinear surface at about 30 m depth. It was also postulated that multiple failure surfaces were generated during the failure of the landslide. More geological details can be found in Berti et al. (2017).

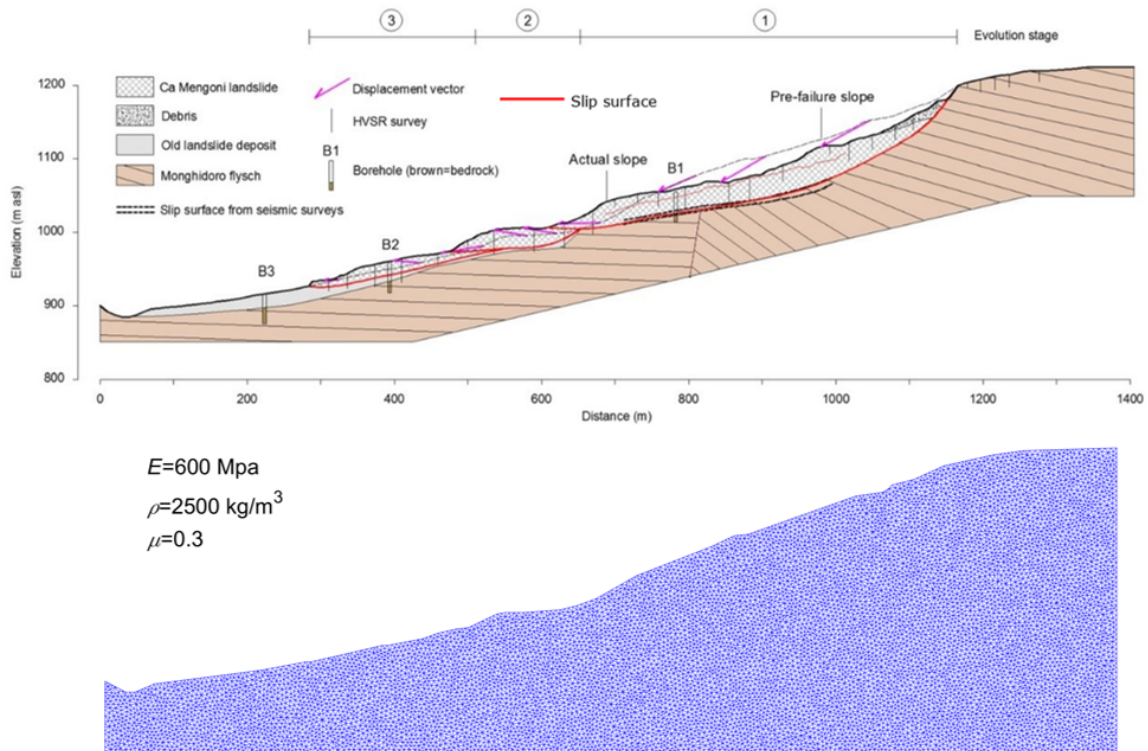


Fig. 5.4 Evolution and numerical set-up of of the main cross-section of the Cà Mengoni landslide (after Berti et al. (2017)).

The original, intermediate and final profiles of the landslide are shown in Fig. 5.4. The corresponding 2D numerical mesh in Fig. 5.4 consists of 21755 triangles with area of 25 m^2 . Values for elastic modulus E , density ρ and Poisson's ratio ν are taken from Berti et al. (2017) as well as the values for cohesion c and internal friction angle ψ , that are 30 kPa and 29° respectively. In the present model the material is one phase only, so the numerical slope model is stable with the chosen c and ϕ . Different reduction factors RFC and RFF are used to investigate the dynamic evolution of the landslide.

5.2.2 Numerical investigation

The dynamic evolution of landslides involves various mechanisms during different stages, while here we simulate the dynamic evolution of homogeneous material controlled by

the gravity force and local topography. In this section, we concentrate on the mass flow movements within shallow depth by implementing different material strength parameters. The performed numerical simulations are to investigate the slide motion from initiation to deposition. Current numerical simulations release material from a certain zone without the identification of the potential failure zone. With the aim to explore the performance of the PFEM model in describing the landslide processes in a single code, the numerical simulations are carried out separately in two steps: (1) Static analysis; (2) Dynamic analysis. The identification of unstable zones in mountain slopes is usually done by means of the shear strength reduction method associated with FEM. According to the previous studies on a simple geometry slope, the recognized landslide mass moves along the slip surface close to the one obtained from static analysis. It is of interest to compare the motion of the landslide simulated by the dynamic analysis with the slip surface identified by static analysis based on a more complicated slope model, since the stress conditions are changed during the dynamic computation.

Slip surface by static analysis

The Mohr-Columb model is implemented in the code to identify the slip surface of the slope. By means of the adopted material parameters associated with the algorithm presented in chapter 4, the obtained *FOS* are 1.5 and 1.545 respectively. The identified slip zones are shown in the *PEEQ* plots in Fig. 5.5. For the associated model, the toe of the slope starts to move when the reduction factor equals to 1.5, and this indicates a local failure of the landslide. Since the plastic zone depicted in Figure 5.5(a) does not show connection between the toe and the slope surface, a further check was carried out to check the robustness of *FOS* searching algorithm. With the associated Mohr-Coloumb model, the numerical landslide fails when *RF* is higher than 1.5. This slip zone shown in Figure 5.5(b) is deeper than the one observed and the one obtained by the finite difference analysis by Berti et al. (2017), where the water table was set at the ground. The *PEEQ* accumulates at the toe of the generated slip zone downhill and gradually decreases moving uphill. It should be noted that the slip surface obtained by means of the static analysis here is not the slip surface obtained by means of the dynamic analysis, which will be explained later on. Black dashed line in Fig. 5.5 represents the observed slip surface during the first stage of the landslide.

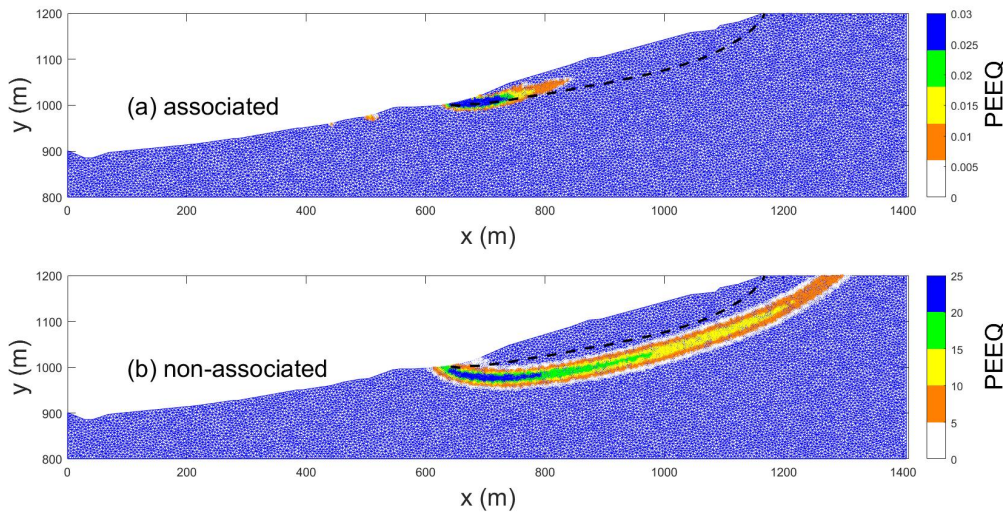


Fig. 5.5 Contour of $PEEQ$ under the critical condition for the slope models.

Dynamic evolution

The dynamic evolution of landslides involves several dynamic processes, such as the dynamic behavior of material and the redistribution of landslide slips. Unlike the single slip surface shown in Figure 5.5, simulations here present the generation of multi-slip surfaces during post-failure stages. The previous study on a simple geometry slope showed that the reduction of internal friction angle ϕ has a significant influence on the slip surface, contributing also to the generation of multiple slip surfaces.

The critical condition of $RF = 1.545$ identifies the stage where the plastic strain zone allows the slipping over an internal surface, which marks the landslide initiation. With the same strategy to weaken the material strength, we test different values for RFC and RFF . If not mentioned explicitly, the end flag of simulation is the minimum average velocity lower than 0.0001 m/s and the time step is $\Delta t = 1$ s. When the failure mass is still moving, a clear velocity distinction between the mass and the stable body can be seen. We checked all the cases that the failure mass is stopped with the specific velocity threshold, even by adopting a very large time step.

The final profile of the landslide using the critical reduced parameters gives the local failure of the initial slope displayed in Figure 5.6(a). Increasing RFF makes the plastic zone closer to the observation data, as shown in Figures 5.6(b) and 5.6(d). Two cross slip surfaces are observed in Figure 5.6(d) and this can represent two different stages of the landslide. Figure 5.6(c) shows that the increment of cohesion does not change the local failure portrayed in Figure 5.6(a). It should be mentioned that the non-normalized $PEEQ$ values for the case

of Figure 5.6(c) are generally higher than the ones of Figure 5.6(a), and that also the $PEEQ$ values inside the sliding body are distributed more widely than in Figure 5.6(a). Interestingly, Figure 5.6(b) depicts a slip surface that agrees well with the slip surface of the first stage of the landslide. However, it cannot describe the whole stages of the landslide, and thus the deposit profile is not well captured.

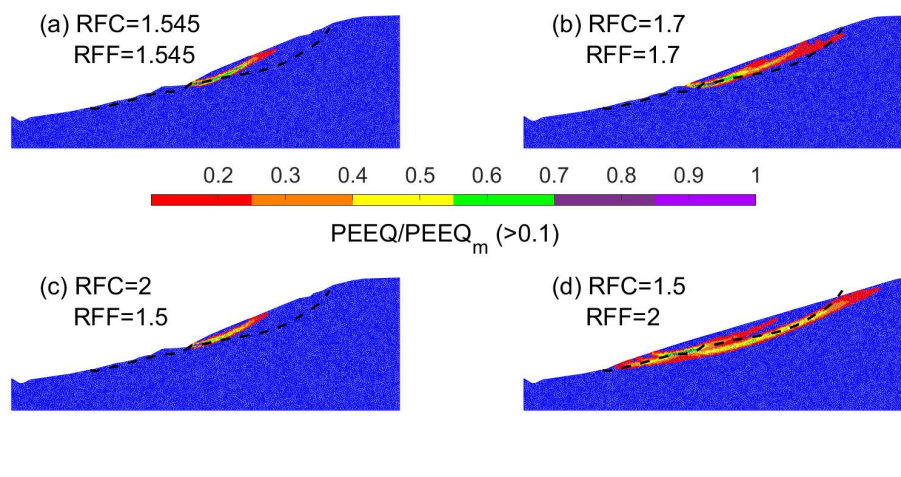


Fig. 5.6 Normalized $PEEQ$ contour with final profile of landslide for four cases.

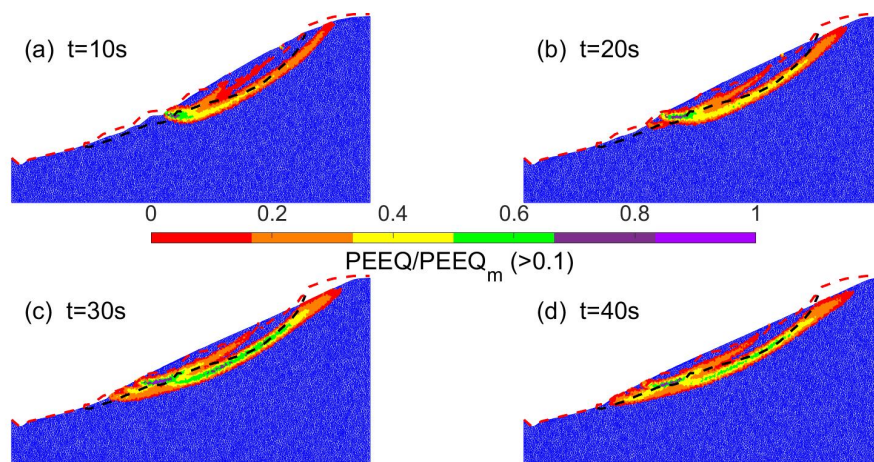


Fig. 5.7 Snapshots of $PEEQ$ with $RFC = 1.5$, $RFF = 2$.

It can be seen in Figure 5.7 that two main slip surfaces form at the beginning of the landslide evolution. With different sliding velocities, different slide bodies are observed in

(b), (c) and (d). Red and black dashed lines represent the actual slope and observed slip surface. The landslide is nearly stopped with $t = 40$ s. Simulations with various RFF and RFC values are also conducted to investigate the dynamic mechanism of landslide evolution, and the maximum displacement of the nodes is chosen as an evaluation index. As shown in Fig. 5.8, the landslide can have a maximum displacement over 200 meters when RFF is larger than 1.5. The slope of the isolines confirms that the landslide mobility is influenced much more by RFF than by RFC .

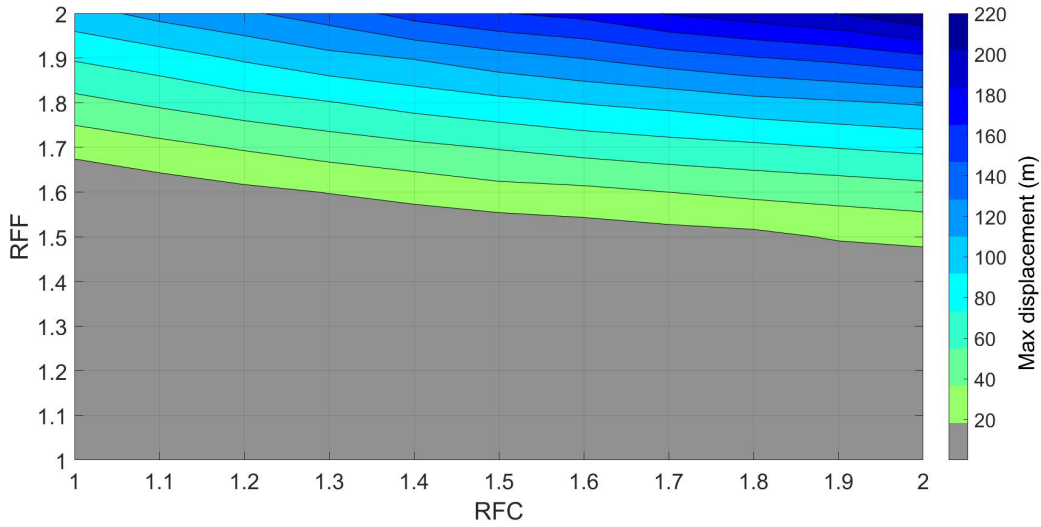


Fig. 5.8 Relationship between the maximum displacement and the reduction factors RFC and RFF . The simulations are conducted with RFC and RFF varying from 1 to 2 with equal step of 0.1.

Landslide deposit profile

With the observed data and the numerical results, the misfit index (Zaniboni and Tinti, 2014) can be calculated by means of operation on polygons. The polygons corresponding to the observed landslide deposit profile and to the numerical deposit profile are denoted as P_O and P_N . Using P_I for the polygon of the initial profile, the misfit index, designated by MI , is computed through the formula:

$$\Delta P_O = P_O \cup P_I - P_O \cap P_I \quad (5.1)$$

$$\Delta P_N = P_N \cup P_I - P_N \cap P_I \quad (5.2)$$

$$MI = 1 - \frac{\Delta P_O \cap \Delta P_N}{\Delta P_O \cup \Delta P_N} \quad (5.3)$$

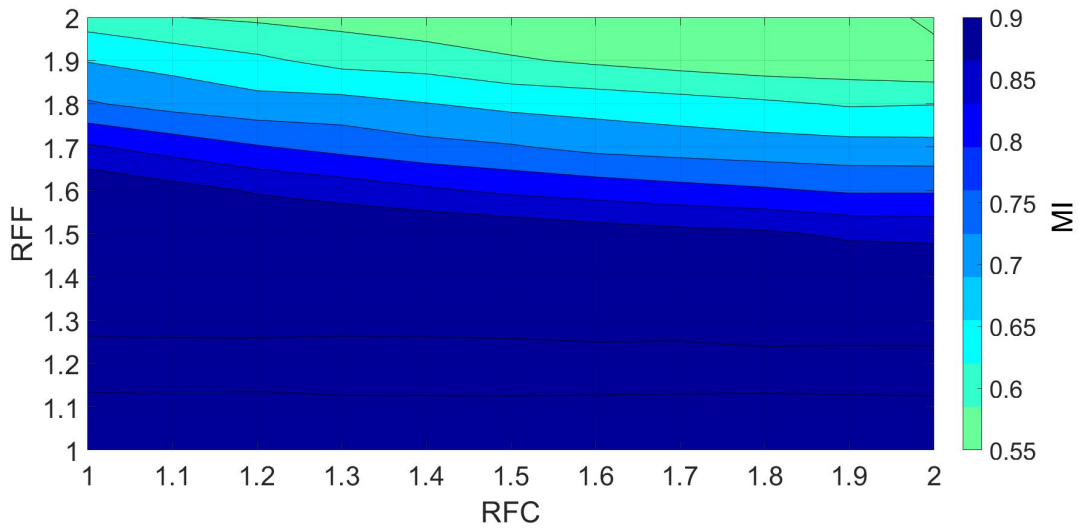


Fig. 5.9 Relationship between the MI and the reduction factors RFC and RFF that are varied from 1 to 2 with equal interval of 0.1.

According to Figure 5.9, the most similar numerical deposit profile might appear when the MI takes the smallest value. Considering that the values are quite close, we choose the four smallest values of MI and plot the corresponding results in Figure 5.10. The run-out distance is well reproduced in the case (a), (c) and (d), while the case (b) indicates that with the value $RFF = 1.9$ one might obtain a slip surface more in agreement with the observation data.

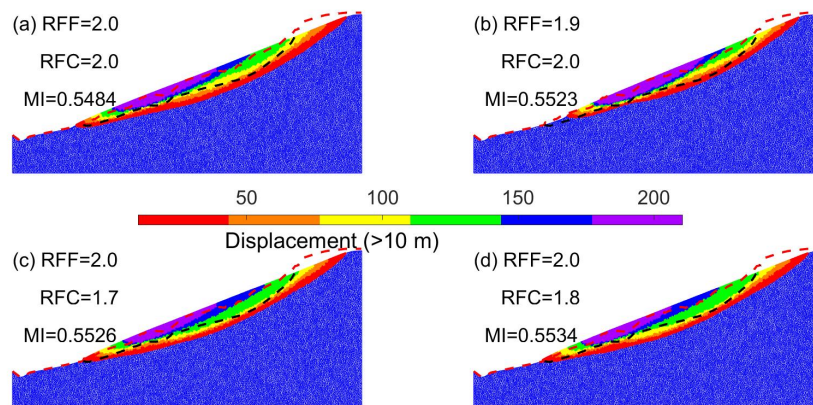


Fig. 5.10 Final deposit profile with four cases. Red and black dashed lines represent actual slope and observed slip surface.

The present PFEM simulation not only provides a reasonable deposit compared with the observed deposit profile, but also agrees quite well with the observed slip surface. This remarkable result indicates that: (1) the classical slope stability analysis might overestimate the strength parameters when it is applied to real landslide cases; (2) weakening process is quite important during the propagation of a landslide. Combining Figure 5.10(b), which captures the slip surface of the first stage and Figure 5.10(d), one may conclude that the observed slip surfaces and the run-out distance might be reproduced reasonably well by weakening the material parameters.

Weakening process

The previous simulations are carried out with the sudden reduction of strength parameters, where the reduction factors RFF and RFC are employed at the first dynamic time step (after the gravity balance calculations). In this section, a simple gradually increasing reduction factor law is implemented into the code to cast a light on the weakening process. In a first stage with a duration $T_1 \sim 280s$ RFF and RFC are gradually increased from 1.5 until $RFF = 1.90$ and $RFC = 1.98$. After that, the simulation remains with $RFF = 1.9$ and $RFC = 2$ until the general maximum velocity smaller than $10^{-5}m/s$ ($T_2 \sim 2900s$). The results for the first weakening process are shown in Figure 5.11(a) and 5.11(b). It can be seen that this quasi-static weakening process produces a result that is slightly different than the one shown in Figure 5.10(b). In Figure 5.11(a), the landslide has maximum displacement around 80 m at the front, which is smaller than in Figure 5.10(b). Further, we note that the sliding body moves with extremely low velocity along the slip surface as shown in Figure 5.11(b).

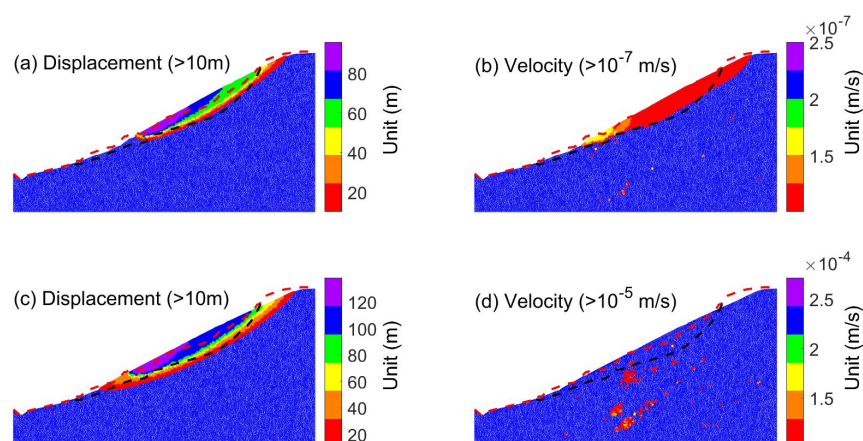


Fig. 5.11 Final deposit profile for the weakening process.

Then, in another phase of duration, $T_3 \sim 1100s$, the factors are increased to the final values $RFF = 2.0$ and $RFC = 2.0$ and the consequence is that the landslide moves at a higher velocity before reaching the final deposit profile that is a good approximation of the observed profile (see Figs. 5.11(c) and 5.11(d)). Notice that the time intervals T_1 , T_2 and T_3 have been selected with no reference to the observed time phases of the real Cà Mengoni landslide, but only with the purpose to investigate how our PFEM model performs assuming time-dependent material parameters. This experiment suggests that the evolution time of the landslide is strongly governed by the weakening process of the sliding material, and that, when it is extremely slow, like in creeping, it can be interpreted as the progressive passage through varying conditions of quasi-equilibrium. In other words, it can be seen as a quasi-static process rather than as a full dynamic process. It also suggests that more physically-based weakening models, i.e. strain-accumulated model, should be further employed to investigate further this topic, as it deserves.

The present PFEM model, that describes the dynamic deformation of a homogeneous slope that is controlled by gravity, local topography and material strength, gives results that agree well with the observed deposit profile and slip surface of the landslide when choosing appropriate reduction of internal friction angle ϕ . This finding can contribute to the risk assessment of shallow landslides, where landslide movements are controlled by deformations. We note that with the current model we have not been able to predict exactly the dynamic evolution of the Cà Mengoni landslide, as we have obtained a landslide moving much faster than it was. This is not critical, however, since slow creeping can be obtained by applying proper weakening laws. Furthermore, we point out that our model can provide more complete information on a landslide process, including the identification of the failure and influence areas, which is quite important for planning adequate mitigation strategies.

5.3 Conclusions

The accurate modelling of the entire process of landslide under a unified computational framework is a challenge for landslide studies and the significant developments of novel numerical approaches cast a light on solving this issue. To investigate and explore the capability of meshless approaches, the PFEM approach was employed in this Chapter. The present PFEM model, which combines the conventional finite element analysis and the particle-based technique, can simulate the dynamic evolution of landslides, mainly focusing on the shallow deformation of a slope.

Based on typical examples in slope stability analysis (Griffiths and Lane, 1999), we observe that under critical conditions the failure mass deposits with slight modification of the

original profile. This result indicates that there should be a further weakening process that is effective in controlling landslide propagation. Further investigations show that the reduction of internal friction angle significantly contributes to the mobility of landslides.

Applying the PFEM model to the 2013 Cà Mengoni landslide, that is a typical mass-movement event in northern Appennines, Italy, and was controlled by the homogeneous deformation of weak rocks, we found that the multi-slip surface mechanism can be accounted for by our model. Indeed, the numerical results show that the slip-surface obtained by the dynamic analysis is different from the one obtained by static analysis, since the plastic strain zones further develops during the movement of the failure mass, with a redistribution of stresses. Moreover, the model can provide a deposit profile and slip surfaces that well approximate the observed data if suitable material parameters are specified. The dynamic analysis, however, is not able to reproduce the observed duration of the process, which numerically occurs in the order of tens of seconds rather than in several hours. We have shown that the overall landslide duration can be modified by assuming simple weakening laws for the material parameters and the final landslide picture is more sensitive to the final values taken by the material parameters than to the weakening time interval. In this study, we have considered a maximum weakening time of about 4280 s instead of the observed time that was about two-day long (Berti et al., 2017), because of running time limitations. Our results show that more physically-based weakening models should be built, especially considering the effects of rainfalls on material properties, and also that, technically, the use of larger time step to reduce the computational time without affecting the physical significance of the results should be further studied.

Chapter 6

Large deformation analysis of soil slopes subjected to seismic loading

The efforts of modelling the effects of seismic loading on slopes start from the early works of limit-equilibrium methods (Terzaghi, 1950), in which seismic forces are represented as permanent body force acting on the landslides. The *FOS* can be computed by the ratio between the resistance force and the driving force terms. Soon, the method has been widely known as the pseudostatic analysis. This simple method has been used as one of the main techniques for the stability analysis of slopes in engineering during the last several decades. The choice of the coefficient is quite important for the pseudostatic analysis, and there is not a suitable physically-based criterion for choosing the coefficient. Another popular simple approach is the permanent-displacement analysis introduced by Newmark (1965). The permanent-displacement analysis is used to assess the deformation of slopes during the earthquake. The model depicts a sliding rigid block exerted by seismic forces, moving over a basal topography. Notwithstanding its simplicity in computing the permanent displacement, the model can fairly predict the deformation if slope geometry, soil properties, and earthquake motions are reasonably predefined, according to laboratory model tests and back-analysis of real cases (Goodman and Seed, 1966; Wartman et al., 2005; Wilson and Keefer, 1983).

In these two methods, the relationship between the stress and deformation is not well expressed. Therefore, mathematical models including the constitutive model relationship have been applied to the deformation of slopes solved by FDM, FEM, DEM, etc. (Jibson, 2011). Numerous efforts have been devoted to numerical analysis of seismic slopes by means of the mentioned numerical techniques. In this section, numerical investigations are performed based on the behaviour of seismic slopes involving large deformations based on the particle finite element model. It is concluded in Chapter 5 that the weakening process should be further studied during the post-failure of landslides. The capable numerical model

should describe the couple-effects of seismic shaking and material weakening. With this objective, a strain-softening model and the term of seismic forces are included into the code to investigate the behaviour of seismic slopes.

6.1 Literature reviews

The direct action on slopes by earthquakes is the stresses caused by seismic ground motion. It has been acknowledged that the dynamic response of slopes to seismic motion is controlled by factors including the excitation signal (that is the seismic wave itself), local topography, material property and discontinuities that can amplify and de-amplify signals. Step-like topographies significantly influence the dynamic response of slopes according to the early study in 1960s by Idriss and Seed (1967). A long-term (four year) monitoring system of a landslide-prone area in Italy showed that the amplification factor of shaking energy is about 2-3, apparently related to the local topography effects. The results also suggested that the directional redistribution of shaking energy is controlled by the combination of topographic and geological factors acting in similar directions (Del Gaudio and Wasowski, 2007). By means of large-scale shaking table tests, the response and amplification behaviour was also studied on a prototype slope (Lin and Wang, 2006). It was found that the dynamic response of the slope model remained linear when the loading amplitude is lower than 0.4 g and nonlinear responses were observed when acted by higher amplitude. It was also found that the failure surface of the slope is fairly shallow under such excitation. This failure mechanism is similar to the observations in some earthquake-induced landslide events. Due to the fact that observational data are difficult to obtain and that large-scale physical model test are expensive, numerical analyses have also been conducted to explore the role of different effects on slope dynamic responses. The study of seismic wave amplification also belongs to the field of seismology. Analytical solutions of the scattering of seismic waves in simple local surface topography can be found in Trifunac (1972) and Wong (1982). The use of numerical approaches is first validated against these analytical solutions. Various numerical approaches including FDM, FEM, boundary element-based methods (BEM) have been applied to computational seismology to quantify the site response. In contrast to the pure seismology analyses, the proper constitutive relationships that can address failure processes should be implemented into the stress-deformation analysis of seismic slopes. The failure of earthquake-induced landslides is controlled by the evolution of the behaviour of geomaterial during the seismic excitation. The adopted constitutive model should be able to describe the yield process of slip surface during the pre-failure and post-failure processes. The entire simulation in Chapter 5 shows that the weakening process of material can be

regarded as a significant factor contributing to the failure of landslides. Also, field surveys of historical landslide events suggest that the peak and residual shear strength should be properly incorporated into mathematical models addressing the mobilized strength.

A review of the residual shear strength in first-time slope failures in real cases is provided by Mesri and Shahien (2003). The paper reanalyses 99 historical events of slope failures and it is found that the slip surface of many first-time slope failures is at residual condition, which indicates that the weakening process exists during the stage transiting from initiation to deposition. After the first-time global slope failure, the material along the slip surface might be fully softened or at residual condition. The reduction of material from peak strength to residual strength usually is represented by the function of plasticity index. The interpretation of this strength drop can be attributed to the random arrangement of particles along the yield surface. Due to the complex dynamic behaviours of soils in various conditions and the difficulties in obtaining in-site experimental data, the constitutive models that can describe this strain-softening behaviour of soils are implemented with emphasis on the qualitative analysis of slope deformations.

It is known that this drop of material from peak strength to residual strength can cause the progressive failure of landslides, and a landslide occurred at Senise (Southern Italy), 1986 was analysed by Troncone (2005) to address the role of strain-softening behaviour. The finite element analysis associated with an elasto-viscoplastic Mohr-Coulomb model was adopted to simulate the material behaviour by reducing the strength with the accumulated deviatoric plastic strains. Based on the numerical analyses, the landslide evolution was controlled by the strain-softening behaviour of soils after the triggering by excavation activities. The variation of shear strength, i.e. cohesion and internal friction angle, follows the bilinear form proposed by Potts et al. (1990). However, it has to be pointed out that the large deformation process of the landslide could not be reproduced due to the limitation of the traditional FEM analysis. Naturally, the large deformation analysis of soils involving strain-softening behaviours can be conducted by the aforementioned advanced numerical techniques using proper strain-softening models.

A large deformation finite-element modelling of progressive failure of sensitive clay slopes was carried out by Dey et al. (2015), where the coupled Eulerian-Lagrangian (CEL) approach is performed using Abaqus software. After the erosion of a block located at the toe of the conceptual slope model, the soil mass moves with the shear strength degradation following an exponential function. The evolution of shear band inside landslide body was clearly described by the approach. Further, the Material Point Method (MPM) analysis of the large deformation of a similar conceptual slope model triggered by excavation was performed by Wang et al. (2016). Later, a detailed investigation of the role of clay sensitivity in the

evolution of progressive and retrogressive failure of landslides was conducted through PFEM by Zhang et al. (2017).

With the successes of the strain-softening models in describing the progressive failure of landslides, the effects of seismic shaking have also been incorporated into the numerical models to analyse the large deformation analysis of soil slopes. A very recent work is presented by Islam et al. (2018) with emphasis on the couple effect of strain-softening and seismic excitation. The research was carried out to investigate the large deformation of landslides in sensitive clays based on four conceptual models using the software Abaqus. The soil was modelled in a coupled Eulerian and Lagrangian procedure, where a Eulerian step follows the calculation of the traditional Lagrangian step. The information obtained from Lagrangian analysis has to be mapped back to the fixed Eulerian mesh, and the Eulerian analysis naturally avoids the mesh distortion. Seismic excitation was implemented into the simulations as horizontal acceleration time history curves along the bottom. The degradation of soil strength was expressed through an exponential function of accumulated plastic shear displacement. Von Mises yield criterion was adopted with two segments of cohesion weakening, where remoulded undrained shear strength and large-displacement undrained shear strength are reduced according to the magnitude of the accumulated plastic displacement. The performed simulations successfully captured some types of seismic slope failure (e.g. spread, flowslide or monolithic) as observed in field.

6.2 The aim of this work

It has been numerically investigated by the aforementioned works that the strain-softening process of material significant contribute to the evolution of landslides via different numerical techniques. Coupled with the long-term seismic excitation (more than 18s), the large deformation of landslides have been performed by Islam et al. (2018). However, there are still several aspects to analyse for a complete study of large deformations of seismic slopes. Indeed, it is still challenging to qualitatively describe the process by means of which the seismically induced stress triggers the failure of slopes through numerical analysis. One of the difficulties for the implementation of the seismic wave propagation is the large computational cost. The accurate description of landslides involving large deformation requires a high resolution of the numerical scheme (e.g. high-quality mesh), which is usually expensive for seismic wave propagation. Due to this limitation, the designed conceptual landslide model for large deformation analyses is generally of depth no more than 100 m. The incident seismic wave field will be very hard to describe due to the existence of free topography and imperfect absorbing property of dynamic boundary conditions. Therefore, a natural alternative choice

is to introduce the seismic wave as a body force term following the time history of the input seismic excitation. With this technique, in the following simulations, the role of vertical seismic excitation is investigated numerically as well as the role of the magnitude of the seismic excitation.

It has been reported by Iverson (1997) that the cohesion of geomaterial after failure is usually negligible and the resistance forces mainly depend on the frictional angle and the pore water pressure. The sensitive analysis of strength parameter in Chapter 5 also shows that the friction effects significantly contribute to the run-out distance of landslides. The importance of friction-weakening law was early studied in the field of dynamic rupture of faults, where the relationships between slip rate and other state variables was explored (Dieterich, 1979). Therefore, the friction coefficient on the sliding surface can be updated with those state variables. Based on the observations and numerical reconstructions of catastrophic landslide events, it was found that the postulated friction coefficient can vary from $\mu = 0.7 - 0.8$ for small volumes at low velocities to $\mu = 0.1$ for large volumes at high speed. Correspondingly, a velocity-weakening friction law was proposed by Lucas et al. (2014) to account for these effects.. However, it has to be mentioned that the friction- weakening law is currently implemented with emphasis on the post-failure stage of landslides (Borykov et al., 2019). So, another goal of this section is to numerically investigate the role of the friction-weakening process in landslide dynamics via the PFEM model.

The PFEM model presented in Chapter 3 is adopted here with the modified strain-softening model. To account for the introduced seismic forces, the gravity acceleration should be modified. When the horizontal acceleration is considered, the horizontal acceleration is set equal to the input excitation signals. When the vertical and horizontal seismic motion are both included, the input vertical motion should also be added to the gravity acceleration term. It can be implemented by modifying the body force term in Eq. (3.12). To describe the strain-softening behaviour, the similar degradation model reducing material strength by plastic index is included. In this section, the plastic index is chosen as the deviatoric plastic strain.

6.3 Clay model configuration

Similar to the Slope-I model in Islam et al. (2018), a three-layer model with flat crest is selected in our simulations. The geometry is illustrated in Fig. 6.1 with discretized elements. The soil below the blue dashed line is set as the rigid base and the soil between blue and red dashed lines is stiff clay. The material strength of the stiff clay is constant during the simulation. The soil above the blue dashed line is sensitive clay, where the cohesion varies

with the plastic index, i.e. deviatoric plastic strain. The input seismic motion is chosen from two records: 1940 El Centro and 1985 Nahanni earthquakes, which can be found in COSMOS virtual data centre (Archuleta et al., 2006). A simple linear reduction law for material strength is adopted in our simulations. For the clay slope model here, the internal friction angle is set to zero. For stiff clay, the cohesion at the crest is set as $c_0 = 25kPa$, and the cohesion increases along the depth d by the linear relationship $c = c_0 + 2d$. The depth d is computed from the crest of the slope model. For stiff clay, the cohesion is not changed during the simulation, while for sensitive clay, it is reduced by the linear form shown in Fig. 6.3. $c_{r1} = c_0/3, k_1 = 5e - 4$ and $c_{r2} = c_0/16, k_2 = 1e - 2$.

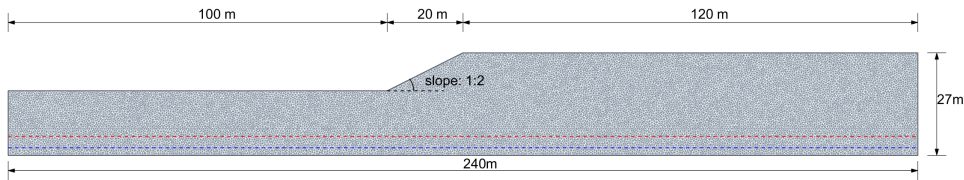


Fig. 6.1 Model of clay slope

Preliminary study on mesh sensitivity has been carried out to ensure the accuracy of the present numerical simulations. It has been investigated by Zhang et al. (2017), the mesh plays a role in the description of shear bands, while no significant effects are found on landslide dynamics and run-out distances by means of our model. To capture the landslide process including the evolution of shear bands in high resolution, i.e., dense mesh, is required, as illustrated in Fig. 6.1, where 33639 elements are used. Lateral and bottom boundaries are set as fixed.

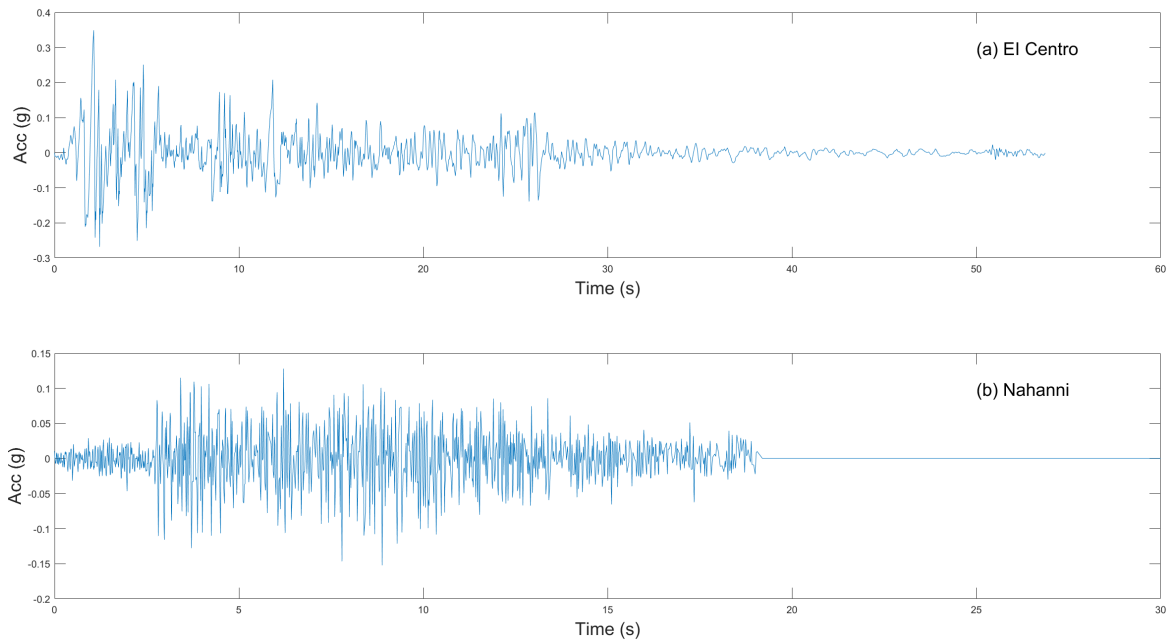


Fig. 6.2 Input signals

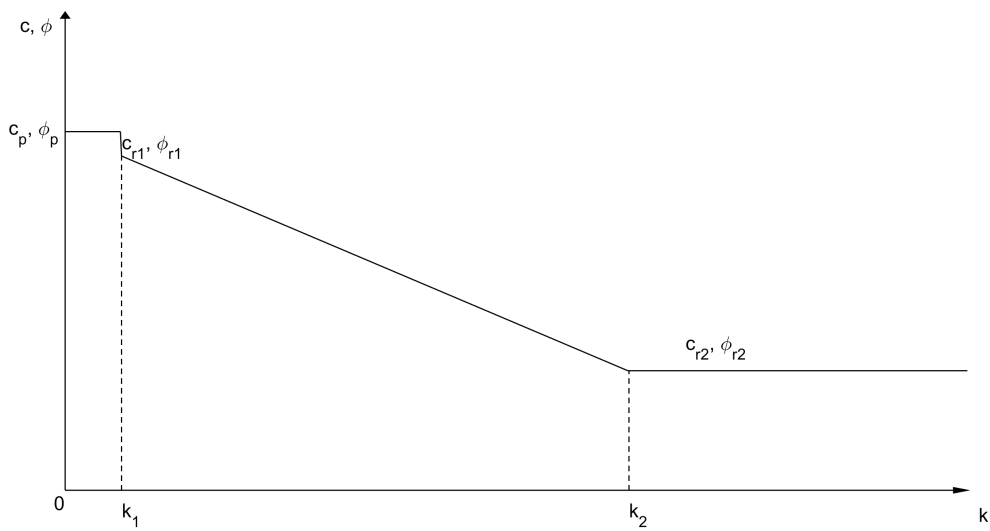


Fig. 6.3 Material-softening law

6.3.1 Onset and failure Mechanism

The Nahanni seismic signal shown in Fig. 6.2(b) multiplied by a scale factor that equals to 2 is implemented into the simulation. In this part, we restrict the research on the onset and failure mechanism of the landslides. It has been studied that the strain-weakening behaviour can induce the progressive failure of landslides with large run-out distance(e.g., Zhang et al., 2017). The relationships between seismic motion/material strength with run-out distance will not be fully studied, and we mainly investigate the onset-failure process via the PFEM model. The excitation lasts 7 seconds, as illustrated in Fig. 6.4. The external horizontal body force term is included to represent the horizontal seismic motion.

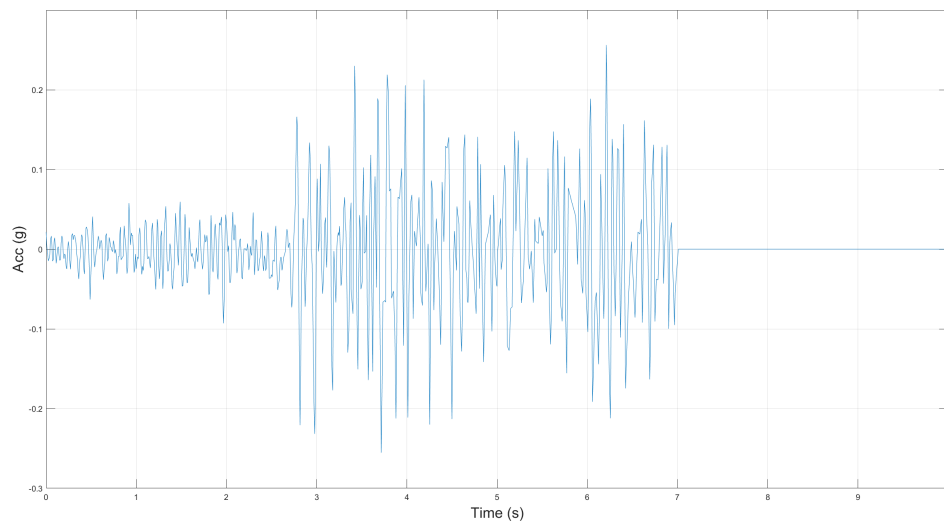


Fig. 6.4 Input seismic signal with 7s lasting excitation.

To study the evolution of the process from onset to motion, we first study the evolution of displacement of the sliding body. The displacement of two directions at different moments are extracted to interpret the landslide dynamics. x direction displacement of the landslide at 2 s, 4 s, 6 s, 8 s, 10 s, 12 s, 14 s, and 16 s can be found in Fig. 6.5 and Fig. 6.6, where the initiation and propagation are well captured. horizontal body force term is included to represent the horizontal seismic motion.

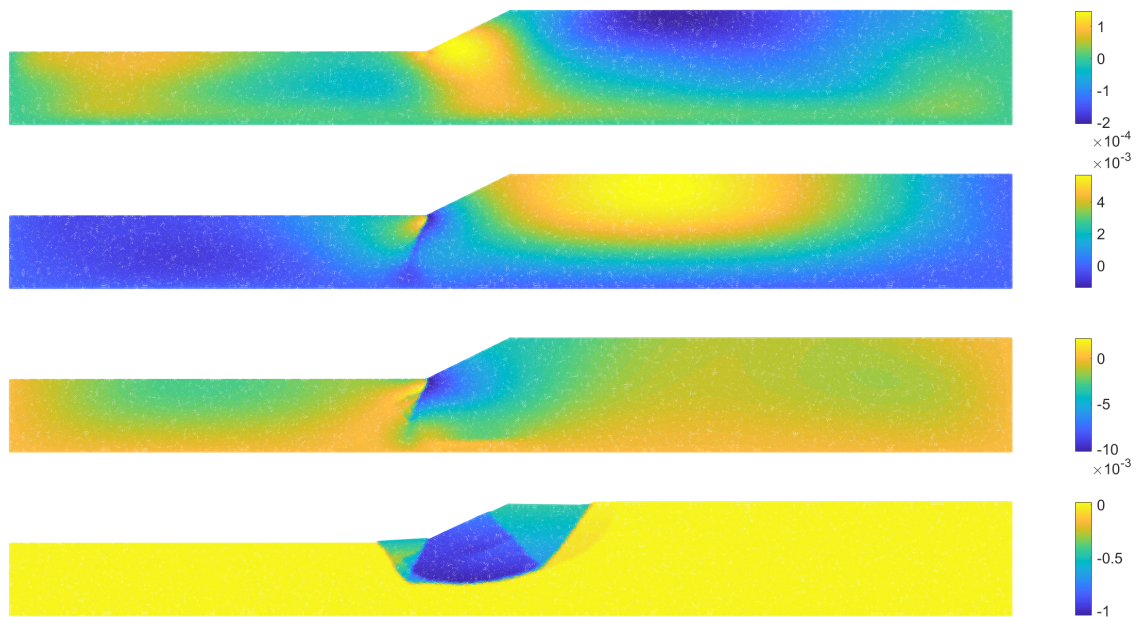


Fig. 6.5 Horizontal displacement of the landslide at four instants: 2 s, 4 s, 6 s, 8 s. (Unit: m)

According to Fig. 6.5, it is found that the failure of the landslide can be attributed to the yield of the toe of the slope. For $t = 2$ s (the first plot in Fig. 6.5), the displacement is at a negligible scale (10^{-4} m). In the second plot ($t = 4$ s), it is clear that the soil at the toe starts yielding and there is a distinct line that indicates the opposite motion of the surrounding soil. The intensive strong seismic motion (see Fig. 6.4) starting from about $t = 3$ s contributes to this failure process. Then, it becomes clearer that the soil at the toe is exerted by the opposite motions of its back soil and magnitude of displacement increases by one magnitude (10^{-3} m). Later, it can be seen in the fourth plot that the slip surface is generated and an irregular sliding body is extruded to the ground with a large horizontal displacement exceeding 1 m. Also, the simulation depicts that the landslide moves with several different blocks, which can be recognized from blocks with different colours (four blocks in the fourth plot). The displacement of the thin yellow block behind the green one is at low values and this block will move after the movement of the front of the landslide.



Fig. 6.6 Horizontal displacement of the landslide at four instants: 10 s, 12 s, 14 s, 16 s. (Unit: m)

In the following time instants, the extreme large deformation of the landslide is involved. For $t = 10$ s, the recognized sliding body illustrated by $t = 8$ s in Fig. 6.5 has a displacement of 1 m. The blocks interact together and induce the surface deformation on the sliding body. With high velocities, the blocks rapidly with large displacement as shown in the moments $t = 12$ s and $t = 14$ s. For $t = 16$ s, it is found that a circle slip surface on the crest is generated by the movements of the landslide.



Fig. 6.7 Vertical displacement of the landslide at four instants: 2 s, 4 s, 6 s, 8 s. (Unit: m)

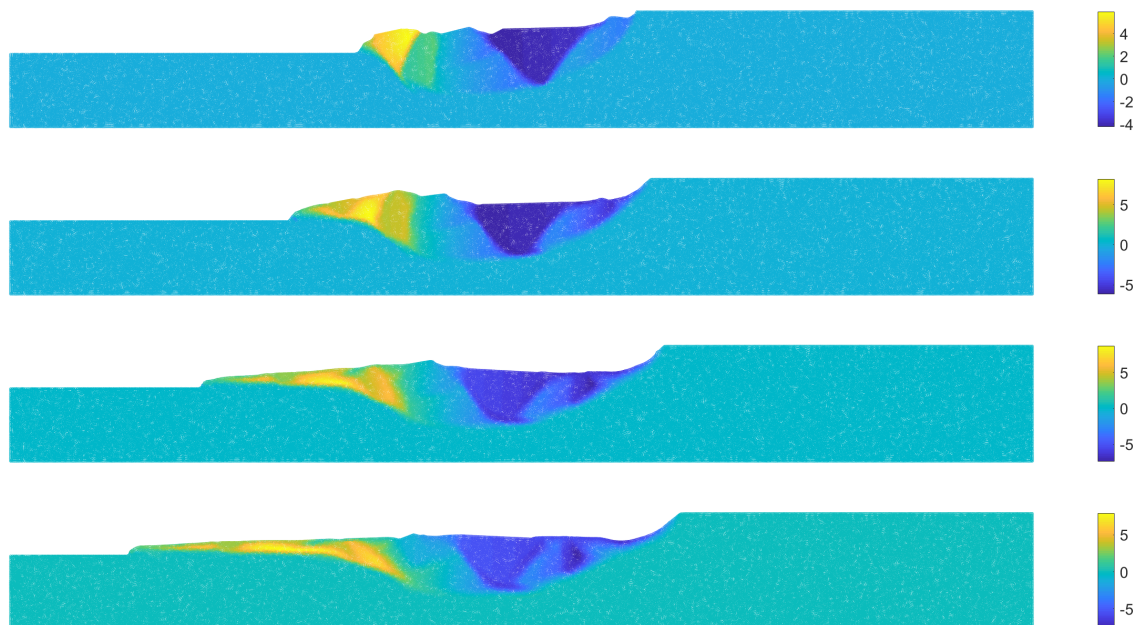


Fig. 6.8 Vertical displacement of the landslide at four instants: 10 s, 12 s, 14 s, 16 s. (Unit: m)

The landslide dynamics is depicted in Fig. 6.7 and Fig. 6.8, where the front and the rear of the landslide experiences an upward and a downward motion respectively. It is clear in $t = 4s$ and $t = 6s$ that, the lasting of seismic motion significantly contributes to uplift of the toe and then induces the failure. The landslide dynamics can be also represented by the evolution of velocity information as shown in Fig. 6.9 and Fig. 6.10. It can be seen in Fig. 6.9 that the deformation of the slope mainly comes from the subsidence on the crest until the generation of the slip surface (see Fig. 6.12). The velocity of front the sliding body at $t = 8s$ is 2 m/s and then increases to 10 m/s at $t = 14s$ (see Fig. 6.10). The induced retrogressive failure has been well captured in Fig. 6.10 by the velocity discontinuities between the front and the rear of the sliding body. The evolution of the plastic zone (shear band) can be observed by the Fig. 6.11 to Fig. 6.14 at four instants. The complete slip surface is observed at $t = 8s$ after the yield of soils at the toe of the slope. Later, the plastic propagates inside the sliding body with a following failure shown in Fig. 6.13. As mentioned that we focus on the main dynamics of the landslide from failure to motion, so the full simulation of the whole process is not presented here for simplicity.

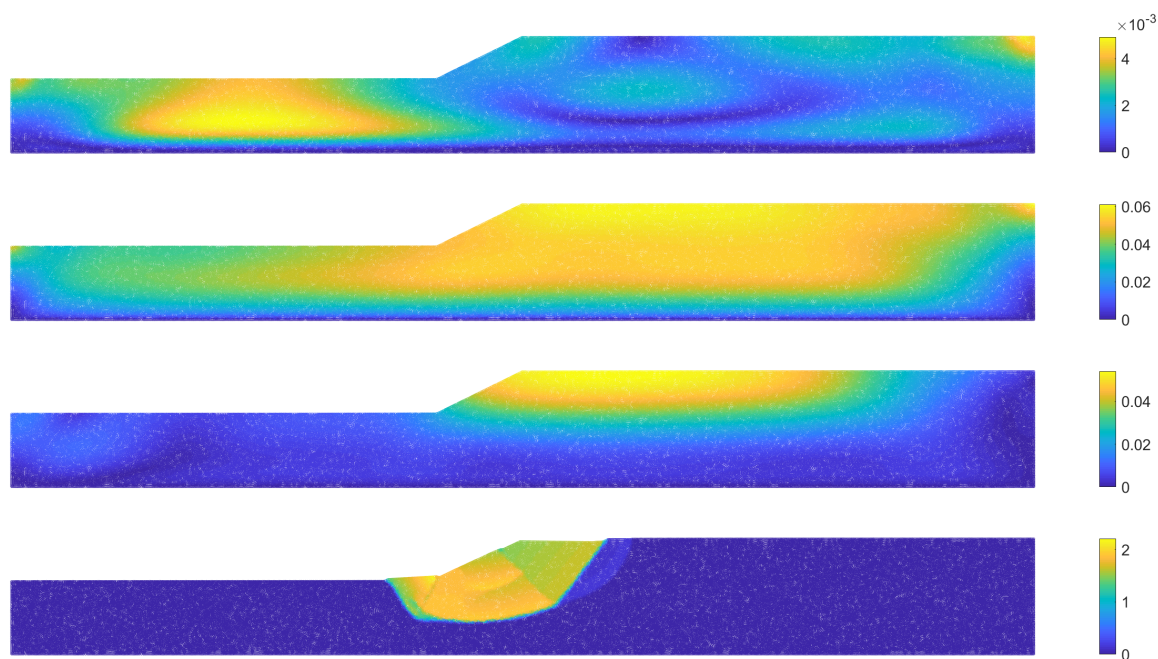


Fig. 6.9 Velocity magnitude of the landslide at four instants: 2 s, 4 s, 6 s, 8 s. (Unit: m/s)

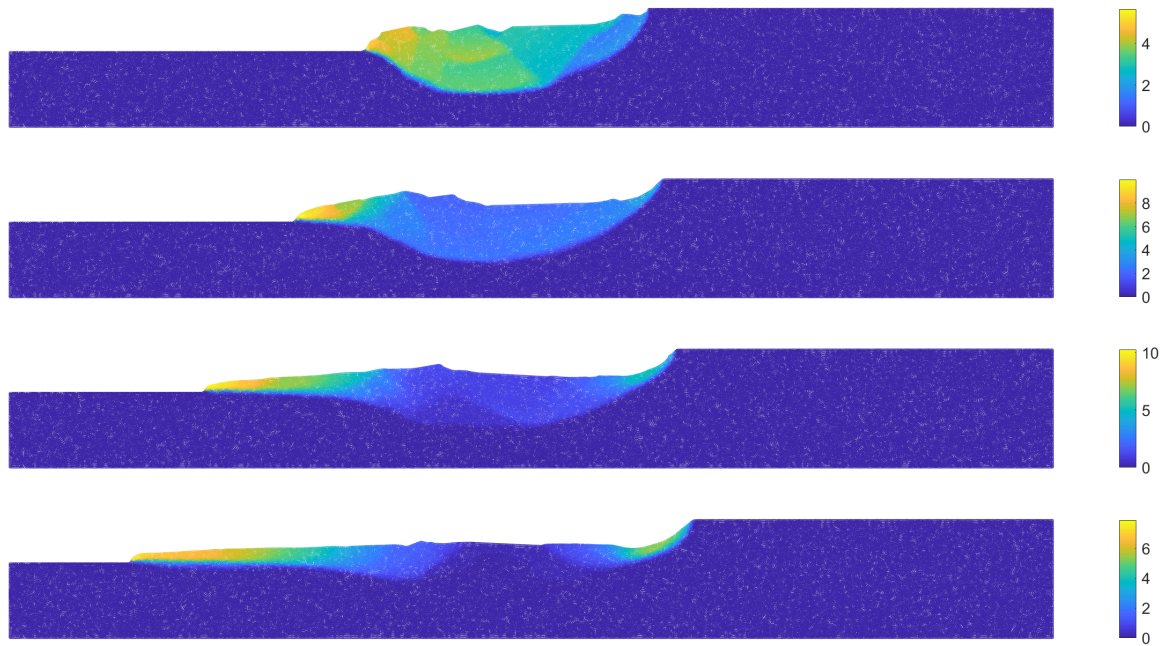


Fig. 6.10 Velocity magnitude of the landslide at four instants: 10 s, 12 s, 14 s, 16 s. (Unit: m/s)

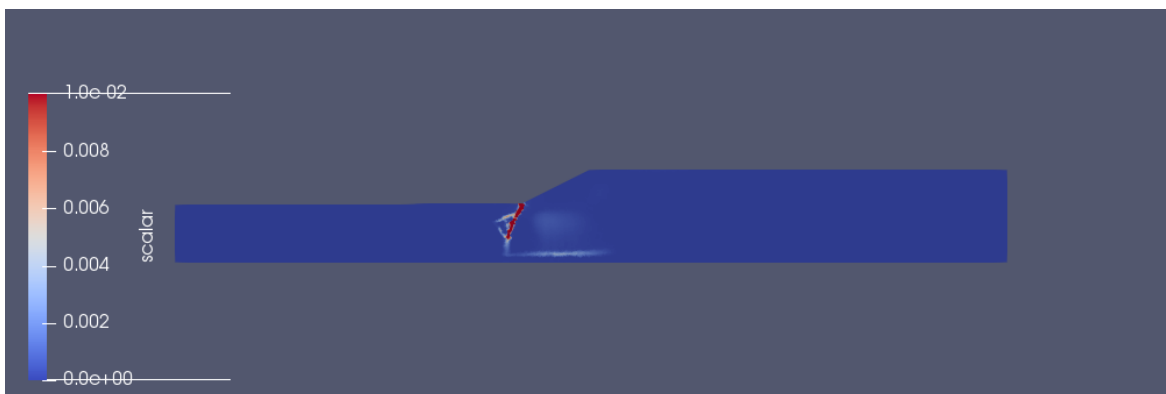
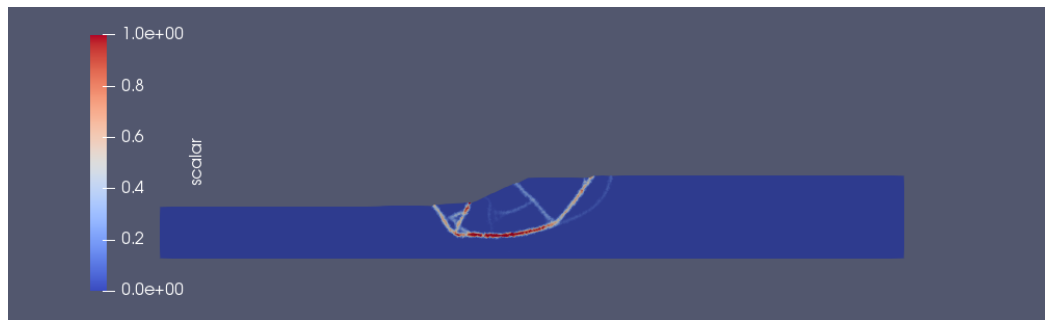
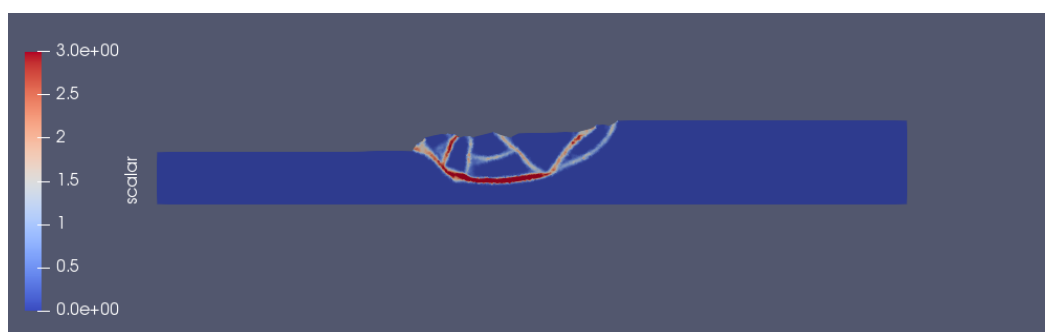
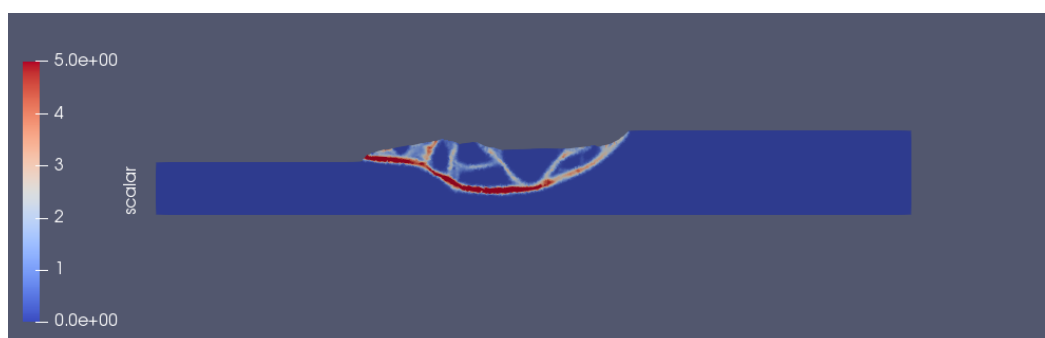


Fig. 6.11 Equivalent plastic strain at $t = 6s$.

Fig. 6.12 Equivalent plastic strain at $t = 8s$.Fig. 6.13 Equivalent plastic strain at $t = 10s$.Fig. 6.14 Equivalent plastic strain at $t = 12s$.

Overall, the dynamics of such a landslide of clay subjected to seismic loading can be summarized as: (1) The failure of soils at the toe; (2) The propagation of plastic strain that generate the slip surface; (3) The included retrogressive failure induced by the landslide motion. It is obvious that the weakening of the soils significantly contributes the propagation of shear bands.

6.3.2 Influence of weakening parameter

The residual strength is changed as $c_{r2} = c_0/10$ in this part and the seismic signal shown in Fig. 6.4 is changed with a factor 0.75 and 1.25 respectively. The corresponding slope models are denoted as Slope-I and Slope-II respectively. The influence of weakening parameters on the failure mechanism is studied by the comparison between slip surfaces. The velocity of the landslide at five instants from $t = 2$ s to $t = 10$ s with interval of 2 s are displayed in Fig. 6.15 and Fig. 6.16 respectively.

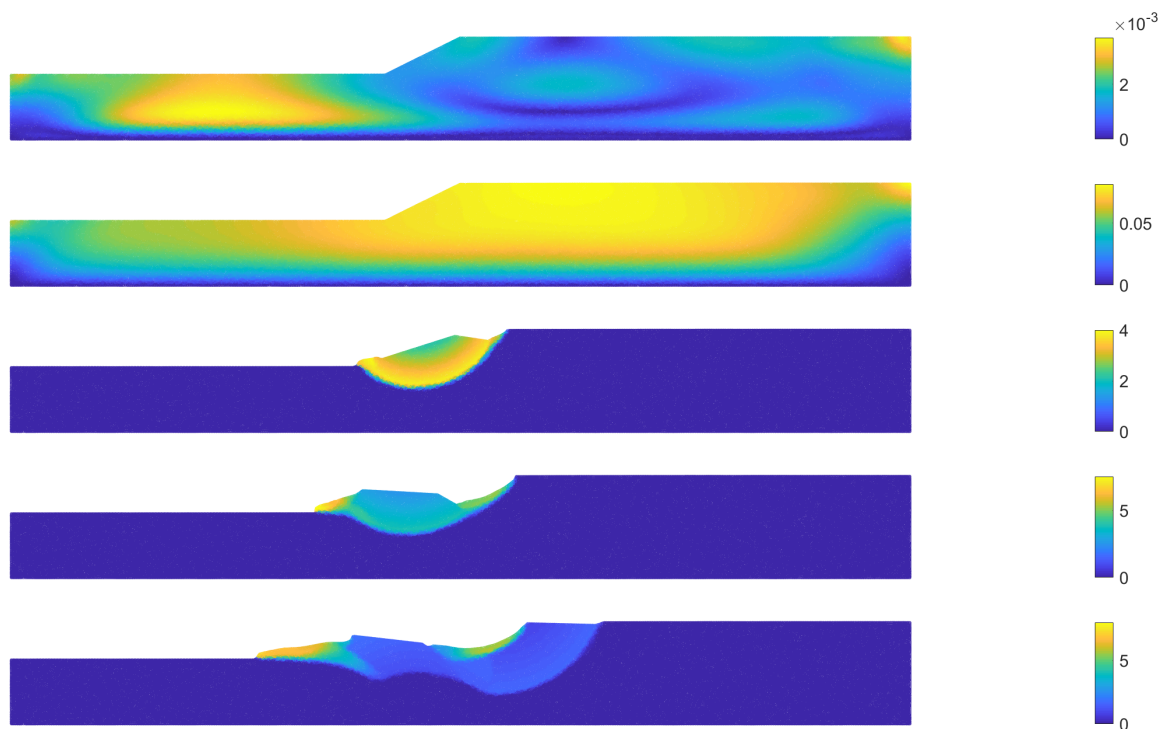


Fig. 6.15 Velocity profiles of Slope-I at five moments from $t = 2$ s to $t = 10$ s with interval of 2 s, Unit: m/s .

In contrast to the irregular slip surface shown in section 6.4.1, clear circle slip surfaces are observed by our approach under two different situations. This can be attributed to the change of c_{r2} , and the failure process is influenced by the weakening parameters. It has been investigated by Yerro et al. (2016) that the residual strength of material controls the post-failure behaviour of the landslide. Instead, it is found by the present model that the residual strength also plays a role in the generation of the slip surface during the seismic excitation.

According to the comparison between Fig. 6.15 and Fig. 6.16, the slope failure occurs earlier when exerted by a larger excitation. As shown in Fig. 6.15, the recognized sliding

body of Slope-I is larger than the one of Slope-II in Fig. 6.16. The seismic motion lasts 7 s, and the slip surface of Slope-II has been already generated at $t = 4$ s. After this time the intensive bilateral excitation restricts the propagation of the failure. For the case of Slope-I, the slip surface generates after the intensive seismic excitation phase and the failure propagates with less influence from the seismic motion. So far, the seismic wave propagation between the sliding body and the stable body cannot be accurately described by the current techniques due to the variation of geometry and material. The seismic motion is implemented in a simple manner and it can be further studied with more advanced ways.

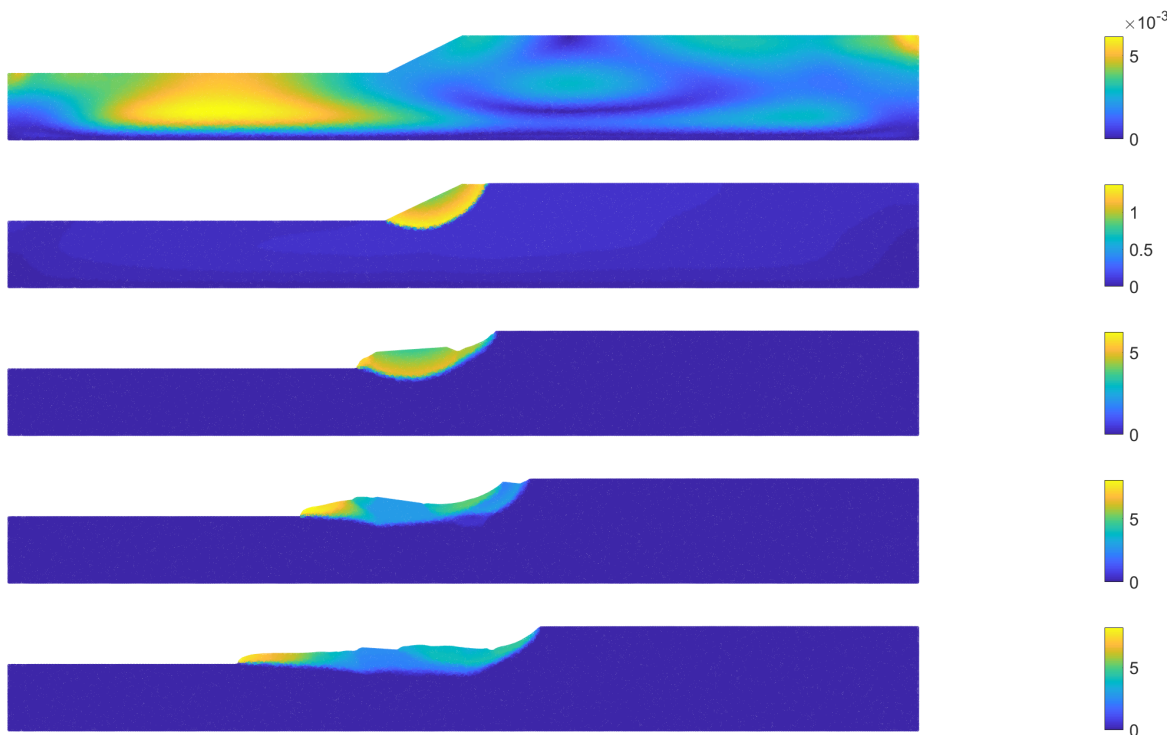


Fig. 6.16 Velocity profiles of Slope-II at five moments from $t = 2$ s to $t = 10$ s with interval of 2 s, Unit: m/s .

6.3.3 Vertical loading

The characteristics of lateral seismic motion have been extensively studied in the seismic slope stability, and the importance of vertical motion in earth structures has been noticed after the devastating Kanto Earthquake in Japan (Ling et al., 1997). For practical seismic design of structures, seismic coefficient should be determined by the maximum peak acceleration of the considered earthquake. In the limit equilibrium method, the influences of seismic motion are introduced by two acceleration coefficients. According to earthquake records,

peak value of vertical acceleration approximates to the range of 1/2 to 1/3 of peak horizontal acceleration (Wiegel, 1970). Therefore, two body terms including the horizontal and the vertical loading are implemented into the model to trigger the failure of the clay slope.

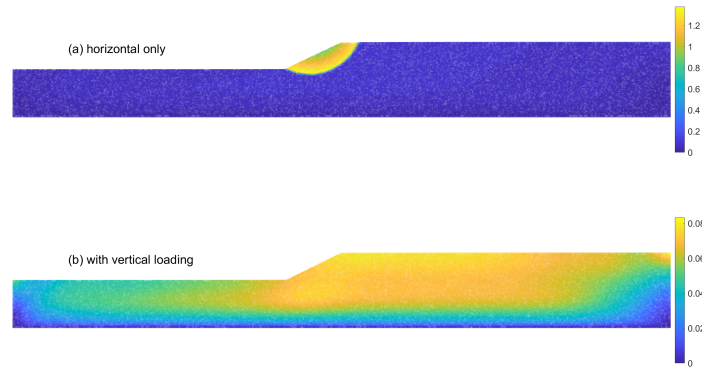


Fig. 6.17 Velocity profiles of Slope-II at $t = 4$ s excited by (a) horizontal and (b) two-direction loading, unit: m/s .



Fig. 6.18 Velocity profiles of Slope-II at $t = 5$ s excited by (a) horizontal and (b) two-direction loading, unit: m/s .

As displayed by Fig. 6.17 and Fig. 6.18 that the inclusion of vertical loading has an influence on the onset mechanism of the landslide. With the vertical loading, the slope failure happens later than the one only excited by horizontal loading due to two reasons. One is that the directional change of the vertical loading can reduce the gravity effects, since upward and downward accelerations are involved. The other reason can be seen from the comparison between slip surfaces, i.e. (a) in Fig. 6.17 and (b) in Fig. 6.18. The slip surface induced by seismic motion involving vertical loading is deeper than the one triggered by pure horizontal loading. It is obvious that the generation of deeper failure experiences larger impeding forces coming from the base. It should be mentioned that the onset velocity of the landslide shown

in Fig. 6.18(b) is larger than that in Fig. 6.17(a). Also, the slip surface in Fig. 6.18(b) is more irregular compared with the slip surface obtained in Fig. 6.17(a).



Fig. 6.19 Equivalent plastic strain evolution of Slope-II excited by two-direction loading from $t = 4s$ to $t = 6.5s$ with interval of $\Delta t = 0.5s$.

The onset mechanism tracked by the evolution of equivalent plastic strain is presented in Fig. 6.19. The toe of the slope first yields and leads to generation of slip surfaces where three blocks are involved (see Fig. 6.19(b)). After that, the shear band propagates inside the sliding body and the onset mechanism is quite similar in all simulations. In addition to the retrogressive failure on the crest, a clear slip surface under the front of the landslide is also observed during the motion of the landslide (see Fig. 6.20 (c)). It should be mentioned that the seismic excitation ends after $t = 7s$ (see Fig. 6.4). The velocity profiles of the slope after slope failure are presented in Fig. 6.21. The alphabetical order from (a) to (e) indicates the results obtained from the model only excited by horizontal motion. The Roman numeral represents the model considering vertical loading. It is clear that the magnitude of the sliding velocity is quite close, and the deeper sliding zone contributes to the generation of new slip surfaces. As can be seen, the retrogressive failure shown in (b-c) is smaller than the one in (III-IV). The deeper failure disturbs the situation of the sensitive clay and generates a new slip surface under the front of the landslide.

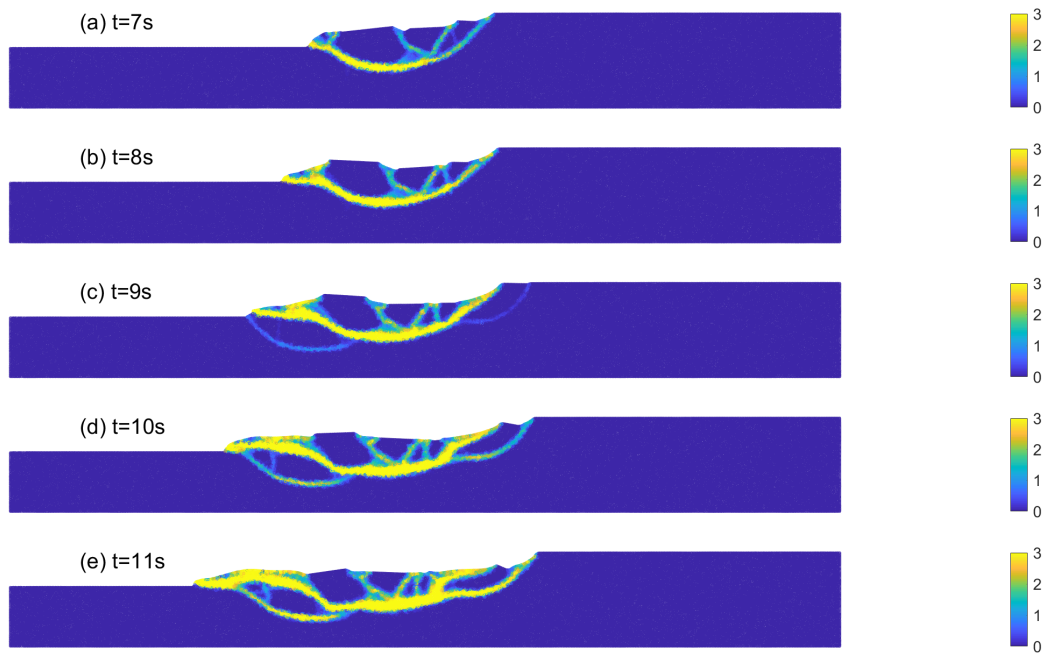


Fig. 6.20 Equivalent plastic strain evolution of Slope-II excited by two-direction loading at different instants. Slip surfaces are highlighted by adopting a fixed colorbar.

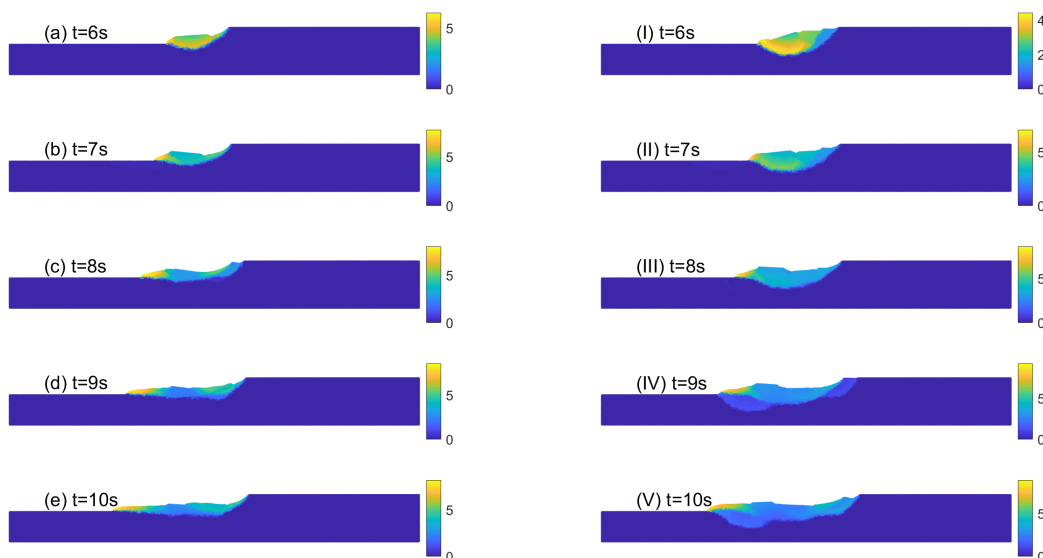


Fig. 6.21 Comparison between velocity profile of Slope-II after the onset of landslide.

6.4 Frictional effects

In this part, the resistance of internal friction angle is also included into the model. The non-associated Mohr-Coulomb model is used and the dilation angle is set to zero. The concept landslide model shown in Fig. 6.1 is still used here with the internal friction angle equal to 10° . Correspondingly, the reduction parameters for the soil are changed as $c_{r1} = 2.5$ and $C_{r2} = 5$, since the upper layer is not high sensitive clay when considering internal frictional effects. The consideration of amplitude is included by using two amplification factor of the seismic signal shown in Fig. 6.2 (b). The excitation signals treated as horizontal acceleration are displayed at the bottom of Fig 6.22. The velocity profiles of the landslide at five instants are presented in Fig 6.22 corresponding to the applied loading curve below each of them. With a larger amplitude, the slip surface generates earlier (see (III) $t = 3.5$ s) than the one in Fig 6.22(e) ($t = 4.5$ s). The generated slip surfaces are similar to each other and the onset velocity of sliding body is about 0.5 m/s, mainly controlled by the configuration of material (compared with the velocity in clay soils).

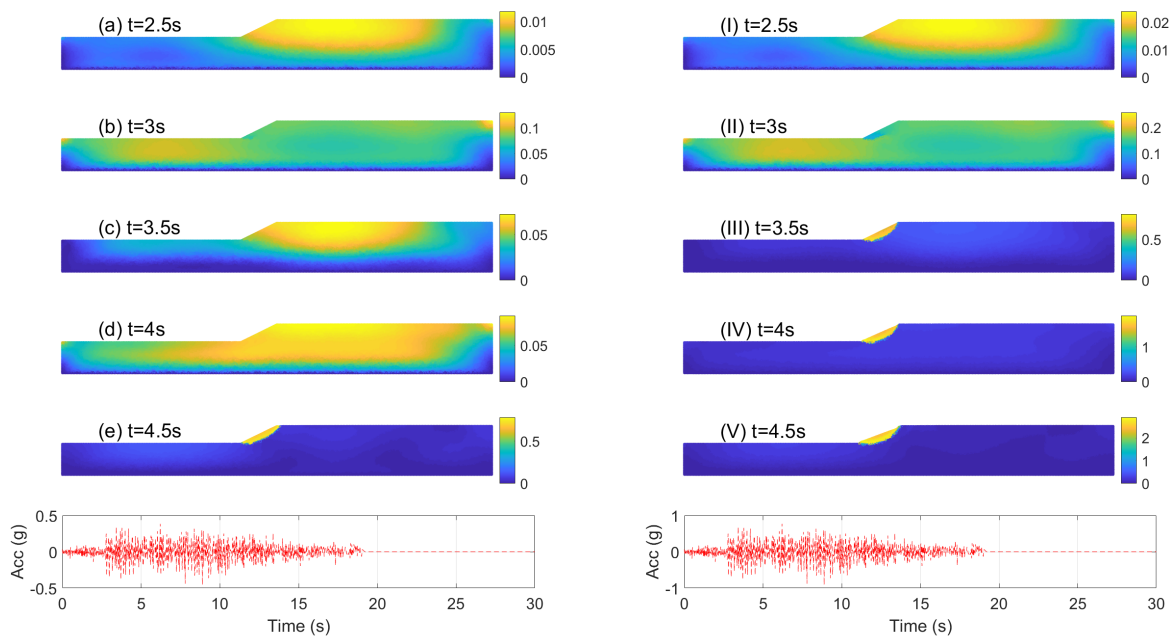


Fig. 6.22 Velocity profiles of the landslide under different excitation amplitude at chosen instants.

The landslide dynamics after-failure can also be captured via the evolution of velocity. The dynamics of the landslide under the two amplitude signals is similar and only the one with higher amplitude is presented in Fig. 6.23. The sliding body moves with a maximum velocity near 4 m/s at $t = 7.5$ s (see Fig 6.23 (d)) and gradually decelerates to maximum

velocity of 1 m/s. It is clear that the front of the landslide approximates to still at $t = 15$ s even though the rear is still moving. The landslide moves mainly based on the initial failure generated at $t = 3.5$ s (see Fig 6.22 (III)) in the form of a shallow movement. Therefore we can see that the inclusion of the internal friction angle significantly affects the whole landslide process since it plays a crucial role in resistance forces.

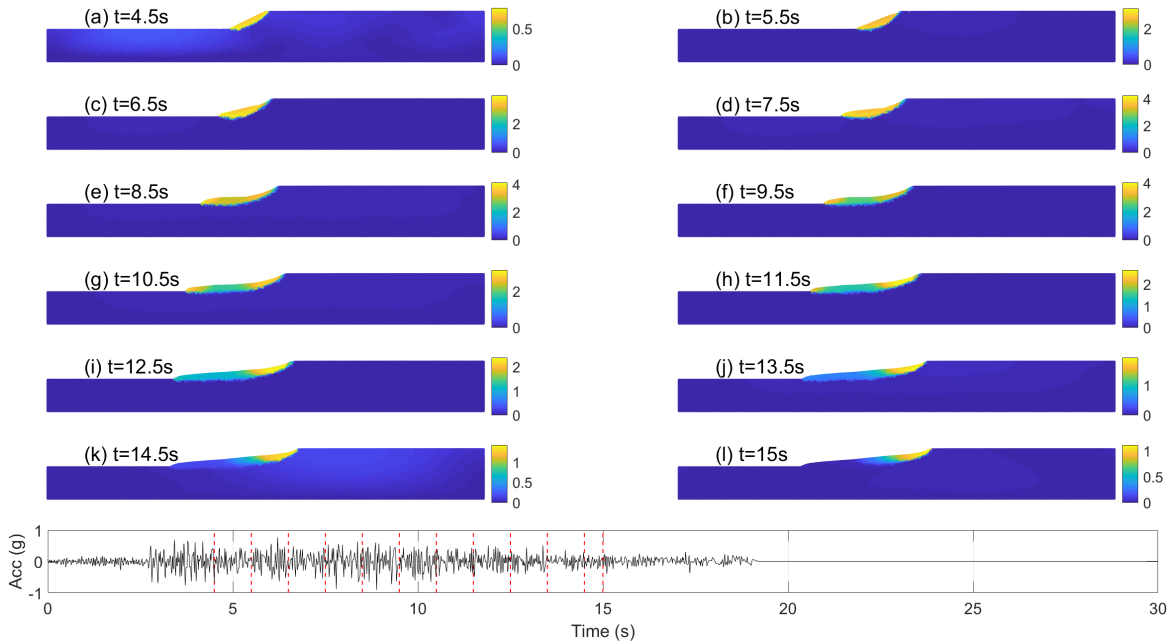


Fig. 6.23 Velocity evolution of the landslide with higher amplitude.

Chapter 7

Conclusions and Outlook

The main work of this thesis has been devoted to the development of numerical tools applied to the entire simulation of landslides including the modelling of pre- and post-failure analysis of landslides. To this end, the optimization-based Particle Finite Element Method (PFEM) has been chosen as the tool to investigate the dynamics of landslides. Additionally, an FDM code based on depth-averaged equations (DAEs) has been developed to allow the comparison between the PFEM model and the DAEs applied to the run-out process of landslides. The present PFEM model can serve for the modelling of landslides and further can be developed to include more features. The contributions of the present work are summarized as follows:

- Numerical details of the DAEs code have been presented and the developed code can be applied to the family of DAEs. Based on a model proposed by Xia and Liang (2018), the DAEs code has successfully captured the deposit profile of the 1783 Scilla landslide, Italy. Two different landslide dynamics have been studied by adopting two submarine drag laws.
- Numerical implementation of the optimization-based PFEM has been fully presented. It is a 2D PFEM code and it can be further incorporated into other geoscientific models to meet different requirements.
- The PFEM code has been applied to the modelling of landslides including the stability analysis and the run-out analysis parts. The performances of the DAEs code and the PFEM code have been compared for the analysis of landslide propagation problems.
- The PFEM code has been used to investigate the evolution of the 2013 Cà Mengoni landslide. It has been found that the weakening process dominates the dynamics of landslide from initiation to deposition.

- Preliminary studies have been conducted to investigate the performance of a strain-softening model combined with the inertial forces in modelling the dynamics of landslides subjected to seismic loading.

Based on the developed models, the landslide dynamics has been studied through experimental tests, real cases and simplified conceptual models. According to the investigations of the 1783 Scilla landslide, Italy, it has been found that the landslide dynamics captured by the depth-averaged model incorporating a linear drag relationship is similar to the one described by the quadratic-drag block model (Zaniboni et al., 2016), even though the deposit profile can be successfully captured by the model adopting two drag relationships. A historical tsunami event was generated by the 1783 Scilla landslide, further comparisons can be carried out based on a tsunami model using different landslide dynamics. A recent work has been published by Zaniboni et al. (2019), where the block model that communicates the landslide dynamics to tsunami generation model was applied to study the landslide-tsunami effects on the Calabrian and Sicilian coasts. Similar efforts can be done to compare the tsunami wave generated by a more solid-like landslide (i.e. block model) and a more fluid-like landslide (i.e. DAEs).

The DAEs and the PFEM model are compared through the modelling of landslide propagation problems: the collapse of aluminum bars (laboratory test) and the run-out of the 2008 Tangjiashan landslide, China. The simulations provide similar deposit profiles for the ‘collapse’ problems, while the velocity of the flow described by the DAEs is faster than the one depicted by PFEM model. This can be attributed to the adopted simple rheology in the present model, and further studies should be conducted by using more advanced models.

Thanks to its capability of modelling large deformation, the PFEM model has been applied to study the entire landslide process for a conceptual case and for a real case. It has been found that slopes experience a relatively small displacement without the weakening process. Therefore, one can conclude that the weakening process contributes significantly to the high mobility of some landslides. A back-analysis has been conducted via numerical investigations on the 2013 Cà Mengoni landslide, Italy. The landslide has been simulated as a homogeneous material according to previous geological surveys and numerical studies (Berti et al., 2017). By means of a simple time-dependent linear weakening law, the slip surface and run-out distance have been captured by the PFEM model. From initiation to deposition, the slope body experienced shallow variations on the surface, and this can be attributed to the response of slope geometry to material strength. However, the present simulations cannot accurately describe the velocity information of the landslide due to the lack of information about the time-dependent degradation of the material. In the future, a proper creeping law

should be included into the model to simulate a real case landslide, for which observation data are available.

Further, the dynamics of landslide subjected to seismic loading has been studied on a conceptual model. The model was presented by (Islam et al., 2018) to simplify the widely found clay slopes in Canada. To simplify the complexity of the seismic analysis of the landslide, the additional stresses caused by seismic waves have been simplified as inertial force terms following the acceleration records in the model. Also, a strain-weakening model has been included to describe the degradation of clay from peak strength to residual strength. According to the numerical simulations, it has been found that the landslide in clay is triggered after the generation of several blocks. First, the toe of the slope yields and several blocks form during the seismic excitation. After the triggering, the blocks interact with each other while moving and one can observe a progressive failure induced by the strain-weakening process. The strain-weakening model depends on the accumulated plastic strain and it has been found that the choice of the weakening parameters influences the slip surface of the clay slope. A further study has been done by considering the influence of vertical loading on the onset mechanism of the landslide. The inclusion of vertical loading increases and reduces the gravity effects and thus affects the initiation moment of the landslide. With the vertical loading, the generated slip surface is deeper than the one only excited by horizontal loading in the studied case. Considering the effects of friction, it has been found that the induced shallow slope failure moves along the ground, in contrast to the observed deep failure of the clay slope. The present simulations successfully capture some types of landslide movements, though this study is still preliminary. More systematic simulations will be carried out to separate the influence of seismic loading and strain-weakening behaviour on the large deformation analysis of seismic slopes.

Appendix A

Short guide of the developed codes

All simulations have been conducted on the PC: *Thinkpad T470p* with the processor *Intel(R) Core(TM) i7-7820HQ CPU @ 2.90GHz* and 16 GB RAM.

Depth-averaged codes

- Tool: MATLAB (for computation and Pre/Post Processing).
- Brief description: the code can be applied to the general depth-averaged models, where the new state of conservative variables are updated by the governing equations of conservative variables, flux and source terms. The flux and source terms are further updated according to the these conservative variables. Flux limiter and adaptive time step are used to ensure numerical stability.
- Consuming time (Scilla case in Chapter 2) for: Linear drag (150s simulation) took 1397.4 seconds and Quadratic drag (300s simulation) took 963.8 seconds. Physical variables were stored each 5 simulated seconds for both linear and quadratic cases.

FEM/PFEM code

- Mesh Generator: DistMesh (Persson and Strang, 2004) and Triangle (Shewchuk, 1996).
- Pre-processing & construction of optimization problem: MATLAB.
- Optimization solver: MOSEK (MOSEK, 2019) with academic license.
- Post-processing: MATLAB & Paraview (Ahrens et al., 2005).
- Brief description: The optimization problem is constructed as a *structure 'prob'* that can be identified by MOSEK, and the solutions are contained in *'res'* returned by the

MOSEK. Physical variables are extracted from 'res', and further being stored, updated and written in the format of 'vtk' that can be visualized by Paraview. The PFEM technique is written as MATLAB script and it should be called when large-deformation analysis is involved.

- Consuming time (the 2013 Cà Mengoni landslide in Chapter 5): 225.4 seconds for each step, including all the costs of Pre/Post Processing, computation and PFEM technique.

References

- Ahrens, J., Geveci, B., and Law, C. (2005). Paraview: An end-user tool for large data visualization. *The visualization handbook*, 717.
- Alizadeh, F., Haeberly, J.-P. A., and Overton, M. L. (1998). Primal-dual interior-point methods for semidefinite programming: convergence rates, stability and numerical results. *SIAM Journal on Optimization*, 8(3):746–768.
- Andersen, S. and Andersen, L. (2010). Modelling of landslides with the material-point method. *Computational Geosciences*, 14(1):137–147.
- Archuleta, R. J., Steidl, J., and Squibb, M. (2006). The COSMOS Virtual Data Center: A web portal for strong motion data dissemination. *Seismological Research Letters*, 77(6):651–658.
- Avolio, M. V., Lupiano, V., Mazzanti, P., and Di Gregorio, S. (2009). A cellular automata model for flow-like landslides with numerical simulations of subaerial and subaqueous cases. *EnviroInfo*, 1:131–140.
- Bagnold, R. A. (1954). Experiments on a gravity-free dispersion of large solid spheres in a newtonian fluid under shear. 225(1160):49–63.
- Bathe, K. and Wilson, E. (1972). Stability and accuracy analysis of direct integration methods. *Earthquake Engineering & Structural Dynamics*, 1(3):283–291.
- Bathe, K.-J. (2006). *Finite element procedures*. Prentice Hall, Pearson Education, Inc, New Jersey.
- Berti, M., Bertello, L., Bernardi, A. R., and Caputo, G. (2017). Back analysis of a large landslide in a flysch rock mass. *Landslides*, 14(6):2041–2058.
- Bishop, A. W. (1955). The use of the slip circle in the stability analysis of slopes. *Géotechnique*, 5(1):7–17.
- Borykov, T., Mège, D., Mangeney, A., Richard, P., Gurgurewicz, J., and Lucas, A. (2019). Empirical investigation of friction weakening of terrestrial and Martian landslides using discrete element models. *Landslides*, 16(6):1121–1140.
- Bozzano, F., Chiocci, F., Mazzanti, P., Bosman, A., Casalbore, D., Giuliani, R., Martino, S., Prestininzi, A., and Mugnozza, G. S. (2006). Subaerial and submarine characterization of the landslide responsible for the 1783 Scilla tsunami. In *Geophysical Research Abstracts*, volume 8.

- Bozzano, F., Lenti, L., Martino, S., Montagna, A., and Paciello, A. (2011). Earthquake triggering of landslides in highly jointed rock masses: reconstruction of the 1783 Scilla rock avalanche (Italy). *Geomorphology*, 129(3-4):294–308.
- Bui, H. H., Fukagawa, R., Sako, K., and Ohno, S. (2008). Lagrangian meshfree particles method (SPH) for large deformation and failure flows of geomaterial using elastic–plastic soil constitutive model. *International Journal for Numerical and Analytical Methods in Geomechanics*, 32(12):1537–1570.
- Caine, N. (1980). The rainfall intensity-duration control of shallow landslides and debris flows. *Geografiska Analer: Sries A, Physical Geography*, 62(1-2):23–27.
- Cascini, L., Cuomo, S., Pastor, M., and Sorbino, G. (2009). Modeling of rainfall-induced shallow landslides of the flow-type. *Journal of Geotechnical and Geoenvironmental Engineering*, 136(1):85–98.
- Castro-Orgaz, O., Hutter, K., Giraldez, J. V., and Hager, W. H. (2015). Nonhydrostatic granular flow over 3-D terrain: New Boussinesq-type gravity waves? *Journal of Geophysical Research: Earth Surface*, 120(1):1–28.
- Catalano, S., De Guidi, G., Monaco, C., Tortorici, G., and Tortorici, L. (2008). Active faulting and seismicity along the Siculo–Calabrian Rift Zone (southern Italy). *Tectonophysics*, 453(1-4):177–192.
- Chang, C. S. (1992). Discrete element method for slope stability analysis. *Journal of Geotechnical Engineering*, 118(12):1889–1905.
- Chen, C.-L. (1988). Generalized viscoplastic modeling of debris flow. *Journal of Hydraulic Engineering*, 114(3):237–258.
- Chen, W.-F. (2013). *Limit analysis and soil plasticity*. Elsevier.
- Cheng, Y., Lansivaara, T., and Wei, W. (2007). Two-dimensional slope stability analysis by limit equilibrium and strength reduction methods. *Computers and Geotechnics*, 34(3):137–150.
- Collins, B. D. and Znidarcic, D. (2004). Stability analyses of rainfall induced landslides. *Journal of Geotechnical and Geoenvironmental Engineering*, 130(4):362–372.
- Cremonesi, M., Frangi, A., and Perego, U. (2010). A Lagrangian finite element approach for the analysis of fluid–structure interaction problems. *International Journal for Numerical Methods in Engineering*, 84(5):610–630.
- Cremonesi, M., Frangi, A., and Perego, U. (2011). A Lagrangian finite element approach for the simulation of water-waves induced by landslides. *Computers & Structures*, 89(11-12):1086–1093.
- Cuomo, S., Prime, N., Iannone, A., Dufour, F., Cascini, L., and Darve, F. (2013). Large deformation FEMLIP drained analysis of a vertical cut. *Acta Geotechnica*, 8(2):125–136.
- Dávalos, C., Cante, J., Hernández, J., and Oliver, J. (2015). On the numerical modeling of granular material flows via the Particle Finite Element Method (PFEM). *International Journal of Solids and Structures*, 71:99–125.

- Dawson, E., Roth, W., and Drescher, A. (1999). Slope stability analysis by strength reduction. *Géotechnique*, 49(6):835–840.
- Del Gaudio, V. and Wasowski, J. (2007). Directivity of slope dynamic response to seismic shaking. *Geophysical Research Letters*, 34(12).
- Denlinger, R. P. and Iverson, R. M. (2004). Granular avalanches across irregular three-dimensional terrain: 1. Theory and computation. *Journal of Geophysical Research: Earth Surface*, 109(F1).
- Dey, R., Hawlader, B., Phillips, R., and Soga, K. (2015). Large deformation finite-element modeling of progressive failure leading to spread in sensitive clay slopes. *Géotechnique*, 65(8):657–668.
- Di, Y., Yang, J., and Sato, T. (2007). An operator-split ALE model for large deformation analysis of geomaterials. *International Journal for Numerical and Analytical Methods in Geomechanics*, 31(12):1375–1399.
- Dieterich, J. H. (1979). Modeling of rock friction: 1. Experimental results and constitutive equations. *Journal of Geophysical Research: Solid Earth*, 84(B5):2161–2168.
- Donea, J., Giuliani, S., and Halleux, J.-P. (1982). An arbitrary Lagrangian-Eulerian finite element method for transient dynamic fluid-structure interactions. *Computer Methods in Applied Mechanics and Engineering*, 33(1-3):689–723.
- Faccanoni, G. and Mangeney, A. (2013). Exact solution for granular flows. *International Journal for Numerical and Analytical Methods in Geomechanics*, 37(10):1408–1433.
- Fagherazzi, S., Rasetarinera, P., Hussaini, M. Y., and Furbish, D. J. (2004). Numerical solution of the dam-break problem with a discontinuous Galerkin method. *Journal of Hydraulic Engineering*, 130(6):532–539.
- Fan, X., Scaringi, G., Korup, O., West, A. J., van Westen, C. J., Tanyas, H., Hovius, N., Hales, T. C., Jibson, R. W., Allstadt, K. E., et al. (2019). Earthquake-Induced Chains of Geologic Hazards: Patterns, Mechanisms, and Impacts. *Reviews of Geophysics*, 57:421–503.
- Fennema, R. J. and Chaudhry, M. H. (1990). Explicit methods for 2-D transient free surface flows. *Journal of Hydraulic Engineering*, 116(8):1013–1034.
- Fernández-Nieto, E. D., Bouchut, F., Bresch, D., Diaz, M. C., and Mangeney, A. (2008). A new Savage–Hutter type model for submarine avalanches and generated tsunami. *Journal of Computational Physics*, 227(16):7720–7754.
- Fredlund, D. and Krahn, J. (1977). Comparison of slope stability methods of analysis. *Canadian Geotechnical Journal*, 14(3):429–439.
- Gingold, R. A. and Monaghan, J. J. (1977). Smoothed particle hydrodynamics: theory and application to non-spherical stars. *Monthly Notices of the Royal Astronomical Society*, 181(3):375–389.
- Goodman, P. and Seed, H. B. (1966). Earthquake-induced displacements in sand embankments. *Journal of Soil Mechanics & Foundations Division*, 92(ASCE Proceeding).

- Gray, J. and Thornton, A. (2005). A theory for particle size segregation in shallow granular free-surface flows. *Proceedings of the Royal Society A: Mathematical, Physical and Engineering Sciences*, 461(2057):1447–1473.
- Gray, J., Wieland, M., and Hutter, K. (1999). Gravity-driven free surface flow of granular avalanches over complex basal topography. 455(1985):1841–1874.
- Graziani, L., Maramai, A., and Tinti, S. (2006). A revision of the 1783–1784 Calabrian (southern Italy) tsunamis. *Natural Hazards and Earth System Sciences*, 6(6):1053–1060.
- Griffiths, D. and Lane, P. (1999). Slope stability analysis by finite elements. *Géotechnique*, 49(3):387–403.
- Griffiths, D. and Marquez, R. (2007). Three-dimensional slope stability analysis by elastoplastic finite elements. *Géotechnique*, 57(6):537–546.
- Hu, X., Huang, R.-Q., Shi, Y.-B., Lv, X.-P., Zhu, H.-Y., and Wang, X.-R. (2009). Analysis of Blocking River Mechanism of Tangjiashan Landslide and Dam-Breaking Mode. *Chinese Journal of Rock Mechanics and Engineering*, 28(1):181–189 (in Chinese).
- Hu, Y. and Randolph, M. (1998). A practical numerical approach for large deformation problems in soil. *International Journal for Numerical and Analytical Methods in Geomechanics*, 22(5):327–350.
- Huang, Y., Zhang, W., Xu, Q., Xie, P., and Hao, L. (2012). Run-out analysis of flow-like landslides triggered by the Ms 8.0 2008 Wenchuan earthquake using smoothed particle hydrodynamics. *Landslides*, 9(2):275–283.
- Hungr, O. (1995). A model for the runout analysis of rapid flow slides, debris flows, and avalanches. *Canadian Geotechnical Journal*, 32(4):610–623.
- Hungr, O., Leroueil, S., and Picarelli, L. (2014). The Varnes classification of landslide types, an update. *Landslides*, 11(2):167–194.
- Hungr, O. and McDougall, S. (2009). Two numerical models for landslide dynamic analysis. *Computers & Geosciences*, 35(5):978–992.
- Idelsohn, S. R., Onate, E., Calvo, N., and Del Pin, F. (2003). The meshless finite element method. *International Journal for Numerical Methods in Engineering*, 58(6):893–912.
- Idelsohn, S. R., Oñate, E., and Pin, F. D. (2004). The particle finite element method: a powerful tool to solve incompressible flows with free-surfaces and breaking waves. *International Journal for Numerical Methods in Engineering*, 61(7):964–989.
- Idriss, I. M. and Seed, H. B. (1967). Response of earth banks during earthquakes. *Journal of Soil Mechanics & Foundations Division*, 93(3):61–82.
- Islam, N., Hawlader, B., Wang, C., and Soga, K. (2018). Large-deformation finite-element modelling of earthquake-induced landslides considering strain-softening behaviour of sensitive clay. *Canadian Geotechnical Journal*, (999):1–16.
- Iverson, R. M. (1997). The physics of debris flows. *Reviews of Geophysics*, 35(3):245–296.

- Iverson, R. M. (2005). Regulation of landslide motion by dilatancy and pore pressure feedback. *Journal of Geophysical Research: Earth Surface*, 110(F2).
- Iverson, R. M. and Denlinger, R. P. (2001). Flow of variably fluidized granular masses across three-dimensional terrain: 1. Coulomb mixture theory. *Journal of Geophysical Research: Solid Earth*, 106(B1):537–552.
- Jiang, G.-S. and Tadmor, E. (1998). Nonoscillatory central schemes for multidimensional hyperbolic conservation laws. *SIAM Journal on Scientific Computing*, 19(6):1892–1917.
- Jibson, R. W. (2011). Methods for assessing the stability of slopes during earthquakes—a retrospective. *Engineering Geology*, 122(1-2):43–50.
- Jop, P., Forterre, Y., and Pouliquen, O. (2006). A constitutive law for dense granular flows. *Nature*, 441(7094):727.
- Keefer, D. K. and Larsen, M. C. (2007). Assessing landslide hazards. *Science*, 316(5828):1136–1138.
- Krabbenhoft, K., Karim, M., Lyamin, A., and Sloan, S. (2012a). Associated computational plasticity schemes for nonassociated frictional materials. *International Journal for Numerical Methods in Engineering*, 90(9):1089–1117.
- Krabbenhoft, K., Lyamin, A., Huang, J., and da Silva, M. V. (2012b). Granular contact dynamics using mathematical programming methods. *Computers and Geotechnics*, 43:165–176.
- Krabbenhoft, K., Lyamin, A., Sloan, S., and Wriggers, P. (2007). An interior-point algorithm for elastoplasticity. *International Journal for Numerical Methods in Engineering*, 69(3):592–626.
- Kurganov, A. and Tadmor, E. (2000). New high-resolution central schemes for nonlinear conservation laws and convection–diffusion equations. *Journal of Computational Physics*, 160(1):241–282.
- La Rocca, M., Montessori, A., Prestininzi, P., and Succi, S. (2015). A multispeed discrete Boltzmann model for transcritical 2D shallow water flows. *Journal of Computational Physics*, 284:117–132.
- Lax, P. D. (1954). Weak solutions of nonlinear hyperbolic equations and their numerical computation. *Communications on pure and applied mathematics*, 7(1):159–193.
- Lian, Y., Zhang, X., and Liu, Y. (2012). An adaptive finite element material point method and its application in extreme deformation problems. *Computer Methods in Applied Mechanics and Engineering*, 241:275–285.
- Lin, M.-L. and Wang, K.-L. (2006). Seismic slope behavior in a large-scale shaking table model test. *Engineering Geology*, 86(2-3):118–133.
- Ling, H. I., Leshchinsky, D., and Mohri, Y. (1997). Soil slopes under combined horizontal and vertical seismic accelerations. *Earthquake Engineering & Structural Dynamics*, 26(12):1231–1241.

- Louaked, M. and Hanich, L. (1998). TVD scheme for the shallow water equations. *Journal of Hydraulic Research*, 36(3):363–378.
- Lucas, A., Mangeney, A., and Ampuero, J. P. (2014). Frictional velocity-weakening in landslides on Earth and on other planetary bodies. *Nature communications*, 5:3417.
- Lucy, L. B. (1977). A numerical approach to the testing of the fission hypothesis. *The Astronomical Journal*, 82:1013–1024.
- Luo, G., Hu, X., Gu, C., and Wang, Y. (2012). Numerical simulations of kinetic formation mechanism of tangjiashan landslide. *Journal of Rock Mechanics and Geotechnical Engineering*, 4(2):149–159.
- Mangeney, A., Bouchut, F., Vilotte, J., Lajeunesse, E., Aubertin, A., and Pirulli, M. (2005). On the use of Saint Venant equations to simulate the spreading of a granular mass. *Journal of Geophysical Research: Solid Earth*, 110(B9).
- Mazzanti, P. and Bozzano, F. (2011). Revisiting the February 6th 1783 Scilla (Calabria, Italy) landslide and tsunami by numerical simulation. *Marine Geophysical Research*, 32(1-2):273–286.
- Meng, X. and Wang, Y. (2016). Modelling and numerical simulation of two-phase debris flows. *Acta Geotechnica*, 11(5):1027–1045.
- Mergili, M., Jan-Thomas, F., Krenn, J., and Pudasaini, S. P. (2017). r. avaflow v1, an advanced open-source computational framework for the propagation and interaction of two-phase mass flows. *Geoscientific Model Development*, 10(2):553.
- Mesri, G. and Shahien, M. (2003). Residual shear strength mobilized in first-time slope failures. *Journal of Geotechnical and Geoenvironmental Engineering*, 129(1):12–31.
- Minasi, G. (1785). Continuazione ed appendice sopra i tremuoti descritti nella relazione colla data di Scilla de 30 settembre 1783, con altro che accadde in progresso. *Messina*, (in Italian).
- MOSEK, A. (2019). The MOSEK optimization toolbox for MATLAB manual Release 9.0.97(2019). URL <https://docs.mosek.com/9.0/toolbox.pdf>.
- Nessyahu, H. and Tadmor, E. (1990). Non-oscillatory central differencing for hyperbolic conservation laws. *Journal of Computational Physics*, 87(2):408–463.
- Newmark, N. M. (1965). Effects of earthquakes on dams and embankments. *Géotechnique*, 15(2):139–160.
- Oñate, E., Idelsohn, S. R., Celigueta, M. A., Rossi, R., Marti, J., Carbonell, J., Ryzhakov, P., and Suárez, B. (2011). Advances in the particle finite element method (PFEM) for solving coupled problems in engineering. In *Particle-Based Methods*, pages 1–49. Springer.
- Oñate, E., Idelsohn, S. R., Del Pin, F., and Aubry, R. (2004). The particle finite element method—an overview. *International Journal of Computational Methods*, 1(02):267–307.

- Ouyang, C., He, S., Xu, Q., Luo, Y., and Zhang, W. (2013). A MacCormack-TVD finite difference method to simulate the mass flow in mountainous terrain with variable computational domain. *Computers & geosciences*, 52:1–10.
- Peng, C., Guo, X., Wu, W., and Wang, Y. (2016). Unified modelling of granular media with smoothed particle hydrodynamics. *Acta Geotechnica*, 11(6):1231–1247.
- Peng, C., Wu, W., Yu, H.-s., and Wang, C. (2015). A SPH approach for large deformation analysis with hypoplastic constitutive model. *Acta Geotechnica*, 10(6):703–717.
- Peng, M. and Zhang, L. (2012). Analysis of human risks due to dam break floods—part 2: application to Tangjiashan landslide dam failure. *Natural hazards*, 64(2):1899–1923.
- Persson, P.-O. and Strang, G. (2004). A simple mesh generator in MATLAB. *SIAM Review*, 46(2):329–345.
- Pitman, E. B. and Le, L. (2005). A two-fluid model for avalanche and debris flows. *Philosophical Transactions of the Royal Society A: Mathematical, Physical and Engineering Sciences*, 363(1832):1573–1601.
- Porfido, S., Esposito, E., Violante, C., Molisso, F., Sacchi, M., and Spiga, E. (2011). Earthquakes-induced environmental effects in coastal area: some example in Calabria and Sicily (Southern Italy). *Marine Research at CNR Dta*.
- Potts, D., Dounias, G., and Vaughan, P. (1990). Finite element analysis of progressive failure of Carsington embankment. *Géotechnique*, 40(1):79–101.
- Pudasaini, S. P. (2012). A general two-phase debris flow model. *Journal of Geophysical Research: Earth Surface*, 117(F3).
- Reissner, E. (1950). On a variational theorem in elasticity. *Journal of Mathematics and Physics*, 29(1-4):90–95.
- Ronchetti, F., Borgatti, L., Cervi, F., Gorgoni, C., Piccinini, L., Vincenzi, V., and Corsini, A. (2009). Groundwater processes in a complex landslide, northern Apennines, Italy. *Natural Hazards and Earth System Sciences*, 9(3):895–904.
- Rovida, A., Camassi, R., Gasperini, P., and Stucchi, M. (2011). The 2011 version of the Parametric Catalogue of Italian Earthquakes. Milano, Bologna.
- Savage, S. B. and Hutter, K. (1989). The motion of a finite mass of granular material down a rough incline. *Journal of Fluid Mechanics*, 199:177–215.
- Shewchuk, J. R. (1996). Triangle: Engineering a 2D quality mesh generator and Delaunay triangulator. In *Workshop on Applied Computational Geometry*, pages 203–222. Springer.
- Simo, J., Kennedy, J., and Taylor, R. (1989). Complementary mixed finite element formulations for elastoplasticity. *Computer Methods in Applied Mechanics and Engineering*, 74(2):177–206.
- Simo, J. C. and Taylor, R. L. (1985). Consistent tangent operators for rate-independent elastoplasticity. *Computer Methods in Applied Mechanics and Engineering*, 48(1):101–118.

- Soga, K., Alonso, E., Yerro, A., Kumar, K., and Bandara, S. (2015). Trends in large-deformation analysis of landslide mass movements with particular emphasis on the material point method. *Géotechnique*, 66(3):248–273.
- Staron, L. (2008). Mobility of long-runout rock flows: a discrete numerical investigation. *Geophysical Journal International*, 172(1):455–463.
- Tai, Y.-C., Noelle, S., Gray, J., and Hutter, K. (2002). Shock-capturing and front-tracking methods for granular avalanches. *Journal of Computational Physics*, 175(1):269–301.
- Tang, C.-L., Hu, J.-C., Lin, M.-L., Angelier, J., Lu, C.-Y., Chan, Y.-C., and Chu, H.-T. (2009). The Tsaoling landslide triggered by the Chi-Chi earthquake, Taiwan: insights from a discrete element simulation. *Engineering Geology*, 106(1-2):1–19.
- Terzaghi, K. (1950). Mechanism of landslides. *Geological Society of America*, S:83–123.
- Tian, Y., Cassidy, M. J., Randolph, M. F., Wang, D., and Gaudin, C. (2014). A simple implementation of RITSS and its application in large deformation analysis. *Computers and Geotechnics*, 56:160–167.
- Tinti, S., Bortolucci, E., and Vannini, C. (1997). A block-based theoretical model suited to gravitational sliding. *Natural Hazards*, 16(1):1–28.
- Tits, A. L., Wächter, A., Bakhtiari, S., Urban, T. J., and Lawrence, C. T. (2003). A primal-dual interior-point method for nonlinear programming with strong global and local convergence properties. *SIAM Journal on Optimization*, 14(1):173–199.
- Trifunac, M. (1972). Scattering of plane SH waves by a semi-cylindrical canyon. *Earthquake Engineering & Structural Dynamics*, 1(3):267–281.
- Troncone, A. (2005). Numerical analysis of a landslide in soils with strain-softening behaviour. *Géotechnique*, 55(8):585–596.
- Van Asch, T. W., Malet, J.-P., van Beek, L. P., and Amitrano, D. (2007). Techniques, issues and advances in numerical modelling of landslide hazard. *Bulletin de la Société Géologique de France*, 178(2):65–88.
- Varnes, D. J. (1978). Slope movement types and processes. *Special report*, 176:11–33.
- Violeau, D. and Rogers, B. D. (2016). Smoothed particle hydrodynamics (SPH) for free-surface flows: past, present and future. *Journal of Hydraulic Research*, 54(1):1–26.
- Wang, B., Vardon, P. J., Hicks, M. A., and Chen, Z. (2016). Development of an implicit material point method for geotechnical applications. *Computers and Geotechnics*, 71:159–167.
- Wang, D., Chen, X., Yu, Y., Jie, Y., and Lyu, Y. (2018). Stability and deformation analysis for geotechnical problems with nonassociated plasticity based on second-order cone programming. *International Journal of Geomechanics*, 19(2):04018190.
- Wang, L., Zaniboni, F., Tinti, S., and Zhang, X. (2019a). Reconstruction of the 1783 Scilla landslide, Italy: numerical investigations on the flow-like behaviour of landslides. *Landslides*, 16(6):1065–1076.

- Wang, L., Zhang, X., Zaniboni, F., Oñate, E., and Tinti, S. (2019b). Mathematical optimization problems for particle finite element analysis applied to 2D landslide modeling. *Mathematical Geosciences*, pages 1–23.
- Wartman, J., Seed, R. B., and Bray, J. D. (2005). Shaking table modeling of seismically induced deformations in slopes. *Journal of Geotechnical and Geoenvironmental Engineering*, 131(5):610–622.
- Wiegel, R. L. (1970). Earthquake engineering. In *Earthquake engineering*. Prentice-Hall.
- Wilson, R. C. and Keefer, D. K. (1983). Dynamic analysis of a slope failure from the 6 August 1979 Coyote Lake, California, earthquake. *Bulletin of the Seismological Society of America*, 73(3):863–877.
- Wong, H. (1982). Effect of surface topography on the diffraction of P, SV, and Rayleigh waves. *Bulletin of the Seismological Society of America*, 72(4):1167–1183.
- Xia, X. and Liang, Q. (2018). A new depth-averaged model for flow-like landslides over complex terrains with curvatures and steep slopes. *Engineering Geology*, 234:174–191.
- Xu, Q., Fan, X.-M., Huang, R.-Q., and Van Westen, C. (2009). Landslide dams triggered by the Wenchuan Earthquake, Sichuan Province, south west China. *Bulletin of engineering geology and the environment*, 68(3):373–386.
- Yerro, A., Alonso, E., and Pinyol, N. (2016). Run-out of landslides in brittle soils. *Computers and Geotechnics*, 80:427–439.
- Zaniboni, F., Armigliato, A., and Tinti, S. (2016). A numerical investigation of the 1783 landslide-induced catastrophic tsunami in Scilla, Italy. *Natural Hazards*, 84(2):455–470.
- Zaniboni, F., Pagnoni, G., Gallotti, G., Paparo, M. A., Armigliato, A., and Tinti, S. (2019). Assessment of the 1783 Scilla landslide–tsunami’s effects on the Calabrian and Sicilian coasts through numerical modeling. *Natural Hazards and Earth System Sciences*, 19(8):1585–1600.
- Zaniboni, F. and Tinti, S. (2014). Numerical simulations of the 1963 Vajont landslide, Italy: application of 1D Lagrangian modelling. *Natural hazards*, 70(1):567–592.
- Zhang, X., Krabbenhoft, K., Pedroso, D., Lyamin, A., Sheng, D., Da Silva, M. V., and Wang, D. (2013). Particle finite element analysis of large deformation and granular flow problems. *Computers and Geotechnics*, 54:133–142.
- Zhang, X., Krabbenhoft, K., Sheng, D., and Li, W. (2015). Numerical simulation of a flow-like landslide using the particle finite element method. *Computational Mechanics*, 55(1):167–177.
- Zhang, X., Oñate, E., Torres, S. A. G., Bleyer, J., and Krabbenhoft, K. (2019). A unified lagrangian formulation for solid and fluid dynamics and its possibility for modelling submarine landslides and their consequences. *Computer Methods in Applied Mechanics and Engineering*, 343:314–338.
- Zhang, X., Sheng, D., Sloan, S. W., and Bleyer, J. (2017). Lagrangian modelling of large deformation induced by progressive failure of sensitive clays with elastoviscoplasticity. *International Journal for Numerical Methods in Engineering*, 112(8):963–989.

